Probing the Universe with Multimessenger Astronomy

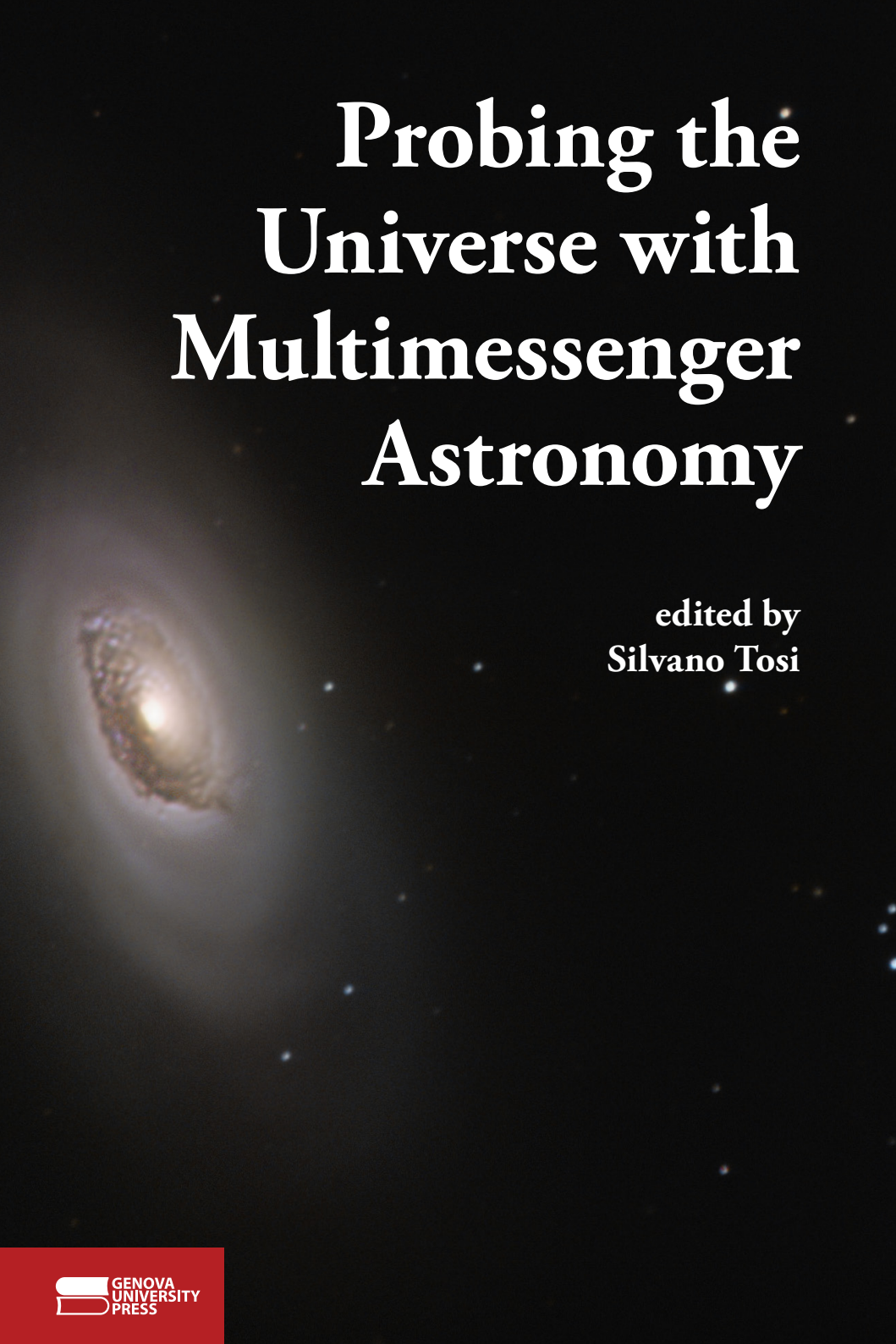

edited by
Silvano Tosi

GENOVA UNIVERSITY PRESS

Scienze Fisiche

1

Probing the Universe with Multimessenger Astronomy

edited by
Silvano Tosi

GENOVA UNIVERSITY PRESS

GENOVA UNIVERSITY PRESS
è il marchio editoriale dell'Università di Genova

Università di Genova

This volume is a collection of original contributions of the invited speakers to the Probing the universe with multi-messenger astrophysics, held in Sestri Levante on September 26-30, 2022.

Organizing Committee: Marialuisa Aliotta (Edinburgh University - UK), Laura Cadonati (Georgia Institute of Technology - USA), Paschal Coyle (CPPM Marseille - France), Luigi Guzzo (University of Milan - Italy), Giovanni Losurdo (INFN-Pisa - Italy), Maria Lugaro (Konkoly Observatory, Budapest - Hungary), Aldo Serenelli (Institute of Space Sciences, Barcelona - Spain), Filippo Maria Zerbi (INAF-Osservatorio di Brera - Italy), Silvano Tosi (University of Genoa and INFN-Genoa - Italy).

UPI UNIVERSITY PRESS ITALIANE
Il presente volume è stato sottoposto a double blind peer-review secondo i criteri stabiliti dal protocollo UPI

ISBN: 978-88-3618-218-3 (versione PDF)

Pubblicato a maggio 2023

Realizzazione Editoriale
GENOVA UNIVERSITY PRESS
Via Balbi, 6 – 16126 Genova
Tel. 010 20951558 – Fax 010 20951552
e-mail: gup@unige.it
https://gup.unige.it

TABLE OF CONTENTS

The Moon: a frontier for gravitational waves astrophysics with LGWA

Francesca Badaracco[1] on behalf of the LGWA collaboration

Abstract

The Lunar Gravitational-Wave Antenna (LGWA) is a proposed detector concept that aims at measuring the lunar vibrations induced by gravitational waves using an array of seismic sensors as Moon-read-out. The concept is the same as that used for the gravitational waves bar detectors. LGWA will be sensitive to the deci-Hz frequency band, thus bridging the gap between current (and future) terrestrial gravitational wave detectors and space-based ones. This contribution will discuss the LGWA project, the scientific results it can deliver and the technologies needed for such an enterprise.

Key Words

Gravitational-wave detectors, Moon, seismic sensor.

Introduction

Gravitational Wave (GW) emission can happen in a broad range of wavelengths, depending on the phenomena involved. Therefore, different types of detectors need to be designed to cover as much GW spectrum as possible. Starting from very low frequencies (10-16 Hz)

[1] INFN Sez. Genova, Via Dodecaneso 33, 16146, Genova, Italia
Correspondence: francesca.badaracco92@gmail.com

there are GWs of primordial origin which can be detected only with inflation probes (Ade, 2014). At 10-9 Hz GWs are produced by supermassive binary black holes (BH), detectable with Pulsar Timing Arrays (Hobbs, 2010), while the 1 mHz-1 Hz band can be covered by space detectors (like LISA), which are designed to search for ultra-compact binaries, supermassive BH mergers, extreme mass ratio inspirals, and other exotic possibilities (Baker, 2019; Shuichi, 2009; Luo, 2016). From a few Hz to a few kHz, Earth-bound GW detectors, such as Virgo, LIGO, KAGRA and the next generation interferometric detectors like the Einstein Telescope (ET) and Cosmic Explorer (CE) can detect BH or neutron star (NS) mergers and other possible sources (Maggiore, 2020; Reitze, 2019; The LIGO Scientific Collaboration, 2015; KAGRA collaboration, 2019; Acernese, 2015). It is noteworthy that the Lunar Gravitational-Wave Antenna (LGWA) can bridge the sensitivity gap between LISA and ET (see Fig. 1), pushing it down in the 0.1-1 Hz band (Harms, 2021). In this band there are many interesting sources that are worth studying in more detail: LGWA concept and its science goals will be described in the following.

Detector concept and working principle

The Moon is the closest object to Earth, it is large and it has a lower seismic activity. The low seismicity is principally due to the absence of an atmosphere and oceans. It is known, in fact, that their presence generates most of the seismic ambient noise on Earth (Bonnefoy-Claudet, 2006). Seismic levels on the Moon are not yet well defined: the scientific community disposes of measurements coming from Apollo missions which measured many moonquakes over the past years. However, the continuous seismic background was too faint to be measured and, therefore, only the upper limit coinciding with the self-noise of the deployed seismic sensors is available (Coughlin & Harms, 2014).

Given these premises, the Moon can be thought as a giant GW resonant detector: since the driving forces in a GW have a quadrupolar

spatial distributions (Thorne, 2000), a GW sweeping over the Moon will excite its quadrupole modes of vibration. It is therefore possible to use a simple array of seismic sensors deployed on the Moon to search for GWs. This approach was in the beginning proposed for the Earth (Weber, 1967) which, however, has an inadequate seismic noise level and do not allow to detect any GW signal (Dyson, 1968).

Fig. 1 shows a possible sensitivity for LGWA which eventually will depend on the not yet well understood Lunar geology details. The peaks and dips in the curve depend on the quadrupolar modes of the Moon.

Historically, there has already been an attempt to use the Moon as a GW resonant detector with the mission Apollo 17 (in 1972). Unfortunately, the Lunar Surface Gravimeter, meant to record the Lunar seismic background, did not work as expected because of an arithmetic error in its design (Giganti et al., 1977). Later, three works were performed by Coughlin & Harms to constrain the GW energy density using Earth's and Moon's (Apollo missions) seismic data (Coughlin & Harms 2014a, 2014b, 2014c).

LGWA is not the only existing lunar GW detector concept: other two have been independently conceived. One is the Lunar Seismic and Gravitational Antenna (LSGA) (Katsanevas et al., 2020) and the other is the Gravitational-Wave Lunar Observatory for Cosmology (GLOC) (Jani & Loeb, 2021). While LGWA takes a differential measurement between the seismic sensor and the Moon, LSGA measures the strain induced by the GW on the Moon. Finally, GLOC is designed to be an interferometric detector like Virgo/LIGO/KAGRA, and therefore it will measure the strain between two free falling test masses taking advantage of the low seismic noise of the Moon.

Environmental Challenges

The lunar environment is extremely quiet from the seismic point of view: this makes it the perfect place for GW experiments. However, it is also a source of other technological challenges. For example, the lu-

nar dust (Grün, 2011) and the cosmic radiation can damage the equipment. In particular, cosmic radiation will lead to a continuous charging of the lunar regolith (Jordan, 2014), which can consequently develop strong electric fields.

Temperatures can drastically change between lunar days and nights, passing from 400 K to 100 K (Williams, 2017): it will be therefore necessary to deploy the sensor array in a permanently shadowed region (i.e. inside lunar craters). These regions can provide a stable thermal environment and behave as a natural cryostat, which will be needed to keep the sensors' thermal noise at an acceptable level. However, this comes at the price of finding an efficient way to power the sensors and the necessary equipment. There are various possibilities to power LGWA: a radioisotope thermoelectric generator (RTG) (Blanke, 1960), which however might be problematic from the material provision point of view; a conjunction of solar panels placed on the crater ridge and power-beaming technologies (Rodenbeck, 2021) or other ways to transport the power from the solar panel to the sensors (e.g. cables or a telescopic mechanism to directly reach the sunlight in the vertical direction).

LGWA Science

The deci-Hz band can open many interesting opportunities for GW physics and for cosmology, it is therefore important to have a detector which is sensitive in this frequency band. Moreover, such a detector would allow for multi-band observations with other existing GW detectors: this could further enrich the information collected from GWs.

Possible observations will account for massive binary BHs (10^5 to 10^{10} solar masses) which are otherwise hard to be observed. LGWA could also localise these events, thus providing the possibility of finding potential electromagnetic counterparts. Another possible source for LGWA are mergers of binary white dwarfs, which are suspected to be the progenitors of supernovae Ia (Iben, 1984). Therefore, an observation of a binary white dwarf merger in conjunction (and at the same

location) with an optical or high-energy signal from a supernova Ia would be an epochal discovery.

Tests of general relativity and studies on possible modifications of the theory will also be possible. Given that LGWA will be able to detect compact binaries signals even years before ET, multi-band observations will also be possible. However, LGWA will not only be a GW detector but it will also constitute an observatory for studying lunar geology (that we might rename selenology), leading to a leap in the knowledge of our satellite. Indeed, even if the Apollo missions have been able to study in detail the Moon, much remains to be explored and discovered about its origin and internal structure. For more insights on the LGWA science, the Reader is referred to Ref. (Harms, 2020).

Conclusions

LGWA will bridge the gap between LISA and ET sensitivities, providing the possibility of studying sources in more detail (for example, with multiband observations). LGWA aims to exploit technologies already under development; indeed, seismic sensors with the necessary sensitivity are already being developed for ET. Tests on the sensors will need to be done in an ultra-quiet seismic environment which can be reproduced in an underground laboratory with the aid of actively suppressed seismic motion platforms (also under development for ET). Finally, a system to cancel the seismic noise produced by meteoric impacts will be tested and developed on Mount Etna. Therefore, LGWA is designed to be a future GW detector that is simple to deploy and operate and that will use existing technology.

Acknowledgements

F.B. would like to dedicate this contribution to Stavros Katsanevas who passed away in November 2022 and who has been a pioneer in Lunar GW detector concepts and the proponent of LSGA.

F.B. would also like to thank Jan Harms for his useful comments

and discussions.

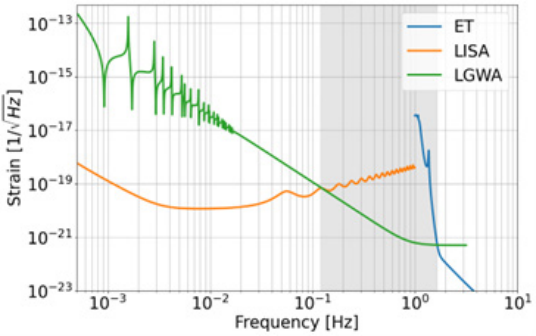

Figure 1: Comparison of the sensitivities of ET, LISA and LGWA relative to GW strain. The gray zone represents the area where LGWA performs better than ET and LISA therefore bridging the sensitivity gap between the two detectors.

References

Acernese, F., et al., 2015. Advanced Virgo: a second-generation interferometric gravitational wave detector. Class. Quantum Grav. 32 024001.

Ade, P.A.R., et al., 2014. Detection of B-Mode Polarization at Degree Angular Scales by BICEP2. Phys. Rev. Lett. 112, 241101.

Baker, J., et al., 2019. The Laser Interferometer Space Antenna: Unveiling the Millihertz Gravitational Wave Sky. arXiv preprint arXiv:1907.06482.

Blanke, B.C., et al., 1960. Nuclear battery-thermocouple type summary report (No. MLM-1127). Mound Lab., Miamisburg, Ohio.

Bonnefoy-Claudet, S., Cotton, F. and Bard, P.Y., 2006. The nature of noise wavefield and its applications for site effects studies: A literature review. Earth-Science Reviews, 79(3-4), pp. 205-227.

Coughlin, M. and Harms, J., 2014a. Constraining the gravitational-wave energy density of the Universe in the range 0.1Hz to 1Hz using the Apollo Seismic Array. Phys. Rev. D 90, 102001.

Coughlin, M. and Harms, J., 2014b. Upper Limit on a Stochastic Background of Gravitational Waves from Seismic Measurements in the Range 0.05–1Hz. PhRvD, 90, 102001.

Coughlin, M. and Harms, J., 2014c. Constraining the gravitational wave energy density of the Universe using Earth's ring. Phys. Rev. D 90, 042005.

Dyson, F.J., 1968. Seismic response of the Earth to a gravitational wave in the 1-Hz band. The Astrophysical Journal, Vol. 156, May 1969.

Giganti, J., et al., 1977, Lunar Surface Gravimeter Experiment. Final Report, Tech. Rep., University of Maryland Department of Physics and Astronomy.

Grün, E., et al., 2011. The lunar dust environment. Planetary and Space Science, 59(14), pp. 1672-1680.

Harms, J., et al., 2021. Lunar Gravitational-wave Antenna. ApJ 910 1.

Hobbs, G., et al., 2010, The International Pulsar Timing Array project: using pulsars as a gravitational wave detector. Class. Quantum Grav. 27 084013.

Iben Jr, I. and Tutukov, A.V., 1984, Supernovae of type I as end products of the evolution of binaries with components of moderate initial mass (M not greater than about 9 solar masses). The Astrophysical Journal Supplement Series, 54, pp. 335-372.

Jani, K. and Loeb, A., 2021. Gravitational-wave Lunar Observatory for Cosmology. JCAP06(2021)044.

Jordan, A.P. et al., 2014. Deep dielectric charging of regolith within the Moon's permanently shadowed regions. Journal of Geophysical Research: Planets, 119(8), pp. 1806-1821.

KAGRA collaboration. KAGRA: 2.5 generation interferometric gravitational wave detector. Nat Astron 3, 35-40.

Katsanevas, S., et al., 2020. In Ideas for exploring the Moon with a large European lander (ESA, 2020), p. 1, URL https://ideas.esa.int/servlet/hype/IMT?documentTableId=45087607031744010&userAction=Browse&templateName=&documentId=a315450fae481074411ef65e4c5b7746.

Luo, J., et al., 2016. TianQin: a space-borne gravitational wave detector. Class. Quantum Grav. 33 035010.

Maggiore, M., et al., 2020. Science case for the Einstein telescope. Journal of Cosmology and Astroparticle Physics, 2020(03), p. 050.

Reitze, D., et al., 2019. Cosmic explorer: the US contribution to gravitational-wave astronomy beyond LIGO. arXiv preprint arXiv:1907.04833.

Rodenbeck, C.T., et al., 2021. Microwave and millimeter wave power beaming. IEEE Journal of Microwaves, 1(1), pp. 229-259.

Shuichi, S., 2019. DECIGO: The Japanese space gravitational wave antenna. J. Phys.: Conf. Ser. 154 012040.

The LIGO Scientific Collaboration et al., 2015. Advanced LIGO. Class. Quantum Grav. 32 074001.

Thorne, K.S., Charles, W.M. and John, A.W. 2000. Gravitation. San Francisco, CA: Freeman.

Weber, J., 1967. Gravitational Radiation. Phys. Rev. Lett. 18, 498.

Williams, J.P., et al., 2017. The global surface temperatures of the Moon as measured by the Diviner Lunar Radiometer Experiment. Icarus, 283, pp. 300-325.

Looking for orphan gamma-ray burst in the Rubin LSST data with the Fink Albert Broker

Johan Bregeon[1], *Marina Masson*[1]

Abstract

Gamma-ray bursts are highly energetic cosmological objects that provide us with different paths towards a better understanding of fundamental physics and the evolution of the universe. One idea consists in estimating the Hubble cosmological constant from gravitational wave events for which the distance can be estimated through electromagnetic observations. The perfect case was the one of GW 170817 / GRB 170817A, and indeed several initiatives are underway to optimize the matching of on-axis GRB signal (prompt, afterglow, kilonova) with sub-threshold gravitational waves. What we propose here is to provide new electromagnetic candidates for this matching by trying to identify off-axis GRBs in the Rubin LSST data through their so-called orphan optical afterglow emission. We will present our early work on this topic, starting with simulations with the afterglowpy package of off-axis GRB afterglow light curves on a large part of the phase space of the parameters: energy, distance, jet nature and geometry, burst environment. This set of simulation helped us to understand that indeed some orphan af-

[1] Univ. Grenoble Alpes, CNRS, Grenoble INP (Institute of Engineering Univ. Grenoble Alpes), LPSC-IN2P3, 38000 Grenoble, France
Correspondence: bregeon@in2p3.fr

terglows should appear in Rubin LSST data as faint and slow transients that could be observable from several days to several months. We then produced a population of short GRBs off-axis afterglows for which we ran pseudo-observations using the *rubin_sim* package that offers a realistic schedule of the 10 years long observations of the LSST. With that setup we are ready to dive into the characterization and identification of orphan afterglow light curves.

Key Words

Gamma-ray Burst, Cosmology, Astrophysics, Hubble constant, Multimessenger astronomy, Optical afterglow, Rubin Observatory, Gravitational Wave.

Introduction

In 2017, the first joint detection of the neutron star merger GW170817 by gravitational waves detectors and its gamma-ray burst counterpart by multiple instruments at different electromagnetic wavelengths, made possible a new type of measurement of the Hubble constant H_0 (Abbott et al., 2017). This new method, named the *standard siren* measurement, derives H_0 through the comparison of the luminosity distance d_L estimated from the gravitational wave waveform, and the redshift z measured via the spectroscopy of the host galaxy. With just one of these *sirens* observed so far, the probability density function remains quite large however, but a few tens should be sufficient to estimate H_0 with a statistical uncertainty similar to other existing measurements from the Cosmic Microwave Background (Planck, 2018) or the Supernovae (Riess, 2022). We therefore aim at increasing the number of standard sirens by looking for gravitational wave signals associated with orphan gamma-ray burst optical afterglows (OA) that we hope to find in the Rubin Legacy Survey of Space and Time data (Rubin LSST).

We will explain the basics of OA physics as implemented in the afterglow model that we have used to produce our simulations to first explore the parameters phase space. Then, we will describe the simula-

tion of a population of short gamma-ray bursts for which we produced light curves and spectra in order to produce pseudo-observations in the context of Rubin LSST. We will conclude with a path forward to develop an identification skim from light curves in the framework of the FINK alert broker (Möller, 2021).

Oophan gamma-ray burst afterglow

Gamma-ray bursts (GRBs) are among the most violent phenomena in the universe, releasing equivalent isotropic energies as large as 10^{54} ergs within the time frame of seconds to minutes. Initially detected in gamma rays at the end of the sixties, simply defined as bright bursts of high energy photons, GRBs were eventually also shown to have a so-called afterglow emission that could last from hours to days and cover the full electromagnetic spectrum from radio to very-high energy gamma rays (Mészáros, 2019).

The consensus reached on emission models is that GRB emission has to come from a relativistic jet, what implies that the viewing angle has a strong impact on observations. When the observer is far off the jet axis, gamma rays from the prompt phase become challenging to reveal while the afterglow emission, that comes from a larger region, still has good possibilities to be detected at optical and radio wave lengths. Orphan gamma-ray bursts are hence defined as GRB afterglows for which no emission is observed in gamma rays.

We focused our work specifically on the afterglow emission, using the afterglowpy python package (Ryan et al., 2020) that implements a standard synchrotron emission from the forward shock model. Afterglowpy solves the fully trans-relativistic shock evolution through a constant density medium and includes a number of important features for our use case, in particular an approximate prescription for jet spreading, an angularly structured jet and arbitrary viewing angles.

The python package is fully open source, very user friendly and easy to use: the user can simulate afterglow light curves and spectral energy

densities at any time on the full electromagnetic spectrum from any arbitrary observer angle. Bursts parameters include first the usual set of the burst characteristics like the isotropic equivalent energy, the redshift, the circumburst density, the electron energy distribution index and the microphysics parameters (ε_e and ε_B). Then the model also implements three different jet structures: standard top-hat for which the energy is uniform across the jet section and, Gaussian and power-law angular distributions. Three geometrical angles are hence defined: the core angle θ_c within which the largest part of the energy is contained (all of it for a top-hat jet), the angle θ_w (w for 'wing') above which the jet energy distribution is truncated, and θ_{obs} that is the observer angle with respect to the jet axis.

Afterglow light curve shape and observability

We first explore the burst parameters phase space by studying the impact of the jet structure on the light curve shape, and observe that structured jets (Gaussian or power-law energy distributions) light curves tend to rise and peak much earlier than the top-hat jets. This is understood as the energy distributed in the jet wings being more accessible by the observer for structured jets. Gaussian and power-law jets behave in a similar way unless the condition $\theta_w >> \theta_c$ is met, in which case, the Gaussian jet flux rises very slowly and eventually remains dimmer than the power-law jet.

Another interesting study was to check the dependence of the afterglow observability upon varying the three geometric angles. We simply define the observability as the number of days for which the afterglow flux is above the average Rubin-LSST nightly magnitude in the r band, that is 24.5. We found that when fixing θ_w and θ_c, the afterglow observability generally decreases as the observer moves off-axis, i.e. when θ_{obs} increases the flux peaks later but also decreases quite rapidly. Then, when fixing θ_c and θ_{obs}, if θ_w increases, meaning that more energy is available in the jet wings, the afterglow flux peaks earlier in time and

gets to higher values. Eventually, if one fixes the observer angle θ_{obs}, and the size of the jet wings (θ_w), then increasing the core angle of the jet θ_c just pushes the flux to higher values with little effect on the light curve shape. These behaviors are mostly as expected when angles stay within reasonable ranges, so we considered this as a nice verification of how the simulation is handling its parameters.

In order to better understand the impact of the geometry, we have further explored the phase space by building several matrices showing the observability in r-band as a function of θ_c and θ_w, for different values of θ_{obs}, and this for a set of isotropic energies and redshifts. These matrices made clear a few important points. First, only the brightest and closest bursts will be observable off-axis: at redshift z=0.1, $E_{iso}=10^{51}$ erg is needed for the afterglow to be observable off-axis for a few days, then at z=1, E_{iso} has to reach 10^{53} erg. Second, as expected, jets with a larger opening angle θ_c or larger wings θ_w are observable for more time, and this observability can reach hundreds of days in the best cases. Third, the overall dependence upon the 3 angles is not trivial, so that although these matrices gave us a hints about what to expect, we shortly ended up limited in our global understanding, i.e. in the context of a large decadal survey.

Short gamma-ray burst population

In order to make progress, we decided to focus our main science case involving nearby short GRBs, for which there should be a possibility to also have gravitational waves detection during the next data taking. Our goal was to get a reasonable set of bursts to work with, in particular to understand better light curve shapes to develop identification filters. We chose reasonable distribution for each parameter of importance and fixed others to average values. For instance, the redshift distribution slightly rises almost linearly from 0 to 0.1 and the isotropic equivalent energy has a Gaussian shape in log scale around 1051 erg similar to the short burst population measured by the Fermi GBM.

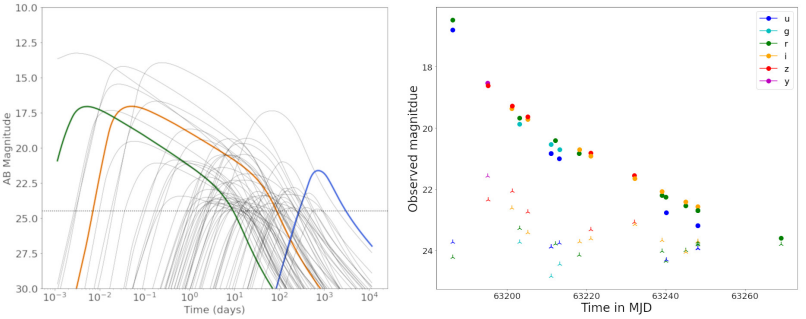

Figure 1: Left, light curves of orphan afterglows of the short gamma-ray burst population that would be observable for more than 7 days with the Rubin observatory ; Right, pseudo-observation of one of the simulated orphan afterglows, realized with the rubin_sim package.

The observer angle was chosen uniform from 0 to 90°, and the truncation angle θ_w was chosen to increase slightly for a few degrees over θ_c and then to go down with a long tail over 20°, meanwhile we decided to stick to 2 single values for the core angle θ_c, 2.86° and 8.60°. Eventually, the circumburst density was chosen to be uniform from 0.001 to 1 particle per cm^3.

We then ran 1000 simulations for both the top-hat jet and the power-law structured jet, kept only off-axis afterglows and computed the observability in r-band. The left side of Figure 1 shows all afterglow light curves of off-axis burst that should be observable more than 7 days by Rubin: 3 light curves are highlighted in colors in order to show the variety of shapes and observability duration. Some afterglows appear to be bright but short, while others will be dim but long: the record holder in our data set could be observable for more than 2000 days. We verified that our production is reasonably realistic by comparing our light curves with the set of (Kann & Klose, 2009). Overall, around 5% of all afterglows end up being observable for more than 7 days, this number varies from 2% to 7% depending upon the jet opening angle and the jet structure: this is clearly in the right ball park, although may be a bit on the lower end of expectations (Ghirlanda et al., 2015). Then we

note that for the power-law structured jet with a θ_c of 8.6°, we find 66 off-axis afterglows for only 49 observed on-axis ($\theta_{obs<}\theta_w$): meaning, that we might just be able to double the statistics of GW-EM associations.

Pseudo observations with the Rubin observatory

We then processed our simulated light curves through pseudo-observations by Rubin using the rubin_sim package that proposes a framework to emulate 10 years of a realistic scheduling of observations including background light, air mass, atmospheric conditions and obviously the filter and camera response. For each burst, we chose a date within the 10 years schedule and a random position in the sky, we then use the afterglowpy to produce a full spectral energy density that is then integrated through the correct filter for each scheduled observation. Through this procedure we obtain pseudo observation of light curves as shown on the right hand side of Figure 1: the burst shown would benefit from a nice coverage over more than 60 days. Pseudo-observations also include an estimation of the limiting magnitude for each observation emulated by the scheduler: these are shown here as small triangles, and we note that there is quite some dispersion depending upon observing conditions, confirming the importance of this step. We are currently analyzing pseudo-observations in order to compute characteristic parameters of the light curves such as average rise and decay time, time of the maximum flux and the average g-r bands color. From these we expect to be able to develop a first rough selection that we wish to then implement in the framework of the FINK broker.

Conclusions

We have simulated gamma-ray burst afterglows in the optical band and studied their light curves when observed off-axis in the context of the Rubin LSST. The large number of parameters defining an afterglow (equivalent isotropic energy, redshift, jet opening angle and structure,

circumburst density) entails that the phase space is too large to be simply characterized. We decided to focus on a population of short nearby gamma-ray bursts, the ones for which a detection of the gravitational wave signal should also be possible by the current generation of detectors. The simulation of afterglow light curves for the short burst population was found useful to verify that indeed Rubin LSST data should contain at least as many off-axis afterglows as on-axis afterglows, even for quite large values of the jet opening angle. With these encouraging results, we are now in the process of analyzing pseud-observation made from these light curves in order to derive selection cuts to filter alerts from variable objects in the FINK broker framework. A lot of work remains ahead to get ready to extract OAs out of Rubin LSST data as the survey should start as soon as end of 2024.

Acknowledgements

We wish to specifically thank the authors of the afterglowpy package for making their code open source and user friendly. This work is supported by the French National Research Agency in the framework of the «Investissements d'avenir» program (ANR-15-IDEX-02).

References

Abbott, B.P., 2017. A gravitational-wave standard siren measurement of the Hubble constant. Nature, vol. 551, no. 7678, pp. 85-88.

Ghirlanda, G., 2015. Unveiling the population of orphan gamma-ray bursts. Astron. Astrophys, vol. 578, A71.

Kann, D.A. and Klose, S., 2009. GRB Afterglows in the ELT Era. Science with the VLT in the ELT Era, vol. 9, p. 233.

Mészáros, P., 2019. Gamma-Ray Bursts: theoretical issues and developments. Memorie della Societa Astronomica Italiana, vol. 90, p. 57.

Möller, A., 2021. FINK, a new generation of broker for the LSST community. Monthly Notices of the Royal Astronomical Society, vol. 501, no. 3, pp. 3272-3288.

Planck, 2020. Planck 2018 results. VI. Cosmological parameters. Astron. Astrophys, vol. 641, A6.

Riess, A.G., 2022. A Comprehensive Measurement of the Local Value of the Hubble Constant with 1 km/s/Mpc Uncertainty from the Hubble Space Telescope and the SH0ES Team. The Astrophysical Journal, vol. 934, no. 1, 2022.

Ryan, G., 2019. Gamma-ray Burst Afterglows in the Multimessenger Era: Numerical Models and Closure Relations. The Astrophysical Journal, vol. 896, n°2.

New 3D white dwarf deflagration models for type Iax supernovae

Fionntan Callan[1], Florian Lach[2,3], Stuart Sim[1], Friedrich Röpke[2,3]

Abstract

Type Iax supernovae (SNe Iax), a sub-class of SNe Ia, are suggested to arise from pure deflagrations of Chandrasekhar mass CO white dwarfs. Here we present new 3D models of Carbon-Oxygen White Dwarf deflagrations (Lach et al., 2022) with varying geometric conditions including ignition radius of the deflagration and central density. We comment on the light curves and spectra produced from this series of models and compare the synthetic observables to the SNe Iax population. Finally, we discuss the possible causes of systematic differences between our model sequence and SNe Iax, the understanding of which are key to supporting or ruling out the pure deflagration scenario.

Key Words

Physics, Astrophysics, Radiative Transfer, Supernovae, White Dwarfs, Hydrodynamics.

[1] Queen's University Belfast, University Road, BT7 1NN, Belfast, UK. Correspondence: fcallan02@qub.ac.uk

[2] Heidelberger Institut für Theoretische Studien, Schloss-Wolfsbrunnenweg 35, D-69118 Heidelberg, Germany.

[3] Zentrum für Astronomie der Universität Heidelberg, Institut für Theoretische Astrophysik, Philosophenweg 12, D-69120 Heidelberg, Germany.

Introduction

Type Ia supernovae (SNe Ia) play a number of key roles in astrophysics. These include contributing substantially to cosmic nucleosynthesis, injecting kinetic energy in galaxy evolution and acting as cosmological distance indicators. Thanks to modern transient surveys it has become clear that type Ia supernovae are a diverse population with many different explosion scenarios proposed to explain normal SNe Ia as well as the various sub-classes. A key theoretical challenge is understanding the origin of this diversity across a wide range of wavelengths and epochs.

Type Iax supernovae are estimated by Foley et al. (2013) to make up approximately 30% of the total SNe Ia rate. SNe Iax show spectroscopic differences to SNe Ia, have generally lower peak magnitudes and also show a much larger spread in their luminosities than normal SNe Ia: the faintest and brightest SNe Iax differ by more than 4 magnitudes at peak. Their infrared (IR) light curves do not show the secondary peak commonly seen in SNe Ia and the long-term evolution is different, potentially suggesting there is some form of luminous bound remnant left behind (see e.g. Foley et al., 2014). This is in agreement with what is predicted by pure deflagration models.

Pure deflagrations of near-Chandrasekhar mass carbon-oxygen white dwarfs (near-MCh CO WDs) have been suggested as a promising explosion scenario to explain SNe Iax: such explosion models have been found to reproduce many of the observed properties of SNe Iax. In this scenario a CO WD accretes matter from a main sequence star in a binary system until it approaches the Chandrasekhar mass limit. At some point a thermonuclear run-away will occur near the centre of the WD. In this pure deflagration scenario the burning front never transitions to moving at a speed greater than the sound speed of the white dwarf (i.e. there is never a transition to a detonation). Pure deflagration models release less energy than those involving a detonation phase, leading to better agreement with the properties of SNe Iax than 'normal' SNe Ia. Multiple studies have been carried out comparing

pure deflagration models for near-MCh CO WDs to SNe Iax. A key challenge that remains is whether it is possible to reproduce the observed diversity of SNe Iax using models of near-MCh CO WDs.

Fink et al. (2014) carried out hydrodynamic explosion simulations followed by a nucleosynthetic post-processing step and finally radiative transfer simulations for a sequence of near-MCh CO WD pure deflagration models. In an attempt to reproduce the observed diversity of the SNe Iax class different numbers of ignition sparks were used to ignite the models. Increasing the number of ignition sparks led to more energetic explosions and brighter events. Fink et al. (2014) found good agreement between their models and brighter members of the SNe Iax class, in particular the colours at peak, decline in blue bands, lack of secondary infrared maximum and presence of IGEs at all times are in agreement with the observed properties of SNe Iax. However, the models declined too quickly in the red bands and the model sequence was unable to reproduce the luminosities of the faint members of the SNe Iax class. Additionally, simmering phase simulations carried out by Zingale et al. (2009) and Nonaka et al. (2012) show that the initial deflagration being ignited by multiple ignition sparks is very unlikely and a single spark ignition is much more likely. This motivated our new study (Lach et al., 2022) in which we aimed to explore whether it is still possible to reproduce many of the observed properties of SNe Iax using models of near-MCh CO WDs ignited using only a single ignition spark. In addition we aimed to determine whether it was possible to produce the observed brightness variation of the SNe Iax class and in particular reach down to the faintest members of the SNe Iax class.

Model setup and numerical simulation pipeline

In order to achieve diversity in the luminosities of our single spark models the two primary initial parameters we varied were the radius of the ignition spark from the centre of the WD and the central density of the WD (see Lach et al., 2022 for details of all parameters we varied).

Once we selected these initial parameters for each model we carried out 3D hydrodynamical explosion simulations using the LEAFS code (Reinecke et al., 1999), followed by a post processing step using the YANN nuclear network code (Pakmor et al., 2012) to calculate nucleosynthetic yields. Finally, we carried out radiative transfer simulations using our 3D time-dependant Monte-Carlo radiative transfer code ARTIS (Sim, 2007; Kromer & Sim, 2009) to allow us to compare synthetic spectra and light curves with observed SNe Iax. We followed this approach for 17 single spark pure deflagration models in our sequence.

Results and discussion

By varying the initial geometric conditions in our explosion models (ignition radius and central density primarily) we were able to achieve significant diversity in luminosity throughout our model sequence, covering a significant portion of the observed brightness diversity of the SNe Iax class (see Fig 17 in Lach et al., 2022). In particular, our new sequence of near-MCh CO WD pure deflagration models is able to reproduce the luminosities of some of the faintest members of the SNe Iax class, extending to over a magnitude fainter at peak in r-band compared to the model sequence of Fink et al. (2014). As Fink et al. (2014) found previously, our models fall on a quasi 1D sequence driven by the mass of 56Ni synthesised in the explosion: the more 56Ni synthesised the brighter the model and the slower the light curves rise and decline. The variation in 56Ni achieved can almost entirely be attributed to variation in ignition radius and central density of the WD, which we vary as initial parameters. In general, higher central densities of the WD and smaller ignition radii lead to more 56Ni being synthesised and brighter models.

We find good agreement between the blue band light curves of our models with bright and intermediate luminosity SNe Iax. However, as was the case for the Fink et al. (2014) model sequence, our model light curves are too fast in decline in the red bands in comparison to

observed SNe Iax. Additionally, the faint models in our sequence show light curve evolution which is too fast in comparison to observed SNe Iax in all bands. This is because while our models show significantly faster light curve evolution as we move to fainter events, this same trend is not observed for SNe Iax. This may suggest our models require more ejected mass for a given mass of 56Ni synthesised. This would slow down the light curve evolution of our models to better match observations as a higher total ejecta mass for a fixed 56Ni mass means the energy injected remains the same but will have to travel through more material in order to escape the ejecta.

We also find the spectroscopic agreement between our single spark models and bright and intermediate luminosity SNe Iax is good. Figure 1 shows comparisons between a bright (blue) and faint (red) viewing angle for one of our models with the intermediate luminosity SNe Iax, SN 2019muj. This spectral comparison is representative of what we generally see when comparing our models to bright and intermediate luminosity SNe Iax. As can be seen from Figure 1 our models have significant viewing angle dependencies which have a noticeable effect on how well our models match observations. Focusing on the brighter viewing angle (blue) which matches the brightness of SN 2019muj better we see at 4 days before B-peak our model provides a very good match to the overall flux profile of SN 2019muj, however our model spectra does produce stronger spectral features at this time. At 2 days after B-peak our model still matches the flux profile of SN 2019muj well but now also provides a good match to the strength and location of spectral features. This change in the agreement of the spectral features between the model and SN 2019muj at different epochs may suggest there is some systematic difference in the spectral evolution between our model sequence and observed SNe Iax. At 11 days post B-peak our model still provides a good match to the spectral features of SN 2019muj, however there is now a poor match to the overall flux profile particularly towards the red wavelengths. This is because of the faster decline post peak of our model compared to SN 2019muj particularly in the red bands, as discussed above.

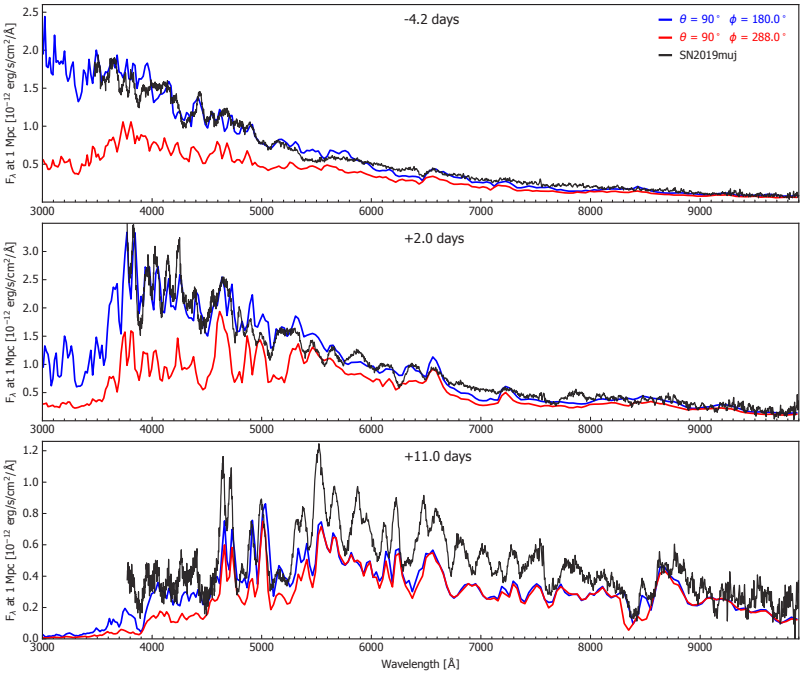

Figure 1: Spectroscopic comparisons in absolute flux between the intermediate luminosity SNe Iax, SN 2019muj (Barna et al., 2021) and two viewing angles for the model from our new sequence which is in best agreement with the luminosity of SN 2019muj. Times are relative to B band maximum.

The systematic difference in spectral evolution mentioned above may be explained by differences in the ionisation and excitation state of the ejecta at earlier times between our models and observed SNe Iax. In these simulations we have used our standard approximate non-LTE treatment of the ionisation and excitation conditions in the ejecta. However, simulations by Shen et al. (2021) have shown for a different class of SNe Ia explosion model there are quantifiable differences in the light curves and spectra when a full non-LTE treatment of ionisation and excitation is used in the radiative transfer simulations. Therefore, carrying out simulations of our models using a full non-LTE treatment of ionisation and excitation may produce ejecta conditions more simi-

lar to the conditions in SNe Iax, leading to better spectroscopic agreement at these earlier epochs. Alternatively, it has been suggested that such systematic differences in the spectral evolution between models and observed SNe Iax could be explained by models with a more stratified ejecta structure (e.g. Stritzinger et al., 2015; Barna et al., 2018). This would exclude pure deflagration models as the scenario which explains SNe Iax as pure deflagrations always produce a well mixed ejecta structure. Magee et al. (2022) however argue that such ejecta stratification in the models is not a requirement to match observed SNe Iax.

Conclusions

Our new model sequence extends to a magnitude fainter at peak compared to the Fink et al. (2014) sequence and can successfully reproduce the luminosities of some of the faintest observed SNe Iax. Additionally we find generally good agreement between the light curves and spectra of our models when compared to bright and intermediate luminosity SNe Iax. However, all models in our sequence decline too fast in the red bands and the faintest models in our sequence show light curve evolution which is too fast in all bands compared to observations, suggesting the ejected mass may be too low. We are currently investigating whether these systematic differences between our models and observed SNe Iax can be resolved by simulating our models using the ARTIS code version developed by Shingles et al. (2020) which has full non-LTE treatment of the ionisation and excitation conditions in the ejecta. The systematic differences may also be improved by taking into account the effect of a possible luminous bound remnant suggested for SNe Iax (and predicted for pure deflagrations) which we do not treat here in the radiative transfer. This bound remnant is predicted to contain material which was burned in the deflagration and has fallen back onto the remnant, some of which will be 56Ni. The radiation emitted due to the radioactive decay of this 56Ni in the remnant has been shown to impact the late time light curve evolution of pure deflagration models

(e.g. Kromer et al., 2013; Shen & Schwab, 2017). We are currently exploring whether such a luminous bound remnant could also help explain some of the systematic differences between the light curves and spectra of our pure deflagration models and those of observed SNe Iax at early times (Callan et al., 2023, in prep). Alternatively, it may be the properties of the deflagration models themselves which is the cause of these systematic differences as suggested by e.g. Stritzinger et al. (2015) and Barna et al. (2018), who argue a more stratified ejecta structure is required to match observed SNe Iax, unlike the well mixed ejecta structure produced by pure deflagrations. However, Magee et al. (2022) argue that such a stratified ejecta structure is not required to match observed SNe Iax. Pure deflagrations of near-MCh CO WDs therefore remain a promising scenario to explain SNe Iax, but the systematic differences when comparing to observations must be resolved if they are to be fully supported as the scenario which explains SNe Iax.

References

Barna, B., Szalai, T., Jha, S.W., Camacho-Neves, Y., Kwok, L., Foley, R.J., Kilpatrick, C.D., Coulter, D.A., Dimitriadis, G., Rest, A., Rojas-Bravo, C., Siebert, M.R., Brown, P.J., Burke, J., Padilla Gonzalez, E., Hiramatsu, D., Howell, D.A., McCully, C., Pellegrino, C., Dobson, M., Smartt, S. J., Swift, J.J., Stacey, H., Rahman, M., Sand, D.J., Andrews, J., Wyatt, S., Hsiao, E.Y., Anderson, J.P., Chen, T.-W., Della Valle, M., Galbany, L., Gromadzki, M., Inserra, C., Lyman, J., Magee, M., Maguire, K., Müller-Bravo, T.E., Nicholl, M., Srivastav, S., and Williams, S.C. 2021. SN 2019muj - a well-observed Type Iax supernova that bridges the luminosity gap of the class. MNRAS, 501(1):1078-1099.

Barna, B., Szalai, T., Kerzendorf, W.E., Kromer, M., Sim, S.A., Magee, M.R., and Leibundgut, B. 2018. Type iax supernovae as a few-parameter family. Monthly Notices of the Royal Astronomical Society, 480(3):3609-3627.

Fink, M., Kromer, M., Seitenzahl, I.R., Ciaraldi-Schoolmann, F., Röpke, F. K., Sim, S.A., Pakmor, R., Ruiter, A.J., and Hillebrandt, W. 2014. Three-

dimensional pure deflagration models with nucleosynthesis and synthetic observables for Type Ia supernovae. MNRAS, 438:1762-1783.

Foley, R.J., Challis, P.J., Chornock, R., Ganeshalingam, M., Li, W., Marion, G.H., Morrell, N.I., Pignata, G., Stritzinger, M.D., Silverman, J.M., Wang, X., Anderson, J.P., Filippenko, A.V., Freedman, W.L., Hamuy, M., Jha, S.W., Kirshner, R.P., McCully, C., Persson, S.E., Phillips, M.M., Reichart, D.E., and Soderberg, A.M. 2013. Type Iax Supernovae: A New Class of Stellar Explosion. ApJ, 767:57.

Foley, R.J., McCully, C., Jha, S.W., Bildsten, L., Fong, W.E., Narayan, G., Rest, A., and Stritzinger, M.D. 2014. Possible Detection of the Stellar Donor or Remnant for the Type Iax Supernova 2008ha. ApJ, 792:29.

Kromer, M., Fink, M., Stanishev, V., Taubenberger, S., Ciaraldi-Schoolman, F., Pakmor, R., Röpke, F.K., Ruiter, A.J., Seitenzahl, I.R., Sim, S.A., Blanc, G., Elias-Rosa, N., and Hillebrandt, W. 2013. 3D deflagration simulations leaving bound remnants: a model for 2002cx-like Type Ia supernovae. MNRAS, 429:2287-2297.

Kromer, M. and Sim, S.A. 2009. Time-dependent three-dimensional spectrum synthesis for Type Ia supernovae. MNRAS, 398:1809-1826.

Lach, F., Callan, F.P., Bubeck, D., Röpke, F.K., Sim, S.A., Schrauth, M., Ohlmann, S.T., and Kromer, M. 2022. Type Iax supernovae from deflagrations in Chandrasekhar mass white dwarfs. A&A, 658:A179.

Magee, M.R., Gillanders, J.H., Maguire, K., Sim, S.A., and Callan, F.P. 2022. An analysis of the spectroscopic signatures of layering in the ejecta of Type Iax supernovae. MNRAS, 509(3):3580-3598.

Nonaka, A., Aspden, A.J., Zingale, M., Almgren, A.S., Bell, J.B., and Woosley, S.E. 2012. High-resolution simulations of convection preceding ignition in Type Ia supernovae using adaptive mesh refinement. ApJ, 745:73.

Pakmor, R., Edelmann, P., Röpke, F.K., and Hillebrandt, W. 2012. Stellar GADGET: a smoothed particle hydrodynamics code for stellar astrophysics and its application to Type Ia supernovae from white dwarf mergers. MNRAS, 424:2222-2231.

Reinecke, M., Hillebrandt, W., and Niemeyer, J.C. 1999. Thermonuclear explosions of Chandrasekhar-mass C+O white dwarfs. A&A, 347:739-747.

Shen, K.J., Blondin, S., Kasen, D., Dessart, L., Townsley, D.M., Boos, S., and Hillier, D.J. 2021. Non-local Thermodynamic Equilibrium Radiative Transfer Simulations of Sub-Chandrasekhar-mass White Dwarf Detonations. ApJ, 909(2):L18.

Shen, K.J. and Schwab, J. 2017. Wait for it: post-supernova winds driven by delayed radioactive decays. The Astrophysical Journal, 834(2):180.

Shingles, L.J., Sim, S.A., Kromer, M., Maguire, K., Bulla, M., Collins, C., Ballance, C.P., Michel, A.S., Ramsbottom, C.A., Röpke, F.K., Seitenzahl, I.R., and Tyndall, N.B. 2020. Monte Carlo radiative transfer for the nebular phase of Type Ia supernovae. MNRAS, 492(2):2029-2043.

Sim, S.A. 2007. Multidimensional simulations of radiative transfer in type ia supernovae. MNRAS, 375:154-162.

Stritzinger, M.D., Valenti, S., Hoeflich, P., Baron, E., Phillips, M.M., Taddia, F., Foley, R.J., Hsiao, E.Y., Jha, S.W., McCully, C., Pandya, V., Simon, J.D., Benetti, S., Brown, P.J., Burns, C.R., Campillay, A., Contreras, C., Förster, F., Holmbo, S., Marion, G.H., Morrell, N., and Pignata, G. 2015. Comprehensive observations of the bright and energetic Type Iax SN 2012Z: Interpretation as a Chandrasekhar mass white dwarf explosion. A&A, 573:A2.

Zingale, M., Almgren, A.S., Bell, J.B., Nonaka, A., and Woosley, S.E. 2009. Low Mach Number Modeling of Type IA Supernovae. IV. White Dwarf Convection. ApJ, 704:196-210.

Simulating the recollimation shocks, instabilities and particle acceleration in relativistic jets

Agnese Costa[1,2], Fabrizio Tavecchio[2], Gianluigi Bodo[3]

Abstract

Among blazar, the extreme BL Lacs (EHBL) are characterized by a peculiar hard high energy peaked emission, that challenges standard leptonic scenario. It was recently argued that electron acceleration due to a series of oblique shocks, likely caused by the confinement of the jet as indicated by 2D simulations, could account for the hard TeV Spectral Energy Distribution (SED) of the EHBL. On the other hand, recent work on 3D MHD simulations of weakly magnetized relativistic jets, reveals that strong recollimation shocks trigger a rapidly growing centrifugal instability (CFI) that leads to the development of strong turbulence, eventually disrupting the multiple-shock structure observed in 2D simulations. Nevertheless, our group observed that the presence of strong turbulence downstream of a recollimation shock suggests another effective acceleration scenario. We are then pursuing a vigorous program of relativistic MHD simulations with the PLUTO code, to study

[1] Università degli Studi dell'Insubria, via Ravasi 2, I-21100, Varese, Italy Correspondence: agnese.costa@inaf.it

[2] INAF - Osservatorio Astronomico di Brera, via E. Bianchi 46, I-23807, Merate, Italy Correspondence: fabrizio.tavecchio@inaf.it

[3] INAF - Osservatorio Astrofisico di Torino, strada Osservatorio 20, I-10025, Pino Torinese, Italy Correspondence: gianluigi.bodo@inaf.it

the morphology and the role of instabilities in EHBL jets. Results from preparatory simulations are in tension with the multiple-shock model and with the 3D simulations of CFI after the recollimation shock. In the latter case, other instabilities might interact with the CFI and alter the dynamics of the jet and the acceleration efficiency.

Key Words

Instabilities; methods: numerical, radiation mechanisms: non-thermal; shock waves; galaxies: jets; gamma-rays: galaxies; Astrophysics - High Energy Astrophysical Phenomena.

Introduction

Relativistic jets expelled by AGNs are the most powerful persistent emitters in the Universe. However, the precise processes through which they dissipate part of their energy flux and convey it to rela- tivistic particles are still elusive. In fact, various mechanisms have been investigated, including Diffusive Shock Acceleration (DSA), magnetic reconnection, stochastic acceleration (SA) due to turbulence. In this framework, the EHBL (Biteau et al., 2020) play a fundamental role for the advancement of our comprehension. In order to explain their peculiar very hard and substantially stable gamma-ray continuum (peaking beyond 1 TeV), various models have been investigated. In 2021 Zech & Lemoine presented an extensive scrutiny of the physical processes potentially at work, eventually arguing that the EHBL emission could be associated with recollimation shocks, driven into the flow by the pressure unbalance with the external confining gas. The observed very hard gamma-ray spectrum of the EHBL with the hardest spectra (such as the prototype 1ES 0229 + 200), however, is recovered only if particles undergo acceleration by more than one shock. This is actually expected, since recollimation is believed to trigger a series of recollimation and reflected shocks (e.g. Komissarov & Falle, 1997), and it is confirmed via 2D simulations (e.g. Fichet de Clairfontaine et al., 2021). This scenario is highly attractive for several reasons. In particular the station-

ary recollimation shock would ensure an almost stable acceleration, accounting for the puzzling weakly variable emission. However, it does not explain why, among all blazar, only EHBL jets should behave in this way. More seriously, the key ingredient mentioned above, namely the existence of more than one shock where particles are energized, is questioned by recent 3D hydrodynamical (HD) and magnetohydrodynamical (MHD) simulations of jet recollimation (Gourgouliatos & Komissarov, 2018; Matsumoto et al., 2021). Without the assumption of axisymmetry, the presence of a rapidly growing instability after the recollimation shock is revealed in hydrodynamical flows, and, even if the magnetic fields can damp the instability, this occurs for values of the magnetization well above those inferred for EHBL jets ($\sim 10^{-3}$ G, e.g. Costamante et al., 2018). This instability causes turbulence downstream of the jet and eventually the disruption of its global structure, preventing the formation of the series of shocks. In light of these results, the acceleration model proposed by Zech and Lemoine (2021) was to be reconsidered. Because of the presence of turbulence and of the effective interplay between DSA and SA, we investigated a hybrid scenario where particles are first accelerated at the recollimation shock, then re-accelerated from the turbulence that has developed, applying it to reproduce the SED of 1ES 0229+200 in Tavecchio et al. (2022). A more accurate treatment has later been done by Sciaccaluga & Tavecchio (2022); nevertheless, existing simulations are inadequate to fully characterize the development of the instability and the level of turbulence injected in the plasma. To shed light on the phenomenology of jet recollimation and on the impact of the recently discovered instability on particle acceleration, we need to perform full 3D relativistic MHD simulations with test-particles.

In the next sections we present the preliminary results of our investigation, obtained from two sets of simulations: 1) a 2D rel-MHD simulation with test particles of a recollimation and a reflection shock, 2a) a preliminary 2D rel-HD simulation of a series of recollimation and reflection shocks, 2b) a 3D rel-HD simulation started from the

results obtained from case 2a, to investigate its instability.

The numerical setup

Simulations are carried out with the state-of-the-art code PLUTO (see Mignone et al., 2007), which is a hybrid-MHD code where the plasma equations are solved together with the transport of test-particles (no back-reaction) that can be injected in the fluid (e.g. Vaidya et al., 2018). Most relevant is the fact that the energy distribution of the test-particles is updated at shocks, as described in Vaidya et al. (2018).

In all three setups we use the linear reconstruction together with the HLLC Riemann solver, and a RK2 time-stepping.

For the rel-MHD case, constrained transport is employed to ensure that $\nabla \cdot B = 0$. We choose the Taub-Matthews equation of state, with enthalpy $\omega = \frac{5}{2}p + \sqrt{\frac{9}{4}p^2 + \rho^2}$ (Mignone et al., 2005). The model follows Bodo & Tavecchio (2018): we consider a relativistic jet, under the parsec scale, in a medium characterized by a power law pressure profile, $p_{ext} = p_0(z/z_0)^{-\eta}$, whose 2D stationary solution is that of a confined jet, for $\eta < 2$ (e.g. Bromberg & Levinson, 2007).

At $t = 0$ we inject the initial setup, which for the 2D configurations corresponds to a cold axisymme- trycal conical jet with $r_{j,0} = \theta_0 z_0$, that moves with Lorentz factor Γ and has luminosity $L_j = \pi r^2_{j,0} v_j \omega_j \Gamma^2$. Boundary conditions are set to outflow at external boundaries and at the end of the jet, while reflective conditions are used at the jet axis in the 2D configurations (1 and 2a), and we user-define the lower boundary, $z_0 = 1$, with the initial conditions. For the magnetized case 1, also a poloidal magnetic field is initialized in the whole domain.

2D relativistic MHD + test-particles

The domain of the first setup is made of 200 x 900 cells corresponding to [0,1.5] x [1,4] scaled to $L_{unit} = 0.1$ pc. The external medium has initial density $\rho_0 = 10^{-16}$ g/cm^3, pressure $p_0 = 1$ dyn/cm^2 and its power law

index is $\eta = 1.8$. The injected jet has Lorentz factor $\Gamma = 30$, opening angle $\theta = 0.1$, luminosity $L_j = 10^{44}$ erg/s and relative pressure $p_{j,0}/p_0 = 0.007$, where $p_{j,0}$ is the proper pressure of the jet at $z = z_0$. The magnetic field at $z = z_0$ is $B_0 = 3 \cdot 10^{-4}$ G.

At each time-step, 2 test-particles per cells are injected, with a negligible number density: $n_{nth} = 10^{-10}$ cm^{-3}. To account for the pre-acceleration stage and the minimum Lorentz factor of the emitting electrons in the EHBL (Zech & Lemoine, 2021), the energy distribution of test-particles is initialized as a power law with index 2 in the range $\gamma_{nth} \in (10^2, 5 \cdot 10^3)$.

The results can be summarized in panel 1a): the trajectory of test-particle "2" is displayed on top on the pressure map calculated at the end of the run. Discontinuities in the pressure identify the shocks (the recollimation and reflection shocks, as highlighted respectively in red and blue), where the particle is deflected following the streamlines. The recollimation shock reaches the axis at $z* = 2.2 z_0$ that corresponds to 0.22 pc. At each shock the particles gain energy following Vaidya et al. (2018) and the relevant sources cited therein. This is shown in panel 1b) via an overplot of the SED carried by test-particle 2. At lower energies and densities the initial SED is plotted in black, then energy is lost adiabatically (up to the green line), until the recollimation shock accelerates the particles, even collecting more particles from the thermal population, up to $\gamma^* = 10^8$. The action of the reflection shock is instead comparable to adiabatic gains and can't be distinguished in this overplot. This shows how a series of 2 shocks can easily fail to provide enough high energy electrons and the hard distribution that would be required for modeling with leptonic inverse Compton the high energy emission of TeV blazar (Zech & Lemoine, 2021). This result is not a counter proof to such a model, but it is in tension.

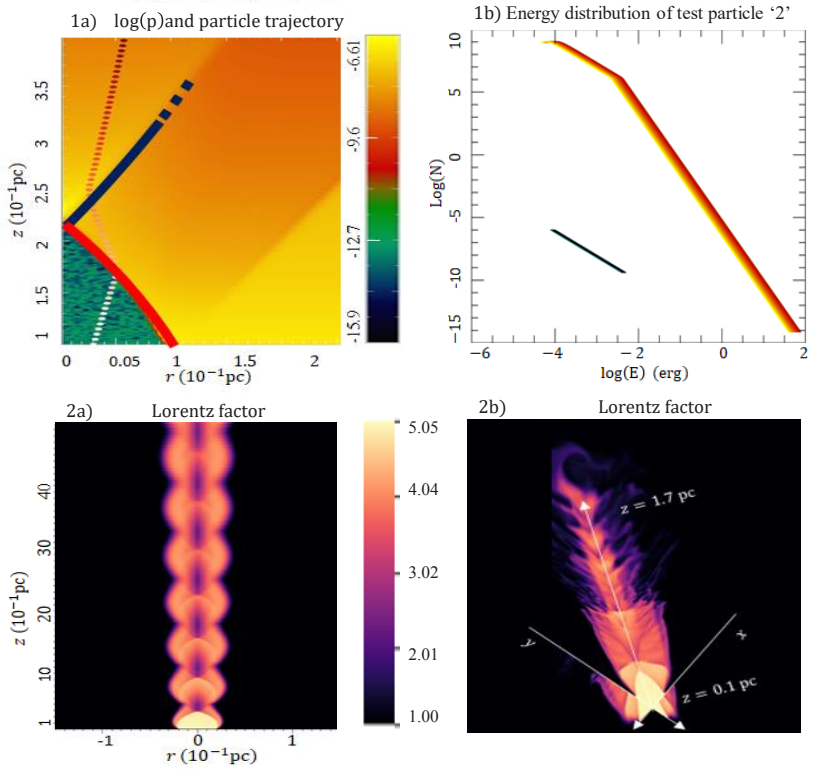

1a) and 1b) refer to the first set of simulations: in 1a the trajectory of a test-particle is displayed on top of the logarithm of the pressure of a 2D section of the jet. In 1b the energy distribution of the test-particle is updated (from black to yellow). Energy is in erg. 2a) represents the Lorentz factor of a 2D steady state of a confined HD jet. The 2D steady state is then projected in 3D and run until t = 60. In figure 2b) a 3-slice (planes x = y, x = –y, z = 17) of the Lorentz factor can be seen in perspective. Some details can be observed, including a recollimation stage made of two shocks, fingers of plasma expanding in the medium, signs of CFI/RTI, and a helical motion of the plasma at z = 17, that points towards the KHI.

3D relativistic HD simulations

The second case consists of two runs. The 2D simulation uses a grid of 350 x 2200 grid points corresponding to [0,20] x [1,50] with unit length L_{unit} = 100 pc. Initial values are chosen to create a stronger con-

finement, so the opening angle is changed to $\theta = 0.2$ and the power law index for the external pressure becomes $\eta = 0.5$. Moreover, in order to compare the results with those of Matsumoto et al. (2021), the initial values of a few quantities are altered to better resemble their setup: $\Gamma = 5$, $L_j = 2 \cdot 10^{44}$ erg/s and $p_0 = 9 \cdot 10^{-9}$ dyn/cm^2, and of course $B = 0$.

The stationary solution is displayed in panel 2a with a map of the Lorentz factor and is that of a series of recollimation and reflection shocks, as expected: the external pressure confines the jet and, as the first recollimation shock reaches the axis ($z* \simeq 3.7$) and the internal pressure increases, a second shock expands outwards. The jet expands until it is confined again, and a series of shocks follow.

The 3D simulation starts from the 2D stationary jet, projected in 3D. The simulation is run for 300 light crossing times of the jet injection radius and the result is displayed in panel 2b as a 3D 3-slice of the Lorentz factor. The morphology of the jet is completely different due to the developing of instabilities. The first recollimation shock happens faster, so it is nearer in z, as expected from Gourgouliatos & Komissarov (2018); there are however differences between our results and those in Gourgouliatos & Komissarov (2018) and Matsumoto et al. (2021). First, in our solution the first recollimation shock splits into two shocks, and the subsequent series is not completely disrupted by turbulence. While in the cited papers the origin of turbulence is found to be in the CFI, a form of the Rayleigh-Taylor instability (RTI), that develops downstream of the recollimation shock; in our setup this instability is probably weaker and there are also signs of the Kelvin-Helmholtz instability (KHI). The KHI, even if damped (Bodo et al., 2004), is probably the agent of the spiraling of the jet at $z \gtrsim 20$. The effect of other instabilities, as the Richtmyer-Meshkov (e.g. Matsumoto & Masada 2019), is to be further investigated, as also suggested from the recent paper of Abolmasov & Bromberg (2022) that shares similarities with our conclusions.

Conclusions

We presented our results for two models of low magnetized jets confined by the pressure unbalance with the external medium: a multiple-shocked jet, that is studied via 2D a rel-MHD simulation, and a recollimated unstable jet, result of a 3D rel-HD simulation. For the first model we also discussed the particle acceleration in a series of 2 oblique shocks, but the conclusion is in tension with the model of Zech & Lemoine (2021). However, the main weakness of the multiple-shock model consists in the instability of the 2D steady state to perturbations in 3D. The structures that form in the xy plane, as observed in the maps of the Lorentz factor obtained via 3D simulations (helical rotation of the jet, fingers penetrating the environment and so on), could not form in 2D axisymmetry, but they grow rapidly and significantly hamper the series of shocks. Despite this conclusion is mainly in accordance with Matsumoto et al. (2021), the details differ considerably. The reason behind this tension, that we do not have with Abolmasov & Bromberg (2022) instead, may be found either in slightly distinct parameters, or in the numerical method Matsumoto et al. used (Komissarov et al., 2015) to determine the steady state of axisymmetric relativistic jets via 1D time-dependent simulations. We leave to future works the conclusions. Finally, while we neglected the magnetic field in the 3D simulations, its action is fundamental for constraining the instabilities and modeling the DSA and SA, so we plan to include diverse configurations of the magnetic field in the next simulations.

References

Abolmasov, P. and Bromberg, O., 2022, in prep. Biteau, J., Prandini, E., Costamante, L., Lemoine, M., Padovani, P., Pueschel, E., Resconi, E., et al., 2020, Progress in unveiling extreme particle acceleration in persistent astrophysical jets. NatAs 4: 124.

Bodo, G., Mignone, A., Rosner, R., 2004. Kelvin-Helmholtz instability for relativistic fluids. PhysRevE 70: 3.

Bodo, G., Tavecchio, F., 2018. Recollimation shocks and radiative losses in extragalactic relativistic jets. A&A 609: A122.

Bromberg, O., Levinson, A., 2007. Hydrodynamic Collimation of Relativistic Outflows: Semianalytic Solutions and Application to Gamma-Ray Bursts. ApJ 671: 678.

Costamante L., Bonnoli G., Tavecchio F., Ghisellini G., Tagliaferri G., Khangulyan D., 2018, The NuSTAR view on hard-TeV BL Lacs. MNRAS 477: 4257.

Fichet de Clairfontaine, G., Meliani, Z., Zech, A., Hervet, O., 2021. Flux variability from ejecta in struc- tured relativistic jets with large-scale magnetic fields. A&A 647: A77.

Gourgouliatos, K.N., Komissarov, S.S., 2018. Reconfinement and loss of stability in jets from active galactic nuclei. NatAs 2: 167.

Komissarov, S.S., Falle, S.A.E.G., 1997. Simulations of Superluminal Radio Sources. MNRAS 288: 833.

Komissarov, S.S., Porth, O., Lyutikov, M., 2015. Stationary relativistic jets. ComAC 2: 9.

Matsumoto, J., Masada, Y., 2019. Propagation, cocoon formation, and resultant destabilization of relativistic jets. MNRAS 490: 4271-4280.

Matsumoto, J., Komissarov, S.S., Gourgouliatos, K.N., 2021. Magnetic inhibition of the recollimation instability in relativistic jets. MNRAS 503: 4918.

Mignone, A., Bodo, G., 2005. An HLLC Riemann solver for relativistic flows - I. Hydrodynamics. MN-RAS: 364, 126-136.

Mignone, A., Bodo, G., Massaglia, S., Matsakos, T., Tesileanu, O., Zanni, C., Ferrari, A., 2007. PLUTO: a Numerical Code for Computational Astrophysics. ApJS 170: 228-242.

Sciaccaluga, A., Tavecchio, F., 2022. Extreme TeV BL Lacs: a self-consistent stochastic acceleration model. MNRAS 517: 2502-2507.

Tavecchio F., Costa A., Sciaccaluga A., 2022, Extreme blazars: the result of unstable recollimated jets?. MNRAS 517: L16-L20.

Vaidya B., Mignone A., Bodo G., Rossi P., Massaglia S., A Particle Module for the PLUTO Code. II. Hybrid Framework for Modeling Nonthermal Emission from Relativistic Magnetized Flows. ApJ 865: 144.

Zech A., Lemoine M., 2021, Electron-proton co-acceleration on relativistic shocks in extreme-TeV blazars. A&A 654: A96.

Physics prospects of KM3NeT

Carla Distefano[1] for the KM3NeT Collaboration

Abstract

KM3NeT is a new generation underwater neutrino observatory with two detectors in the Mediterranean Sea: ARCA, a km^3-scale neutrino telescope dedicated to neutrino astronomy, and ORCA, a Mton scale detector optimized for the measurement of neutrino oscillations. At present, both KM3NeT detectors are taking data with the first detection units deployed. Several studies are currently on-going to validate the performance of the detectors and to improve the data analysis procedures. In this talk we present the status of KM3NeT detectors and results of data analysis by discussing the future perspectives in the coming months with the deployment of new detection units. The expected sensitivities with the full ARCA and ORCA configurations will be also presented.

Key Words

Neutrinos, Astrophysics, KM3NeT.

Introduction

The KM3NeT Collaboration is constructing two neutrino telescopes at distinct locations in the Mediterranean Sea: ORCA (Mton scale,

[1] INFN-Laboratori Nazionali del Sud, via S. Sofia 62, 95123, Catania, Italy. Correspondence: carla.distefano@lns.infn.it

at a depth of 2500 m, offshore Toulon, France) and ARCA (Gton scale, at a depth of 3500 m, offshore Capo Passero, Italy). ARCA is the high-energy component and is dedicated for the search of cosmic neutrino sources in the TeV-PeV range. The main physics objectives for the ARCA telescope are the search for diffuse neutrino fluxes − in particular the investigation of the IceCube findings with better angular resolution and from a complementary field of view − and the search for point-like neutrino sources. Its location in the Northern hemisphere will allow for surveying a large part of the sky, including most of the Galactic Plane and the Galactic Centre. ORCA will be dedicated to the study of atmospheric neutrino oscillations, with the main objective of determining the neutrino mass ordering (NMO), but also low energy neutrino astronomy. The status as of September 2022 of KM3NeT and the prospects of the project will be reported in this paper.

The KM3NeT detectors

The KM3NeT detectors are three dimensional arrays of optical sensors detecting the Cherenkov light induced in water by the secondary charged particles produced in neutrino interactions (The KM3NeT Collaboration, 2016). The arrival times and the amount of the light collected by optical sensors and the positions of the latter are used to reconstruct the path of the secondary particles. From this information the neutrino arrival directions can be inferred, and their energies estimated.

The basic unit of the detectors is the Digital Optical Module (DOM). The DOM is a 17-inch diameter pressure-resistant glass sphere containing 31 3-inch photomultiplier tubes (PMTs) with their associated electronics for digitisation and data transmission as well as the calibration instrumentation. A DOM contains 19 PMTs in the lower hemisphere, and are thus looking downwards, and 12 in the upper hemisphere, looking upwards. This design offers significant improvements with respect to optical modules with a single large-area PMT: the total photocathode area is about three times larger, the field of view

covers almost the full solid angle, pixelization allows for high-purity photon counting and directional sensitivity (The KM3NeT Collaboration, 2022a).

A vertical sequence of 18 DOMs forms a Detection Unit (DU). Two thin parallel ropes hold the DOMs in place. The DU is anchored on the seabed and kept taut by a submerged buoy at its top (The KM3NeT Collaboration, 2020). A vertical 'backbone' cable, running along the full length of the DU, provides connectivity for power and data transmission. The cable is an oil-filled plastic tube, in equi-pressure with sea water, containing electrical wires and optical fibres, with a breakout box at each DOM. A set of 115 DUs, arranged with a roughly circular footprint, forms a 'building block'. ARCA will consist of two building blocks of DUs with 700 m height and horizontally space by 90 m. It will have an instrumented volume of 1 km^3, optimized for the detection of cosmic neutrinos up to energies of the PeV scale. ORCA will consist of one building block of 200 m heighted DUs spaced by 20 m and will have an instrumented mass of 7 Mton. Its high granularity of PMTs will allow the detection of atmospheric neutrinos in the energy range 1-100 GeV. The DUs are connected to junction boxes with a sea network of submarine cables and finally to shore by means of a main electro-optical cable (The KM3NeT Collaboration, 2022b). All data is sent to shore and processed real-time by a computer farm with dedicated trigger algorithms. The KM3NeT detector architecture is intrinsically modular allowing for a staged implementation. Both detectors are under construction and already in data-taking with 21 DUs in operation in ARCA and 11 DUs in ORCA. The data presently collected with the two detectors are being analysed.

The first DUs of the ARCA detector are taking data since December 2015 and the detector achieved a configuration with 6 DUs (ARCA6) in the spring of 2021. The current ARCA21 configuration, achieved in September 2022, exceeds the neutrino detection efficiency of ANTARES, the KM3NeT's predecessor (Ageron, M. et al., 2011) which was recently dismantled after 16 years of operation.

Present results and future perspectives

The data sample at the event reconstruction level is dominated by atmospheric muon background. Quality cuts and direction cuts are then applied to remove it. The event selection is optimized by comparing data with Monte Carlo simulations, carried out on a run-by-run basis to account for temporal variations in data acquisition conditions.

Data acquired with ARCA6 in a live time of 101 days were analyzed. The results obtained are compatible with the background and show the presence of atmospheric neutrinos, at the expected level. Although the results do not show an excess of high-energy neutrinos, the data sample allowed for the optimization and test of the analysis procedures and set the first limits on cosmic neutrino fluxes.

A diffuse neutrino flux is expected from the Galactic ridge due to cosmic-ray interactions with gas and radiation fields. The analysis was performed using the ON-OFF method. The ON region was defined as the portion of the Galactic plane having Galactic Longitude |L_gal| < 40° ang Galactic Latitude |B_gal| < 3°. Nine OFF regions were defined by time-shifting the ON region and avoiding the Fermi Bubble. Eight events were observed in the ON region versus an expected mean background of 4.3 events measured in the OFF regions. The observed excess is not statistically significant, but the upper limit of $6.2 \cdot 10^{-4}$ [$GeV^{-1} \cdot cm^{-2} \cdot s^{-1} \cdot sr^{-1}$] on the diffuse neutrino flux from the galactic ridge has been derived (Sinopoulou, 2022).

Analyses were also conducted to search for point-like astrophysical sources. Two real-time alerts of potential astrophysical neutrinos from the IceCube neutrino observatory have been followed-up with a time window of ±1day: IC211208A, associated with the PKS 0735+17 blazar, and IC220205B, associated with the PKS 1741-03 blazar (Palacios González, 2022). Also in this case, the search was performed using the ON-OFF method. The ON region was defined as a cone centred on the source position and the OFF region was defined as a declination band centred in the source and excluding the ON region. No excess

was reported and only one muon neutrino candidate with E = 18 TeV (p = 0.14) was observed in coincidence with PKS 0735+17 after extending the time window of the search to 1 month (see Figure 1a), as reported in the first Astronomer's Telegram published by KM3NeT (Filippini et al., 2022). Also, a time-integrated point-like source search analysis was performed on the ARCA6 data. The upper limits of the neutrino fluxes were obtained for a list of 46 candidate sources and shown if Figure 1b (Muller, 2022).

A joint analysis with the gamma-ray Cherenkov telescope-array has been carried out, aiming at distinguishing between leptonic and hadronic emission scenarios for selected galactic gamma-ray sources: Vela X, RX J1713.7-3946, HESS J1908+063 and Westerlund1 (Unbehaun, 2022). Many other topics are covered in the analyses conducted with the data acquired with the ARCA detector as the search for dark matter, monopoles and nuclearites.

KM3NeT has received the approval for PNRR funds, the Italian funds for recovery after pandemic. These funds will allow for the completion of the first building block of the ARCA detector and the construction of about 15 DUs of the second one, mounting to a total of 130 DUs funded so far. The PNRR timeline is 3 years and for KM3NeT it is the opportunity to definitively enter the neutrino astronomy game. With two building blocks completed, ARCA can confirm flux measured by IceCube within 1 year of data taking.

The ORCA detector is currently taking data with 11 DUs and obtained funding for about 50 DUs. Data acquired in about a year of ORCA6 operation have been analysed and show the effect due to flavour oscillations as expected. When complete, the ORCA detector will reach unprecedented sensitivity in the measurement of the oscillation parameters. In particular, the sensitivity to determine the NMO after three years of data taking is expected to be 4.4s in the case of normal ordering and 2.3s in the case of inverse ordering (The KM3NeT Collaboration, 2022c).

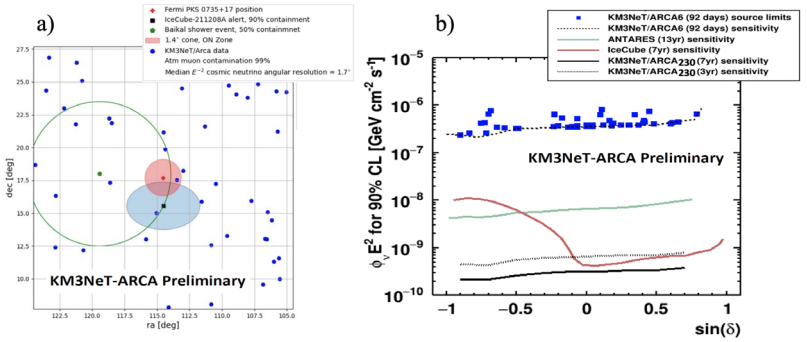

Figure 1. a) Skymap around PKS 0735+17 (see text and Filippini et al., 2022 for major details); b) Upper limits on the cosmic neutrino flux coming from point and extended sources for ARCA, IceCube and ANTARES. Blue squares are limits from individual considered sources.

The capabilities of the detector are not limited to the field of neutrino physics, but also extend to that of low energy neutrino astronomy. ORCA is part of the multimessenger astronomy program of KM3NeT. One of the pilot analyses conducted on the ORCA data concerns the follow-up of gravitational wave (GW) events which allowed to set limits on the neutrino flux for 55 GW events detected during the LIGO-Virgo O3 Observation Run. The flux limits have been set in the GeV-TeV range and at the MeV energies (Le Stum, 2022).

The distance between DOMs in the KM3NeT detectors is too large to individually detect MeV neutrinos. The PMTs see light emitted by electrons produced in inverse beta decay neutrino interactions within 10-20 meter of DOMs. The detection of such low-energy neutrinos is therefore possible by observing the population of coincidences in excess over the background expectation, considering all the DOMs in the detector. This type of analysis is particularly promising for the observation of Core Collapse Supernova events, during which a flux of MeV neutrinos is expected. Statistical analysis of the multiplicity of the detected coincidences in the DOMs shows that ARCA6+ORCA6 are already sensitive to 60% of CCSNe (The KM3NeT Collaboration, 2021). Moreover, an alert system is already operational and KM3NeT is integrated in Super-

Nova Early Warning System (SNEWS) network (Al Kharusi et al., 2021).

In neutrino astronomy there are still no standard candle sources to check the absolute pointing of a telescope. An alternative method is to observe the Moon/Sun shadow, that is the lack of atmospheric muons due to the absorption of primary cosmic rays. The position of the shadow in the sky allows for a check of the detector absolute orientation, while its shape gives a measurement of the angular resolution. ORCA6 data allowed for a test of the applicability of the method in the KM3NeT detectors, providing the first measurement of the angular resolution. Data acquired in a live time of 500 days, were analyzed resulting in an estimated angular resolution of $0.68° \pm 0.12°$ at 6.0σ level from the Sun shadow and $0.54° \pm 0.16°$ at 2.4σ level from the Moon shadow.

Conclusions

KM3NeT will open a new window for neutrino astronomy and the study of fundamental properties of the neutrino, thanks to the complementarity of ARCA and ORCA. ORCA is optimized for the detection of neutrinos with energies of the order of GeV, while ARCA is focused on high neutrino energies, up to and beyond PeV.

The two telescopes are under construction and currently data-taking with 21 and 11 DUs respectively. The data acquired with both detectors are already being analyzed. The first results show the expected performance, both for the measurement of atmospheric muon and atmospheric neutrino fluxes. Although current sensitivities are not yet competitive, a rich variety of pilot analyses is on-going.

KM3NeT has received the approval for PNRR funds (Italian funds for the recovery after the pandemic) having to date funds for 130 ARCA DUs. For ORCA, the Collaboration has funds assured for about 50 DUs. Interesting physics results from KM3NeT are expected in the near future, in particular having the opportunity to definitively enter the neutrino astronomy game.

References

Ageron, M. et al., 2011. The first undersea neutrino telescope. NIM A 656, 11-38.

Al Kharusi, S. et al., 2021. SNEWS 2.0: A Next-Generation SuperNova Early Warning System for Multi-messenger Astronomy. New J. Phys. 23, 03120.

Filippini, F. et al., 2022. Search for neutrino counterpart to the blazar PKS0735+178 potentially associated with IceCube-211208A and Baikal-GVD-211208A with the KM3NeT neutrino detectors. Astronomer's Telegram #15290. https://www.astronomerstelegram.org/?read=15290.

Le Stum, S., 2022. First search for neutrino counterparts from gravitational wave sources with KM3NeT. Poster presented at the Neutrino 2022 Conference. https://zenodo.org/record/6805229.

Muller, R., 2022. Search for cosmic neutrino point sources and extended sources with 6 lines of KM3NeT/ARCA. Poster presented at the Neutrino 2022 Conference. https://zenodo.org/record/6805394.

Palacios González, J., 2022. Follow-up of IceCube alerts with KM3NeT ARCA and ORCA. Poster presented at the Neutrino 2022 Conference. https://zenodo.org/record/6805372.

Sinopoulou, A., 2022. Study of the all-sky diffuse astrophysical neutrino flux and of the Galactic ridge with KM3NeT/ARCA data. Poster presented at the Neutrino 2022 Conference. https://zenodo.org/record/6767724.

The KM3NeT Collaboration, 2016. Letter of intent for KM3NeT 2.0. J. Phys. G: Nucl. Part. Phys. 43: 084001.

The KM3NeT Collaboration, 2020, Deep-sea deployment of the KM3NeT neutrino telescope detection units by self-unrolling, JINST 15 P11027.

The KM3NeT Collaboration, 2021. The KM3NeT potential for the next core-collapse supernova observation with neutrinos. Eur. Phys. J. C 81, 445.

The KM3NeT Collaboration, 2022a. The KM3NeT multi-PMT optical module, JINST 17 P0703 JINST 17 P0703.

The KM3NeT Collaboration, 2022b. KM3NeT Broadcast Optical Data Transport System, arXiv:2210.13328, submitted to JINSTM.

The KM3NeT Collaboration, 2022c. Determining the neutrino mass ordering and oscillation parameters with KM3NeT/ORCA. Eur. Phys. J. C 82, 26.

Unbehaun, T., 2022. Multi-Messenger Analysis of KM3NeT and CTA data to distinguish between leptonic and hadronic emission scenarios. Poster presented at the Neutrino 2022 Conference. https://zenodo.org/record/6785242.

Characterizing the galaxy shape effect on the Euclid slitless spectroscopy using simulations

Louis Gabarra[1,2] *on behalf of the Euclid Consortium*

Abstract

The next generation of wide spectroscopic surveys such as Euclid will scan the sky in the near-infrared to obtain both photometry and spectroscopy. For this purpose, the Euclid telescope will rely on a Near-Infrared Spectrometer and Photometer (NISP) instrument whose spectroscopic channel has been designed to operate in slitless configuration. This powerful and easy to operate configuration makes it possible to avoid any prior selection on the targeted galaxies while covering the entire field of view. Beyond the observed flux of the galaxy, the detector capabilities will strongly depend on the shape of the galaxy, which gets convolved with the galaxy spectra.

To test the effect of the galaxy shape on the quality of the *Euclid* slitless spectra, we have performed simulations testing potentially impactful morphological parameters. We then characterized the effect of the disk half-light radius on the quality of the *Euclid* slitless spectra.

Keywords

Slitless spectroscopy, Euclid, Galaxy shape, Cosmology, Astrophysics.

---

[1] Dipartimento di Fisica e Astronomia "Galileo Galilei", Università di Padova, 35131, Padua, Italy. Correspondence: louis.gabarra@pd.infn.it

[2] INFN, Istituto Nazionale di Fisica Nucleare, Sezione di Padova, 35131 Padua, Italy.

Introduction

The Euclid mission (Laureijs et al., 2011; Racca et al., 2016) whose launch into space is expected for 2023,will scan the extragalactic sky in an under-sampled wavelength range, the near-infrared. This wavelength range provides access to the strong optical rest frame features, e.g., H∝ and [OIII]λ5008 emission, Hβ absorption, up to redshift ≈ 2.5, including the epoch where dark energy started to drive the accelerating expansion of the Universe. This redshift range is also crucial for galaxy evolution studies since it includes the cosmic noon (Madau & Dickinson, 2014), when galaxies were particularly prolific in terms of star-formation. The Euclid Wide survey (Euclid Collaboration: Scaramella et al., 2022) and its spectroscopic channel using the Near-Infrared Spectrometer and Photometer (NISP; Maciaszek et al., 2016) will therefore be of great use to inferphysical parameters such as the star-formation rate, the dust attenuation, and the metallicity of galaxies in this redshift range. The physical parameters estimation inferred from spectroscopy will rely on Euclid ability to reconstruct emission lines. The Euclid Wide survey sensitivity, set at 2×10^{-16} ergs^{-1} cm^{-2} for a 0.25 arcsecradius source at 3.5σ, depends on the background level at the observed coordinates and on the shape of thegalaxy. The latter is particularly important in slitless configuration. In this paper, we investigate the effect ofthe half-light radius of the galaxy on the Euclid capability to detect emission lines.

Justification

Slitless spectroscopy consists in removing any form of mask or slit, leaving the entire field of view (FoV) going through the spectrometer. Euclid slitless spectroscopy will be performed with a set of grisms. The grism is a dispersive and transmissive element in a collimated beam. Wide-field near-infrared slitless spectroscopy was first offered by the HST and now benefits from significant advances with previous studies

on data reduction (Walsh et al., 1979; Pasquali et al., 2006; Ryan et al., 2018), and has therefore been retained to fulfill the Euclid requirements. Slitless spectroscopy benefits particularly from the space environment, getting rid of the telluric OH emission lines and avoiding the atmospheric absorption. Nevertheless, slitless spectra still present several challenges with respect to data reduction. Without any physical aperture restricting the spatial extension of the incoming light, the 2D spectra can be thought of as a convolution of the source and its spatial profile. This feature, while enabling spectroscopic study all over the FoV, is also responsible for potential contamination effects. There can be overlaps between different dispersion orders of different sources and selfcontamination effects due to the finite extension of the observed galaxy, creating a spectral resolution dependance from the shape of the object.

In this work, we tested the effect of the galaxy shape on the quality of the Euclid slitless spectra. To identify the specific effects from the shape, we performed simulations where we ensured that spectra do not overlap, and we focused on the analysis on the first order spectra.

Simulations configuration

Frame and setup. The simulation presented in this work have been done using the NISP spectroscopic pixel simulator (TIPS; Zoubianet al., 2014) that we have configured to mimic an *Euclid* Wide survey (Euclid Collaboration: Scaramella et al. 2022) spectroscopic acquisition, corresponding to an overall exposure time of 2304 s, resulting from four dithered frames of 576 s. These simulations include different sources of noise such as the read-out noise, the dark current, and the zodiacal light diffuse background. The latter is expected to be the dominant background and depends on the pointing coordinates. We chose pointing coordinates representative of a median zodiacal background level.

Input preparation. We produced an input catalog starting from one bright source of the COSMOS field (Laigle et al., 2016) that provided us with the physical parameters for this galaxy relying on multi-wave-

length observations, from UV to far IR, to derive robust spectral energy distribution (SED) fitting parameters. The expected emission line fluxes for the wavelength range of interest were calculated using empirical calibrations available in the literature, i.e., star-formation rate-Hα relation, Baldwin-Phillips-Terlevich (BTP) diagram, mass-metallicity relation (MZR), and photoionization models (see Euclid Collaboration: Gabarra et al, in prep., for details). The resulting SED has then gone through TIPS together with a list of morphological parameters required to reproduce a realistic surface brightness distribution. We tested the effect of some parameters on the quality of the extracted spectra. These parameters are the orientation angle with respect to the dispersion axis, the inclination of the galaxy, the bulge fraction, and the disk half-light radius. In this paper, we report only the results of the simulations changing the disk half-light radius since it was found that this parameter is the one that most affects the quality of the spectra (see Euclid Collaboration: Gabarra et al, in prep.).

Data Analysis.We fitted the continuum with a linear interpolation of the extracted 1D spectra and subtracted it from the spectra. We assumed Gaussian profile for the emission lines and inferred from the fit the flux and full width at half maximum (FWHM). We fixed the central wavelength using the true redshift for each of the lines of interest and left the FWHM and amplitude as free parameters.

Results

We present in Fig. 1.a an overview of the effect of the galaxy size on the extracted spectra by showing the results around the Hα line-complex, i.e., Hα blended with the [NII] doublet, obtained by emulating twice the same spectra but changing the Disk R50 from 0.5 to 1.5 arcsec.

To quantify the effect of the size on the spectral resolution, we present in Fig. 1.b the FWHM of the instrument ($FWHM_{inst}$) measured on the Hα line-complex as a function of the Disk R50. The $FWHM_{inst}$ is obtained by subtracting in quadrature the FWHM of

the incident spectra (due to velocity dispersion) from the FWHM measured on the extracted spectra. This estimate accounted for the blending of the Hα line with the [NII] doublet due to the NISP spectral resolution. To this end we broadened the incident spectrum of an ideal point-like source with a Gaussian filter with FWHM = 25Å. We found that the FWHM of the Hα line-complex is about 1.3 times the FWHM of the single Hα line, and we applied this relation to all the sources. We followed the normalization presented in Pasquali et al. (2006) and normalized the $FWHM_{inst}$ by the Euclid NISP requirement for a 0.25 arcsec radius source ($\Delta\lambda_0$). The expected resolution (R) of the Euclid NISP-S, $R= \lambda/\Delta\lambda_0 > 380$ for a 0.25 arcsec radius source, is taken from Racca et al. (2016). The red line and circles are the median normalized $FWHM_{inst}$ calculated in Disk R50 bins including a fixed number of 50 sources. The error bars are the median absolute deviation (MAD). The solid black line is the result convolving the PSF inferred from the measurement on the NISP ground test campaign images (Costille et al., 2019; Maciaszek et al., 2022; Gillard et al., in prep), i.e., a 50% Encircling Energy radius (EE50) of 0.2 arcsec, with twice the projected disk half-light diameter. The factor two came from the fact that the fixed values for the position angle from the RGS simulator dispersion axis and for the inclination angle of the galaxy are both fixed at 45 degrees.

To evaluate the effect of the size on the quality of the measurement, we characterized the drop of the signal to noise ratio (SNR) as the Disk R50 increases. Results are shown in Fig.1.c for the Hα line-complex flux measurement (in red) and for the continuum flux measurement in the H band (in green) that we normalized by the median SNR of a 0.25 arcsec Disk R50 source. The lines and circles show the median normalized SNR calculated on Disk R50 bins including a fixed number of 50 sources. The error bars show the MAD.

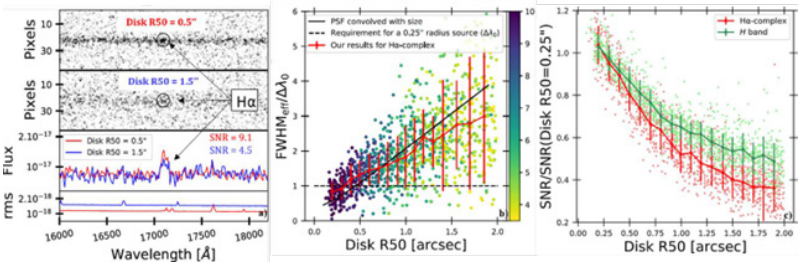

Figure 1. a) Illustration of the disk half-light radius effect on the quality of the spectra. The top two panels are the 2D simulated spectra obtained for the same input spectra with two different sizes, 0.5 and 1.5 arcsec. The bottom two panels are the flux and root mean square (rms). The red line indicates measurements on the 1D combined spectra 0.5 arcsec radius source while the blue line is for the 1.5 arcsec source. b) The spectral resolution measured on the extracted Hα line-complex as a function of the object Disk R50 in arcsec. The spectral resolution has been measured on a sample of 1248 sources with all morphological parameters set at a fixed value except forthe Disk R50 that varies from 0.1 up to 2 arcsec. The red line shows the median normalized $FWHM_{inst}$ calculated on Disk R50 bins including a fixed number of 50 sources. The error bars show the median absolute deviation (MAD). The solid black line shows the model (see explanation in the text). c) SNR of the extracted Hα line-complex measurements (red) and extracted continuum measurements (green) normalized by the median SNR for sources with a disk half-light radius (R50) of 0.25 arcsec as a function of the Disk R50. The lines and error bars shows the normalized median SNR and MAD values calculated on Disk R50 bins including a fixed number of 50 sources. More details in Euclid Collaboration: Gabarra et al., in prep.

Conclusions

We showed that the disk half-light radius has a significant effect on the quality of the extracted slitless spectra and on our ability to detect emission lines. The $FWHM_{inst}$ scales as the Disk R50, degrading redshift determination accuracy and SNR. Beyond the almost linear degradation of the spectral resolution as the Disk R50 increases, we can observe in Fig. 1.b that the MAD significantly increases for sources with Disk R50 > 0.5 arcsec. We can also see that our measurements agree with the requirement set for a 0.25 arcsec radius source and with the expectation from the model. We characterized the effect of the disk half-light radius on the SNR and we showed that there is an almost linear drop of

the SNR as the size increases, to reach a median degradation of ≈45% for emission line and ≈35% for continuum measurements for a source with Disk R50 equal to 0.1 arcsec compared to a 0.25 arcsec source.

Acknowledgements

The author thanks Chiara Mancini, Lucia Rodríguez-Muñoz, Giulia Rodighiero, Chiara Sirignano, Marco Scodeggio and Margherita Talia for their help in shaping this work. The Euclid Consortium acknowledges the European Space Agency and a number of agencies and institutes that have supported the development of Euclid, in particular the Academy of Finland, the Agenzia Spaziale Italiana, the Belgian Science Policy, the Canadian Euclid Consortium, the French Centre National d'Etudes Spatiales, the Deutsches Zentrum für Luft- und Raumfahrt, the Danish Space Research Institute, the Fundação para a Ciência e a Tecnologia, the Ministerio de Ciencia e Innovación, the National Aeronautics and Space Administration, the National Astronomical Observatory of Japan, the Netherlandse Onderzoekschool Voor Astronomie, the Norwegian Space Agency, the Romanian Space Agency, the State Secretariat for Education, Research and Innovation (SERI) at the Swiss Space Office (SSO), and the United Kingdom Space Agency. A complete and detailed list is available on the Euclid web site (http://www.euclid-ec.org).

References

Costille, A., Carle, M., Prieto, E., et al. 2019. Testing NISP instrument on ground, Proc. SPIE, 11180-7L Euclid Collaboration: Scaramella, R., Amiaux, J., Mellier, Y., et al. 2022, A&A, 662, A112.

Kümmel, M., Walsh, J.R., Pirzkal, N., Kuntschner, H., and Pasquali, A. 2009. PASP, 121, 59.

Laigle, C., McCracken, H.J., Ilbert, O., et al. 2016. ApJS, 224, 24.

Laureijs, R., Amiaux, J., Arduini, S., et al. 2011. arXiv:1110.3193.

Maciaszek,T., Ealet, A., Jahnke,K., et al. 2016. in Space Telescopes and

Instrumentation 2016: Optical, Infrared, and Millimeter Wave, ed. H.A. MacEwen, G.G. Fazio, M. Lystrup, N. Batalha, N. Siegler, and E.C.Tong, Vol. 9904, International Society for Optics and Photonics (SPIE), 298.

Maciaszek,T., Ealet, A., Gillard,W., et al. 2022. Euclid near-infrared spectrometera nd photometer instrument flight model presentation, performance, and ground calibration results summary,Proc.SPIE,12180-1K.

Madau, P. and Dickinson, M., 2014. Cosmic Star-Formation History. ARA&A, Volume 52, 415.

Pasquali, A., Pirzkal, N., Larsen, S., Walsh, J., and Kümmel, M. 2006, PASP, 118, 270.

Racca, G.D., Laureijs, R., Stagnaro, L., et al. 2016, in Society of Photo-Optical Instrumentation Engineers (SPIE) Conference Series, Vol. 9904, Space Telescopes and Instrumentation 2016: Optical, Infrared, and Millimeter Wave, ed. H.A. Mac Ewen, G.G. Fazio, M. Lystrup, N. Batalha, N. Siegler, E. C. Tong, O., Ryan, R.E., Casertano, S. and Pirzkal, N., 2018. PASP, 130, 34501.

Walsh, D., Carswell, R.F. and Weymann, R.J., 1979. Nature, 279, 381.

Zoubian, J., Kümmel, M., Kermiche, S., et al. 2014. in Astronomical Society of the Pacific Conference Series,Vol. 485, Astronomical Data Analysis Software and Systems XXIII, ed. N. Manset and P. Forshay, 509.

Quantum noise reduction in gravitational wave interfermometers

Barbara Garaventa[1] *and the Virgo collaboration*

Abstract

The sensitivity of gravitational wave detectors is ultimately limited by the quantum noise, which arises from the quantum nature of light and it is driven by vacuum fluctuations of the optical field entering from the dark port of the interferometer. One way to improve the sensitivity is to inject squeezed vacuum into the dark port, with reduced phase fluctuations (frequency-independent squeezing). At the same time, due to the Heisenberg's uncertainty principle, the amplitude fluctuations are larger and we need to produce frequency-dependent squeezing to achieve a broadband mitigation of quantum noise. This paper shows quantum noise reduction methods that have already been implemented in current interferometers and those that will be introduced in future gravitational wave detectors.

Key Words

Physics, Astrophysics, Quantum Optics, Gravitational Wave, Interferometer.

[1] Physics Department-University of Genoa, INFN Genoa, via Dodecaneso 33, Genoa, Italy Correspondence: barbara.garaventa@ge.infn.it

Introduction

Gravitational waves (GW) are ripples in spacetime due to violent astrophysics events predicted in 1916 by Albert Einstein with the theory of General Relativity. The first direct observation was in 2015 (GW150914). Today, 90 events have been observed by the LIGO and Virgo interferometers in three scientific runs. Laser interferometry is used to detect the very small perturbations ($\Delta L \sim 10\text{-}18$ m) given by the passage of a gravitational wave on the optical path of the light that is moving back and forth between test masses. In order to improve the sensitivity of the GW detectors, many sources of noise need to be mitigated (see Fig.1a). This paper will focuses on the quantum noise mitigation by injecting squeezed states of light into the GW interferometers, in particular frequency-dependent squeezing (FDS) techniques.

Quantum noise

Gravitational wave effects on the test masses can be confused with the effect of vacuum fluctuations of the optical fields that enter the dark port of the detector. Quantum noise affects the entire bandwidth of the GW interferometers (10Hz-10KHz) with its complementary features: at low frequencies, the vacuum amplitude fluctuations dominates (radiation pressure noise); at high frequency, the phase fluctuations of the optical field disturb the detector (shot-noise). Considering the electro-magnetic field in terms of amplitude and phase quadratures, laser light can be described by coherent states, whose quantum uncertainty is depicted with a circle around its amplitudes. Squeezed states of light have a quadrature fluctuation reduced for at least one angle (squeeze angle) and their quantum uncertainty is depicted with an ellipse around their amplitude (squeezing ellipse). Squeezed beams are generated by nonlinear optics and are detected by the homodyne detector technique. Due to Heisenberg uncertainty principle, the decrease of a quadrature leads to an increase of noise in the orthogonal quadrature

(anti-squeezing). In order to improve the sensitivity of the GW detectors, a FDS injection is needed. The following sections will explain the frequency-dependent squeezing achieved by a detuned filter cavity and by an alternative method using Einstein-Podolsky-Rosen (EPR)

Entangled beams

Quantum noise mitigation: Filter cavity in Advanced Virgo Plus

During the O3 observative run, Advanced Virgo injected a frequency-independent squeezing (FIS) into the interferometer, improving the sensitivity curve at high frequencies. Since for the next observation run it is necessary to mitigate quantum noise in the entire bandwidth, Advanced Virgo Plus (AdV+, the upgrade of Advanced Virgo) installed a detuned cavity to achieve a frequency-dependent squeezing. The FDS conceptual design is shown in Fig.1b: the external in air bench hold the squeezing source by a degenerate OPO (Optical-Parametric-Oscillator) to produce FIS; two suspended in-vacuum benches are used to align beams inside the filter cavity, that is detuned with respect to the resonant frequency of the GW interferometer to achieve the rotation of the squeezing ellipse (FDS generation, see Fig.1c) and then reflected from detuned optical cavities into the interferometer; the two other external in-air benches are used for the control loops. However, since squeezed states strongly suffer from optical losses, the round trips inside filter cavity has to be minimized. To ensure that, the cavity bandwidth is of the order of the detection bandwidth, filter cavities have to be long in the order of 100 m and thus represent complex systems to build, maintain and control (for AdV+ it is 285m long).

Quantum noise mitigation: EPR entangled beams

An alternative method for the future gravitational wave detectors to achieve a broadband noise reduction below the standard quantum limit is to use a pair of squeezed EPR entangled beams to produce FDS by a

non-degenerate OPO. EPR experiment produces two beams detuned with respect to each other: one has the frequency of the interferometer (signal), the other (idler) perceives the interferometer like a detuned filter cavity (see Fig.1d). Since these beams are entangled, i.e. their noise sidebands are correlated to each other, once one beam is detected, information about the other is obtained as well (and vice versa). Therefore, the interferometer is both the GW detector and the filter cavity, eliminating the need for external cavity. This method is less expensive, more compact setup and avoids the 1ppm/m round trip losses for the

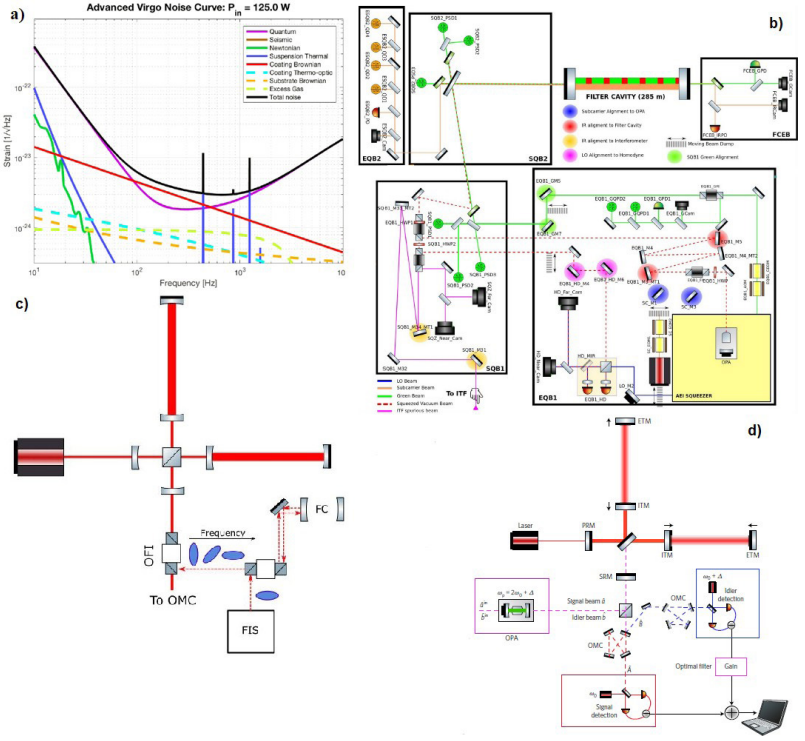

Figure 1. a) shows design sensitivity curve of Advanced Virgo; b) shows the FDS conceptual design in AdV+; c) shows the schematic injection of FDS achieved by a detuned filter cavity from the darkport of the interferometer; d) shows the schematic optical setup of the EPR experiment.

filter cavity, but on the other side two squeezed beams imply double losses and the need for two homodyne detectors.

Conclusions

For next observative run frequency-dependent squeezing is required in order to mitigate quantum noise in the entire bandwidth of the GW interferometer. FDS injection allows to explore a portion of the universe 10 times larger than the last observation run. In Advanced Virgo Plus the squeezing system with the installation of the filter cavity has been completed and FDS measurements have been made with the external homodyne below 50 Hz of cavity detuning. The next step will be to inject FDS into the interferometer. For the EPR experiment, the optical bench located in an R&D laboratory at EGO site is being installed, the optical design has been completed.

Acknowledgements

I would like to thank the quantum noise team for AdV+ and for EPR experiment.

References

Physics Report – Schnabel, R. 2017. Squeezed states of light and their application in laser interferometers. Physics Report 684, 0370-1573.

Physics Report – Ma, Y., Miao, H., Pang, B. et al. 2017. Proposal for Gravitational-Wave Detection Beyond the Standard Quantum Limit via EPR Entanglement. Nature Phys 13, 776-780.

Physics Report – LIGO Scientific Collaboration and Virgo Collaboration. 2016. GW150914: First results from the search for binary black hole coalescence with Advanced LIGO. Physical Review D, 93 (12).

GWFAST: a tool to explore the capabilities of third-generation gravitational-wave interferometers

Francesco Iacovelli[1], *Michele Mancarella*[1], *Stefano Foffa*[1], *Michele Maggiore*[1]

Abstract

We review GWFAST, a Fisher information matrix Python code for gravitational-wave studies, mostly suitable for third-generation ground-based gravitational wave detectors, such as Einstein Telescope and Cosmic Explorer. After discussing the need for fast and accurate parameter estimation codes like GWFAST, we briefly introduce its main functionalities, and present one example of usage.

Key Words

Gravitational Waves, Astrophysics, Fisher-matrix code, Third-generation detectors.

Introduction

The first detection of gravitational waves (GWs) performed by the LIGO detectors in September 2015 (Abbott et al., 2016) opened a new window on our Universe. After a few years from this scientific milestone, the number of detected GW signals emitted from coalesc-

[1] Département de Physique Théorique and Gravitational Wave Science Center, Université de Genève, 24 quai Ernest Ansermet, 1211 Genève 4, Switzerland Correspondence: francesco.iacovelli@unige.ch

ing binary systems is now about 90 (Abbott et al., 2021a) and gives us the possibility e.g., to start understanding the distribution of compact objects in the Universe (Abbott et al., 2021b). The possibilities offered by second-generation (2G) instruments, namely LIGO, Virgo and KAGRA, are already outstanding, and the next step will be third-generation (3G) detectors, Einstein Telescope, ET, in Europe (Punturo et al., 2010; Hild et al., 2011, Maggiore et al., 2020) and Cosmic Explorer, CE, in the U.S. (Reitze et al., 2019; Evans et al., 2021), whose scientific potential is unprecedented. Assessing the capabilities of such instruments, both alone and in a network, is a fundamental requirement in order to understand which are the optimal configurations and make informed choices. One of the key metrics to evaluate the performance of 3G instruments is constituted by the distribution of signal-to-noise ratios (SNRs) and parameter estimation (PE) errors for coalescing binaries. A fundamental challenge in this direction is that full Bayesian PE analyses are computationally demanding even on a single event, and ET and CE are expected to observe up to 10^5 signals per year. For this reason, in recent years various groups developed independently codes based on the Fisher information matrix (FIM) formalism (see e.g., Vallisneri 2008), which can deal with such high numbers of detections in a reasonable amount of time. In particular, the public ones are GWBENCH (Borhanian, 2021) and GWFish (Harms et al., 2022) (see also TiDoFM (Li et al., 2022) and Pieroni et al., 2022). The latest code released by the time of writing is GWFAST (Iacovelli et al., 2022a, b) (the code is publicly available at https://github.com/CosmoStatGW/gwfast), which is particularly suitable to handle large catalogs of events thanks to its vectorization capabilities and is also accurate thanks to the use of automatic differentiation (AD) to compute derivatives. These codes have been cross-checked in the context of the activities of the ET Observational Science Board (OSB), finding good agreement, and have been used to produce various science cases that focus on different aspects of 3G science (Borhanian & Sathyaprakash, 2022, Ronchini et al., 2022, Iacovelli et al., 2022a).

Third-generation ground-based GW detectors

Third-generation detectors represent the next long prepared step of ground-based GW science: thanks to an increase by about one order of magnitude in sensitivity as compared to LIGO, Virgo and KAGRA, and a larger bandwidth especially towards low frequencies, ET and CE will have outstanding capabilities, and dominate the scientific landscape for many years. ET (Punturo et al., 2010; Hild et al., 2011, Maggiore et al., 2020) will feature an innovative triangular design, so being able e.g., to disentangle both GW polarizations, and to observe the whole sky without blind spots. Each arm will consist of two instruments in a 'xylophone' design, one optimized for high-frequency efficiency, and one for low frequencies, thanks especially to cryogenics. Also, the detector will be built more than a hundred meters underground, further mitigating the low frequency noise. ET has recently been included in the ESFRI roadmap, and the ET collaboration has formally been created a few months ago. CE (Reitze et al., 2019; Evans et al., 2021) instead will consist of two separate L-shaped detectors, one 40km long and the other 20km long, that will feature a tunable design, that can be optimized e.g., for compact binaries observations or to observe the post-merger phase of binary neutron star mergers.

GWFAST in a nutshell

GWFAST is based on the FIM formalism, which provides an approximation of the full likelihood for a PE holding in the high SNR limit: the basic idea is that, near a maximum, the likelihood can be approximated by a multivariate Gaussian distribution, with covariance given by the inverse of the Fisher matrix, defined as

$$\Gamma_{ij} \equiv 4Re\left\{\int_0^\infty df \frac{\widetilde{h_i^*}\widetilde{h_j}}{S_n(f)}\right\},$$

where $\widetilde{h_i}$ denotes the derivative of the Fourier domain signal of a GW event with respect to the parameter i, and $S_n(f)$ the noise power spectral density (PSD) of the detector.

Exploiting this formalism, it is possible to perform PE studies greatly lowering the number of required operations, with the key ingredient being the computation of the signal derivatives. To perform this operation, GWFAST adopts AD through the JAX library (https://github.com/google/jax), which is a technique alternative to finite differences to compute derivatives of functions in closed form in a pseudo-analytical way: the function is decomposed in its elementary operations and functions, whose derivative is known, and the derivative is obtained through repeated application of the chain rule, thus performing a number of operations comparable to the one of the original function (see Margossian, 2018 for a review). The fundamental requirement for this to work is to have a pure Python code, otherwise the AD interface would not understand the operations being used inside the function whose derivatives have to be computed. To fulfill this requirement, GWFAST features a pure Python implementation of the waveform models, needed to compute the actual GW signal from the events' parameters (these are also publicly released separately at https://github.com/CosmoStatGW/WF4Py), and the functions to project this signal onto the detector, including the effect of Earth's rotation (which is relevant for 3G detectors, that can observe signals up to $\mathcal{O}(1\ day)$ long). This also allows to fully exploit Python's vectorization capabilities, i.e., the possibility to perform the computation for multiple events per time, even on a single CPU, without resorting to for loops (which are a slow operation in Python), resulting in a considerable gain in terms of computational speed, especially when dealing with large catalogs of events. To further push the computational performance and accuracy, derivatives with respect to some of the parameters are computed analytically. Moreover, GWFAST features a module for parallel computing over multiple CPUs, suitable also for clusters. It is worth mentioning that GWFAST also features the possibility to exploit all the waveform

models implemented in the LIGO Algorithm Library (LAL, https://git.ligo.org/lscsoft/lalsuite), in which case derivatives are computed using the numdifftools library (https://pypi.org/project/numdifftools/).

The inversion of the FIM, needed to obtain the covariance matrix can be performed in various ways within GWFAST, as this can be a delicate operation if the conditioning of a matrix is poor (i.e., the ratio of the absolute values of the smallest and the biggest eigenvalues is smaller than the machine precision). To partially alleviate this issue, GWFAST exploits the mpmath library for precision arithmetic (https://mpmath.org), and features functions to compute the reliability of the inversion, as well as to manipulate the matrix, e.g., fixing some of the parameters, adding Gaussian priors or computing the localization region of an event.

A GWFAST example

As an example of usage for GWFAST we consider a population of binary black hole (BBH) systems analogous to the one adopted in Iacovelli *et al.*, 2022a, and based on the latest results from LIGO, Virgo and KAGRA (Abbott *et al.*, 2021b), namely: the *POWER LAW+PEAK* distribution for the source masses, the *DEFAULT* distribution for the spins, a Madau-Dickinson profile (Madau & Dickinson 2014) for the merger rate with typical parameters (Madau & Fragos 2017), and uniform distributions for the remaining parameters (see App. A of Iacovelli et al., 2022a for details on the parameters and functional forms of the distributions). With these choices, the total number of mergers out to redshift 20 in one year is about 75000, an extremely prohibitive number for a Bayesian PE code to analyze. We perform the analysis for three different detector configurations: a network constituted by the two LIGO detectors, Virgo and KAGRA during the upcoming fourth observing run (O4) (the sensitivity curves are available at https://dcc.ligo.org/LIGO-T2000012/public); a single ET detector (the sensitivity curve for ET is available at https://apps.et-gw.eu/tds/?content=3&r=14065) and

a network made up of ET and two CE detectors (the sensitivity curves for CE are available at https://dcc.cosmicexplorer.org/CE-T2000017/public). We report a selection of the results in Fig. 1 where, for each configuration, in the top panels we show the distribution of detections as a function of the total source-frame mass of the systems, while in the bottom panels we report the measurement errors attainable on the total source-frame mass and effective spin parameter

$$\chi_{eff} = \frac{m_1\chi_{1,z} + m_2\chi_{2,z}}{M_{tot}},$$

where $X_{i,z}$ denote the adimensional spin component of the object i aligned with the orbital angular momentum and M_{tot} the total source-frame mass. As it is apparent from the top row plots, while at 2G detectors there will be only a handful of events, with 3G instruments we will be able to probe the full mass range thanks to the impressive number of detections, reconstructing e.g., its edges, whose determination, other than the relevance for population studies, has been understood to provide a key observable for Cosmology (Ezquiaga & Holz, 2022). From the plots in the bottom row, we instead notice the exquisite accuracy attainable on the mass and spin parameters, whose determination is fundamental to characterize the population of merging black holes and e.g. reconstruct their formation and evolution history, or disentangle them from a possible primordial black hole component (De Luca et al., 2020).

Conclusions

In this work we presented GWFAST a Fisher matrix tool to characterize the capabilities of 3G ground-based GW detectors, the next long-prepared leap of GW science. Thanks to its features, described in Sect. 3, we are confident this code will provide a fundamental tool for the community for the years to come. As an example, in Sect. 4 we used GWFAST to predict the error measurement on a population of

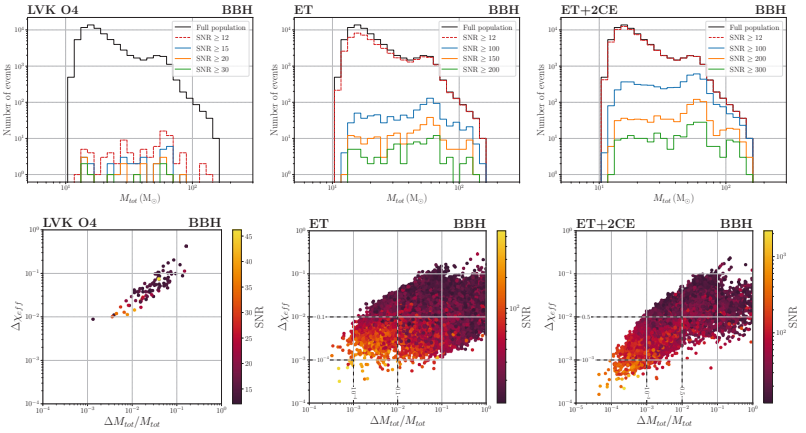

Figure 1: In the top row we report the total source-frame mass distribution of the BBH events detected in one year, with various cuts in SNR, for the LIGO, Virgo and KAGRA detectors during O4 (left panel), a single ET detector (central panel) and a network of ET and 2 CE (right panel). In the bottom row we report scatter plots of the measurement errors attainable on the effective spin parameter and total source-frame mass (relative error), with a color code that gives information on the SNR, at the same detector networks as in the top row. The numbers on the dashed lines report the fraction of events in the regions they delimit.

BBH systems both at 2G and 3G instruments, focusing on the mass and spin parameters, whose precise determination for a large number of sources, only attainable at 3G detectors, is of pivotal importance both for Astrophysical and Cosmological studies.

Acknowledgements

The research leading to the results shown has been conceived and developed within the activities of the ET Observational Science Board. F.I. acknowledges support from Istituto Svizzero, through the Milano Calling fellowship. Our research is supported by the Swiss National Science Foundation, grant 200020_191957, and by the SwissMap National Center for Competence in Research. Computations made use of the Yggdrasil cluster at the University of Geneva.

References

Abbott, B.P. et al. (LIGO Scientific Collaboration and Virgo Collaboration), 2016. Observation of Gravitational Waves from a Binary Black Hole Merger. Phys. Rev. Lett. 116, 061102.

Abbott, R. et al. (LIGO Scientific Collaboration, Virgo Collaboration, KAGRA Collaboration), 2021a. GWTC-3: Compact Binary Coalescences Observed by LIGO and Virgo During the Second Part of the Third Observing Run. arXiv:2111.03606.

Abbott, R. et al. (LIGO Scientific Collaboration, Virgo Collaboration, KAGRA Collaboration), 2021b. The population of merging compact binaries inferred using gravitational waves through GWTC-3. arXiv:2111.03634.

Borhanian, S., 2021. GWBENCH: a novel Fisher information package for gravitational-wave benchmarking. Class. Quantum Grav. 38 175014.

Borhanian, S. and Sathyaprakash, B.S., 2022. Listening to the Universe with Next Generation Ground-Based Gravitational-Wave Detectors. arXiv: 2202.11048.

De Luca, V., et al., 2020. Primordial Black Holes Confront LIGO/Virgo data: Current situation. JCAP06(2020)044.

Evans, M., et al., 2021. A Horizon Study for Cosmic Explorer: Science, Observatories, and Community. arXiv: 2109.09882.

Ezquiaga, J.M., and Holz, D.E., 2022. Spectral Sirens: Cosmology from the Full Mass Distribution of Compact Binaries. arXiv: 2202.08240.

Harms, J., et al., 2022. GWFish: A simulation software to evaluate parameter-estimation capabilities of gravitational-wave detector networks. arXiv:2205.02499.

Hild, S., et al., 2011. Sensitivity studies for third-generation gravitational wave observatories. Class. Quantum Grav. 28 094013.

Iacovelli, F., et al., 2022a. Forecasting the detection capabilities of third-generation gravitational-wave detectors using GWFAST. arXiv:2207.02771.

Iacovelli, F., et al., 2022b. GWFAST: a Fisher information matrix Python code for third-generation gravitational-wave detectors. Astrophys. J. Supp. 263, 1, 2.

Li, Y., et al., 2022. Exploring the sky localization and early warning capabilities of third generation gravitational wave detectors in three-detector network configurations. Phys. Rev. D 105, 043010.

Madau, P,. and Dickinson, M., 2014. Cosmic Star Formation History. Ann. Rev. Astron. Astrophys.Vol 52: 415-486.

P. Madau and T. Fragos, 2017. Radiation Backgrounds at Cosmic Dawn: X-Rays from Compact Binaries. Astrophys. J. 840, 1, 39.

Maggiore, M., et al., 2020. Science case for the Einstein telescope. JCAP03(2020)050.

Margossian, C.C., 2018. A Review of automatic differentiation and its efficient implementation. WIREs Data Mining Knowl Discov. 9:e1305.

Pieroni, M., et al., 2022. Detectability and parameter estimation of stellar origin black hole binaries with next generation gravitational wave detectors. arXiv:2203.12586.

Punturo, M., et al., 2010. The Einstein Telescope: a third-generation gravitational wave observatory. Class. Quantum Grav. 27 194002.

Reitze, D., et al., 2019. Cosmic Explorer: The U.S. Contribution to Gravitational-Wave Astronomy beyond LIGO. Bulletin of the AAS, 51(7).

Ronchini, S., et al., 2022. Perspectives for multi-messenger astronomy with the next generation of gravitational-wave detectors and high-energy satellites. Astron. Astrophys. 665 (A97)

Vallisneri, M., 2008. Use and abuse of the Fisher information matrix in the assessment of gravitational-wave parameter-estimation prospects. Phys. Rev. D 77, 042001.

Measuring the β-decay properties for exotic rare-earth isotopes

Sándor Kovács[1,2], András Vitéz-Sveiczer[1,2], Gábor Gyula Kiss[2]

Abstract:

Many questions remain open even after the observation of the GW170817 event regarding the astrophysical environment of the r-process. A key factor in the comparability of observations and theories is the nuclear properties of the isotopes synthesized during the explosion, which are not or only poorly known. Recently, in experiments at the RIKEN Nishina Center, we have significantly extended the existing β-decay half-life ($T_{1/2}$) and delayed neutron emission probability (P_n value) database. It was shown that these data are essential for understanding the formation of the so-called rare-earth r-process abundance peak (REP). Using the ^{162}Pm isotope as an example, the main steps of the analysis are presented.

Keywords

Nuclear astrophysics, r-process, rare-earth abundance peak, half-life, delayed neutron emission probability, experimental results.

[1] University of Debrecen, Egyetem tér 1, 4032, Debrecen, Hungary
Correspondence: kovacs.sandor1999@gmail.com

[2] Institute for Nuclear Research (ATOMKI), Bem tér 18/c, 4026, Debrecen, Hungary.

Introduction

The wide range of isotopes observed in the Universe is the result of a few key nucleosynthesis processes. According to our current understanding, only the lightest isotopes (^{1,2}H, ^{3,4}He, and ^{7}Li) originated from the Big Bang. The bulk of the elements up to iron (Fe) is synthesized in stars via stellar burning. In AGB stars, in massive stars during the stellar burning phase, and in the explosive end-phases of massive stars, even heavier isotopes are produced mainly by free neutron capture (s-process, r-process) and to a small extent by the p-process (Burbidge et al., 1957).

The slow neutron capture process (so-called s-process) operates close to the valley of stability where the typical time between two consecutive neutron captures is longer than the lifetime of the produced isotope ($\lambda_{n\gamma} << \lambda_{\beta}$). The endpoint of this process is the ^{209}Bi isotope (Käppeler et al., 2011). Therefore, there must be an additional process, creating heavier elements than Bi (U, Th). This, so-called r-process, which takes place on a timescale of seconds, can only occur in an environment with a very high neutron density. A summary of the conditions and corresponding possible astrophysical environments required for the r-process to be successful is given in (Cowan et al., 2021). By the parallel detection of gravitational waves (GW170817 event) and optical counterparts, in 2017 for the first time, it was proved that r-process isotopes can be formed during the merge of neutron stars (Abbott et al., 2017). Furthermore, theoretical modelling suggested that collapsars could also be the site of the r-process which is supported by observing the abundance of old galactic halo stars (Reichert et al., 2020). Abundance calculations using precise nuclear physics inputs may provide additional constraints on the details of the nucleosynthesis processes.

The abundance distribution of the r-process is characterized by two main maximums, located at A~130 and A~195, the formation of these peaks is associated with a more stable structure of the relevant isotopes due to the closed neutron shell. However, in between the two peaks,

there is a third, smaller maximum (at A~160), called the rare-earth abundance peak, which forms during the freeze-out period (when the material starts to decay back to stability) of the r-process. Accordingly, understanding the synthesis of the lanthanides may allow the probe of the freeze-out conditions. The formation of the REP is sensitive to variables that control the neutron density and neutron-to-seed ratio in the late stages of the r-process. The detailed modelling of the REP formation (Mumpower et al., 2012b) showed that it is possible to constrain the range of astrophysical conditions of a potential site, but at first, the uncertainty of the nuclear physics inputs must be reduced.

For this reason, the β-decay properties of 28 isotopes of Pm, Sm, Eu, and Gd were measured (Kiss et al., 2022). Most importantly, the β-delayed one-neutron-emission probabilities (P_{1n} values) have been measured for the first time and the β-decay half-life ($T_{1/2}$) database was significantly improved and extended toward more neutron-rich species. In the following, we will show the main steps of the analysis using the ^{162}Pm isotope as an example.

Experimental approach

The experiment was performed in RIKEN Nishina Center, located at Wako-shi, Japan. The ^{238}U primary beam is accelerated in several steps up to 345 MeV/nucleon and then bombarded into a 5 mm thick ^{9}Be target with an intensity of about 60 pnA. Identification of isotopes with varying proton/neutron ratios is performed using the BigRIPS separator, where energy loss (ΔE), magnetic rigidity (Bρ) and time-of-flight (ToF) measurements are performed at various focal points of the beamline (Fukuda et al., 2013).

A schematic sketch of the AIDA-BRIKEN detector setup is in Figure 1 of (Tolosa-Delgado et al., 2019), whose main components summarize below. After the aluminum degrader (to adjust the kinetic energy) at focal point F11, the radioactive isotopes were implanted in the Advanced Implantation Detector Array (AIDA) which consists of

six double-sided silicon strip detectors (DSSSD). In addition, the set-up contained a 10 mm thick plastic scintillation detector behind the DSSSD stack to veto passing low-mass particles (Griffin et al., 2015). To detect the neutron and gamma events from decay, AIDA is placed in the center of the BRIKEN neutron counter containing 140 ^{3}He-filled proportional counters embedded in a polyethylene matrix that acts as a neutron energy moderator. The slowed neutrons are detected by the ^{3}He(n,p)^{3}H reaction. The neutron detection efficiency of the system was determined by simulation and by experimental measurements with a ^{252}Cf neutron source (Pallas et al., 2022). Since the β-delayed neutron emitters have moderate $Q_{\beta n}$-values (< 6 MeV) in our experiments, in the analysis the nominal average neutron detection efficiency ($\overline{\varepsilon}_n$ = 66.8 ± 2,0%) determined in (Tolosa-Delgado et al., 2019) was used. Furthermore, two CLOVER-type HPGe detectors were inserted into the polyethylene matrix horizontally from opposite sides for γ spectroscopy.

After the identification of the fragments with the BigRIPS separator, the AIDA-BRIKEN detector system is used to detect implantation events, subsequent decays, and associated neutrons as well as γ-photons.

Analysis and results

The implantation-β histograms (i-β) show the number of correlated β-events as a function of the detection time from implantation (panel A of Fig. 1). The half-lives of the daughter and even granddaughter nuclei in this nuclear range are so short that the β-decay events from them are not negligible. Thus, the i-β histograms include not only the events from the β-decay of the implanted parent isotope but also the events from the decay of subsequent members of the decay chain. Hence the half-lives were obtained by binned maximum likelihood fitting of the time distributions of the i-β correlations using the sum of Bateman's equations, taking into account the activity of the mother, daughter, granddaughter, and great-granddaughter (where applicable) nuclei

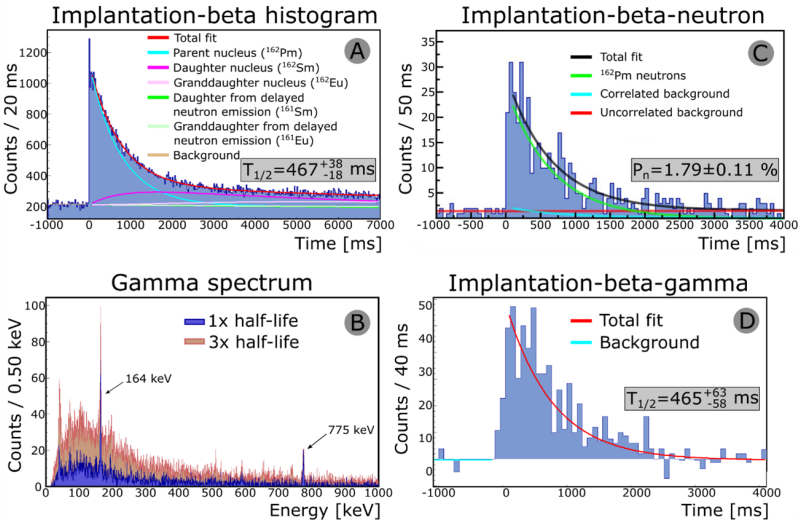

Figure 1.: The β-decay of 162Pm. Panel A shows the Bateman fit of the i-β histogram with contributions from later members of the decay series. Panel B shows the fit of the i-β-n histogram with an exponential function. Panel C shows the low energy part of the γ-spectrum measured by the HPGe detectors. Blue indicates the spectrum detected during one half-life and brown indicates the spectrum detected during three half-lives so that gamma events associated with the parent nucleus can be identified. The i-β-γ histogram for the 162 keV γ-peak, shown in panel D, was fitted by an exponential function to derive the half-life. See the text for details.

and the β-delayed neutron branch of the decay chain. In our case the Bateman equation can be written as:

$$N_k(t) = N_{10} \prod_{i=1}^{k-1} (\lambda_i b_{i,i+1}) \times \left(\sum_{i=1}^{k} \frac{e^{-\lambda_i t}}{\prod_{j=1 \neq 1}^{k} (\lambda_j - \lambda_i)} \right)$$

where $N_{k(t)}$ is the number of -type nuclei at any given t time, N_{10} is the initial (t = 0) number of implanted parent nuclei, $\lambda = \ln 2/T_{1/2}$ is the decay constant, and $b_{i,i+1}$ is the branching ratio from nucleus i to i +1 nucleus. The branching ratios determine the decay path, so to account for the delayed neutron emission branch, the branching ratio is set to be the delayed neutron emission probability (P_n). With the branching ratios isomer states can also be considered. Thus, knowing the half-lives

of the subsequent decay series members, the number of implantations, and the P_n values, the decay constant of the parent nucleus can be determined. Random β-decay events were derived from the backward time distributions. For more details on the analysis method see (Tolosa-Delgado et al., 2019).

β-delayed neutron emission occurs when the decay of a neutron-rich isotope leads to a level in the daughter above the neutron separation energy (S_n) and thus the decay can be followed by the emission of neutron(s). The phenomenon is characterized by the emission probability, known as the P_n value.

To derive the P_n values, the number of the neutron-gated β-decay events was derived by fitting an exponential function to the background subtracted time distribution of implant-β-neutron (i-β-n) correlations. The studied isotopes can be divided into three groups from the evaluation point of view. In the case of the lightest isotopes where $Q_{\beta n}$-values are small or even negative (so this decay channel is closed) the number of implantation-beta-neutron (i-β-n) events were derived by numerical integration and the P_n values were found to be consistent with zero. Similarly, only a conservative upper limit for the P_{1n} value was determined, and numerical integration was applied for the most neutron-rich isotopes with less than 50 neutron events. Furthermore, in numerous cases there were sufficient statistics to fit the i-β-n histogram with exponential functions to determine the number of i-β-n correlation events (panel B of Fig. 1). Since the half-life determination is influenced by the P_n value (it is the branching ratio in the Bateman equation) and vice versa, the fitting procedure described above was performed using an iterative approach.

An independent method to derive the half-life values and to validate the results based on the Bateman fits is to measure the time evolution of yield of the γ-ray transitions emitted during the decay of the implanted isotope. However, to use this approach at first the γ-transitions associated with the decay must be identified. This was done by examining the time evolution of the gamma spectrum (1 half-life and 3 half-lives

shown in panel C) and the time distribution of the implantation-beta-gamma (i-β-γ) correlation events was fitted by the combination of an exponential function and a linear background (panel D).

Using the above methods, the following results were obtained for the ^{162}Pm isotope: $T_{1/2} = 467\ ^{+38}_{-18}$ ms from i-β fitting (Kiss et al., 2022), which is in good agreement with the $T_{1/2} = 465\ ^{+63}_{-58}$ ms preliminary result found from the i-β-γ method. The half-life of this isotope has been measured previously: $T_{1/2}$ = 630 + 180 ms (Wu et al., 2017). Our result agrees with the literature data, but its uncertainty is significantly lower and thus already suitable for use in astrophysical calculations. The P_{1n}-value was determined experimentally for the first time for this isotope and was found to be 1,79 ± 0,11 % by exponential fitting (Kiss et al., 2022).

Outlook

The high-precision experimental data was used in nuclear reaction network calculations for the r-process employing a neutron-star merger and a hot wind scenario. To identify the nuclear physics inputs of importance within the current experimental uncertainties, a new variance-based sensitivity analysis method was used (Kiss et al., 2022). The results of the analysis indicate that only a handful of variables account for nearly all the uncertainty (variance) of the abundance pattern. To better constrain these uncertainties further measurements are needed and thus experimental proposals were submitted to the Program Advisory Committee at RIKEN.

Acknowledgments

This work was supported by NKFIH (NN128072) and by the ÚNKP-22-2 and ÚNKP-22-3 New National Excellence Program of the Ministry for Culture and Innovation from the source of the National Research, Development and Innovation Fund (Project numbers: ÚNKP-22-2-I-DE-75; ÚNKP-22-3-II-DE-132).

References

Abbott, B.P. et al., 2017. Multi-messenger Observations of a Binary Neutron Star Merger', The Astrophysical Journal, 848(2), p. L12. Available at: https://doi.org/10.3847/2041-8213/aa91c9.

Burbidge, E.M. et al., (1957. Synthesis of the Elements in Stars, Reviews of Modern Physics, 29(4), pp. 547-650. Available at: https://doi.org/10.1103/RevModPhys.29.547.

Cowan, J.J. et al., 2021. Origin of the heaviest elements: The rapid neutron-capture process, Reviews of Modern Physics, 93(1), p. 015002. Available at: https://doi.org/10.1103/RevModPhys.93.015002.

Fukuda, N. et al., 2013. Identification and separation of radioactive isotope beams by the BigRIPS separator at the RIKEN RI Beam Factory, Nuclear Instruments and Methods in Physics Research Section B: Beam Interactions with Materials and Atoms, 317, pp. 323-332. Available at: https://doi.org/10.1016/j.nimb.2013.08.048.

Griffin, C. et al., 2015. Beta- decay studies of R-process nuclei using the advanced implantation detector array, in Proceedings of XIII Nuclei in the Cosmos - PoS(NIC XIII). XIII Nuclei in the Cosmos, Debrecen, Hungary: Sissa Medialab, p. 097. Available at: https://doi.org/10.22323/1.204.0097.

Käppeler, F. et al. 2011. The s process: Nuclear physics, stellar models, and observations, Reviews of Modern Physics, 83(1), pp. 157-193. Available at: https://doi.org/10.1103/RevModPhys.83.157.

Kiss, G.G. et al. 2022. Measuring the β-decay Properties of Neutron-rich Exotic Pm, Sm, Eu, and Gd Isotopes to Constrain the Nucleosynthesis Yields in the Rare-earth Region, The Astrophysical Journal, 936(2), p. 107. Available at: https://doi.org/10.3847/1538-4357/ac80fc.

Mumpower, M.R., McLaughlin, G.C. and Surman, R. 2012. The rare Earth peak: an overlooked r-process diagonostic, The Astrophysical Journal, 752(2), p. 117. Available at: https://doi.org/10.1088/0004-637X/752/2/117.

Pallas, M. et al. 2022. Efficiency calibration of the BRIKEN detector: the world largest counter for beta-delayed neutrons. Available at: https://doi.org/10.48550/ARXIV.2204.13379.

Reichert, M. et al. 2020. Neutron-capture elements in dwarf galaxies: III. A homogenized analysis of 13 dwarf spheroidal and ultra-faint galaxies, Astronomy & Astrophysics, 641, p. A127. Available at: https://doi.org/10.1051/0004-6361/201936930.

Tolosa-Delgado, A. et al. 2019. Commissioning of the BRIKEN detector for the measurement of very exotic β -delayed neutron emitters, Nuclear Instruments and Methods in Physics Research Section A: Accelerators, Spectrometers, Detectors and Associated Equipment, 925, pp. 133-147. Available at: https://doi.org/10.1016/j.nima.2019.02.004.

Wu, J. et al. 2017. 94 β -Decay Half-Lives of Neutron-Rich Cs 55 to Ho 67 : Experimental Feedback and Evaluation of the r -Process Rare-Earth Peak Formation, Physical Review Letters, 118(7), p. 072701. Available at: https://doi.org/10.1103/PhysRevLett.118.072701.

Cosmology from the weak lensing of gravitational waves

Charlie Mpetha[1], Giuseppe Congedo[1], Andy Taylor[1]

Abstract

Planned and proposed future gravitational wave detectors will observe huge numbers of binary mergers. It is timely to explore cosmological tests that can be performed with this upcoming plethora of data. We forecast a combined standard siren + weak lensing analysis, where perturbations in the propagation of gravitational waves by intervening matter allows their use to probe large scale structure. We find that 3rd generation detectors, combining sources with and without an electromagnetic counterpart, could outperform future galaxy/intensity mapping surveys in constraining dark energy using this joint analysis method. We also demonstrate for the first time how merging binaries could constrain the sum of neutrino masses independently from other probes, should DeciHz detectors be launched.

Key Words

Astrophysics, Cosmology, Gravitational waves, Gravitational wave detectors, Dark matter, Dark energy, Large scale structure of the universe, Neutrino mass.

[1] Institute for Astronomy, School of Physics and Astronomy, University of Edinburgh, Royal Observatory, Blackford Hill, Edinburgh, EH9 3HJ, United Kingdom Correspondence: c.mpetha@ed.ac.uk

Introduction

In Schutz (1986) the author investigates how Gravitational Waves (GWs) from Binary Neutron Star (BNS) mergers could be used to infer the value of the expansion rate H_0. The first detection of GWs in 2015 (The LIGO Scientific collaboration et al. 2016) led to an increased effort in exploring their use for cosmology. The multimessenger BNS merger event GW170817, where an electromagnetic (EM) transient counterpart was observed along with the GW, allowed this single event to give a constraint of $H_0 = 70.0^{+12.0}_{-8.0}$ kms−1 Mpc−1 (The LIGO Scientific Collaboration and The Virgo Collaboration et al., 2017). This is the Standard Siren measurement, using the relationship between the wave amplitude and the distance to the source, and a redshift obtained through the EM counterpart, to probe cosmology. Independent measurements of H_0 are important due to the apparent tension between late and early universe measurements (Wong et al., 2019; Aghanim et al., 2020; Brout et al., 2022). As the Advanced LIGO-Virgo-Kagra (LVK) network will observe enough sources to inform on this tension in the near future (Chen et al., 2018), it is important to explore the other uses of GWs for cosmology, beyond a standard siren measurement of H_0. This is especially the case when considering the powerful detectors planned for the future, including the space-based LISA (The eLISA Consortium et al., 2013), and 3rd generation (3G) ground based detectors Cosmic Explorer (Reitze et al., 2019) and the Einstein Telescope (Maggiore et al., 2020). From 3G detectors we can expect $O(10^5 - 10^7)$ sources observed by the end of the 2040's, and comparable numbers with much improved sky localisation in the second half of the century should space-based DeciHz detectors such as DECIGO (Kawamura et al., 2020) and the Big Bang Observer (Harry et al., 2006) be launched.

In this work we investigate how the weak lensing of gravitational waves, combined with the standard siren measurement, can be a powerful probe of both geometry and large scale structure. Using the weak lensing of GWs (GW-WL) as a cosmological probe was first speculat-

ed in Cutler & Holz (2009) and developed in Camera & Nishizawa (2013). Forecasting a joint analysis of GWs, using both the standard siren measurement and GW- WL, was performed in Congedo & Taylor (2019) (henceforth CT19). The authors demonstrated how combining these two measurements breaks key degeneracies. Similar work was performed in Balaudo et al. (2022) where the authors look at the weak-lensing signal alone, in the context of cross-correlations with other probes to constrain modified gravity. Here we build upon the work of CT19 and provide a short review of the main results of Mpetha et al. (2022), using a range of assumptions on source properties and extending the analysis to varying models of dark energy and neutrino mass - parameters presently of interest. Tomographic weak lensing is used to exploit all available cosmological information. We also include sources without an associated EM counterpart, which will comprise the bulk of future GW detections.

Gravitational wave cosmology

Standard Sirens

An observed gravitational wave is the linear combination of the two polarisations h_+ and $h_\times$, combined with their respective antenna patterns F_+ and $F_\times$ which describe the detector response to a passing gravitational wave, $h = F_+ h_+ + F_\times h_\times$, in the long-wavelength regime. Here both h_+ and $h_\times$ are $\propto 1/d_L$. The wave amplitude informs on the luminosity distance dL, though there is degeneracy with the inclination angle. This luminosity distance depends on the expansion rate $H(z)$

$$d_L(z) = (1+z)\int_0^z \frac{c\,dz'}{H(z')},$$

where

$$\left(\frac{H(z)}{H_0}\right)^2 = \Omega_{\rm m}(1+z)^3 + \Omega_{\rm DE}(1+z)^{3(1+w_0+w_a)} e^{\frac{-3w_a z}{1+z}}.$$

H_0 is the present universe expansion rate, Ω_m and Ω_{DE} are the matter and dark energy density parameters at present, while we assume the widely used CPL parameterisation (Chevallier & Polarski, 2001; Linder, 2003) of a time-varying dark energy equation of state (EoS) $w_{DE} = w_0 + waz/(1+z)$. w_0 is the dark energy EoS today, and wa is its growth rate with the scale factor a. Ω_m contains the baryonic, cold dark matter and neutrino density components, $\Omega_m = \Omega b + \Omega_{CDM} + \Omega \nu$. In ΛCDM most of the matter in the universe is Cold Dark Matter (CDM), dark energy is a cosmological constant Λ ($\Omega_{DE} = \Omega_\Lambda$) with a constant EoS of $w_\Lambda = -1$ ($w_0 = -1$ and wa = 0). In these proceedings we assume zero curvature, but in Mpetha et al. (2022) we extend to models including curvature. To probe the cosmological parameters above, as well as measuring dL, a source redshift is required - hence the huge benefit of a multimessenger approach to observing gravitational waves. For the vast majority of sources the redshift can not be derived from the gravitational wave alone due to the mass-redshift degeneracy (Schutz, 1986). If an EM counterpart is observed, either from detecting a coincident transient or localising to a host galaxy, the source is a Bright Standard Siren (BSS). This can be a binary neutron star, supermassive black hole binary, and in some cases a black hole neutron star binary (Fragione, 2021). If no EM counterpart is observed, it is a Dark Standard Siren (DSS). This will be mostly binary black holes, and there are several methods of inferring a redshift in this case (Schutz, 1986; MacLeod & Hogan, 2008; Messenger et al., 2014; Mukherjee & Wandelt, 2018; Farr et al., 2019; Mukherjee et al., 2020; You et al., 2021; Ye & Fishbach, 2021; Ezquiaga & Holz, 2022).

Weak lensing of gravitational waves

As gravitational waves travel through the universe from a distant emitting source to our detector, they are weakly lensed by the gravitational potential of the intervening large-scale structure. The magnification effect on both electromagnetic (Bartelmann & Schneider, 2001; Schneider, 2003) and gravitational (Takahashi et al., 2005) radiation in the

geometric optics regime is given by

$$\mu \approx 1+2\kappa,$$

where kappa is the lensing convergence, a weighted projection of density perturbations along the line-of-sight. In the weak lensing regime, the observed, lensed luminosity distance dL^{obs} is given by

$$d_L^{obs} = \frac{1}{\sqrt{\mu}} d_L^{true} \cong (1-\kappa) d_L^{true}$$

so a matter overdensity increases the wave amplitude, leading to a smaller inferred distance.

The weak lensing of each source is a source of statistical noise on the distance measurement of ~1–5%. A noisy estimate of the convergence field at the location in the sky where the source originated from can be found from its deviation from the best fit $d_L(z)$. We can bin these κ estimates into tomographic redshift bins (denoted by i and j), then perform a two-point correlation function of the Fourier transformed convergence field in each bin to find the convergence power spectrum,

$$C_{(ij)}^{\kappa\kappa}(\ell) = \int_0^{z_{max}} \frac{c(1+z)^2}{H(z)} W_{(i)}(z) W_{(j)}(z) P_\delta \left(k = \frac{\ell+\frac{1}{2}}{r}, z \right) dz,$$

where

$$W_{(i)}(z) = \frac{3}{2}\Omega_{m,0} \left(\frac{H_0}{c}\right)^2 \int_{z_i}^{z_i+1} p(z') \frac{r'-r}{r'} dz'.$$

is the Window function, containing the normalised observed source distribution $p(z)$ and the effect of the lens on this source due to their separation. r is the comoving distance. The Limber approximation for k-modes, $k = (\ell + 1/2)/r$, is shown in the matter power spectrum, and is used for large values of the multipole ℓ. A common parameter to normalise the matter power spectrum, $P_\delta(k,z)$, is the linear normalisation of its amplitude in spheres of $8h^{-1}$ Mpc, σ_8 (Peebles, 1980).

Results

The standard siren measurement and corresponding weak lensing analysis of GWs are combined for a joint analysis, the Bayesian framework of which is outlined in CT19. We find the Cramér-Rao lower bound on physical parameters using a Fisher matrix formalism. These physical parameter uncertainties are then mapped to observable parameter uncertainties using Monte Carlo methods, ensuring we capture the non-linear relationship between some parameters. We use Class to compute σ_8 values and auto- and cross- convergence power spectra for six redshift bins. We assume DSS are observed up to redshift 3.5, and their redshift is determined by a statistical average of galaxies in the line of sight. This leads to photometric-like redshift uncertainty at low-z which rapidly dilutes as we go to higher redshifts with fewer galaxy and GW sources. BSS have spectroscopic like redshifts, observed up to redshift 2 due to limits of GW detector sensitivity and spectroscopic redshift limits. Other sources of uncertainty considered are peculiar velocities, weak lensing, and GW detector instrumental uncertainty.

Fig. 1a shows forecasts for 3G gravitational wave detectors, using expected numbers of BSS and DSS (Reitze et al., 2019; Maggiore et al., 2020; Yu et al., 2021). We see how combining the two breaks parameter degeneracies, most notably in the Ω_m-S_8 plane where $S_8 = \sqrt{(\Omega_m/0.3)}$. This is because DSS events can be observed up to a higher redshift. The constraints on dark energy are better than forecasts for Euclid (Euclid Collaboration et al. 2020) and future intensity mapping surveys (Karkare et al. 2022).

Fig. 1b shows forecast for DeciHz detectors,and is the first demonstration of how gravitational waves can be used to independently constrain the sum of neutrino masses. In the best case we see a 1σ preference for the normal neutrino mass hierarchy (NH). While these constraints are not competitive with future CMB and intensity mapping experiments, GWs are a very clean signal and so could be a valuable source of extra information.

Conclusions

We find GW weak lensing tomography is set to be a valuable cosmological tool for 3G detectors. Bright Standard Sirens found from multimessenger gravitational wave and electromagnetic observations could constrain the dark energy equation of state parameters w_0 and wa with comparable precision to Euclid, depending on the number of sources and their uncertainty. In the case where we combine a population of BSS with realistic numbers of Dark Standard Sirens coming from binary black hole mergers, constraints on w_0 and wa improve upon Euclid, and give comparable or better constraints to forecasts for a CMB-S4-like experiment with 10^9 spectrometer hours (Karkare et al., 2022), and a 1024 dish HIRAX experiment which expects a precision ~ few percent (Karagiannis et al., 2022). Therefore it is vital the tools necessary for statistical inference of DSS redshifts are developed.

For space-based DeciHz GW detectors, many more BSS observations are expected due to the incredible sky localisation of these detectors, including DECIGO and the Big Bang Observatory. There will be exquisite precision on geometry parameters due to very large number of d_L – z data points with small d_L errors. These detectors could achieve a 1σ preference for the neutrino normal mass hierarchy. While not significant enough as a single probe to determine the neutrino mass hierarchy, these results demonstrate for the first time how the weak lensing of GWs could provide valuable extra information on the sum of neutrino masses when combined with future CMB experiments (Aiola et al., 2022) and HI intensity mapping surveys (Ferraro et al., 2022). For these results to be possible, the substantial challenge to overcome is building and deploying the space-based DeciHz GW detectors into their heliocentric orbits. Another recently explored possibility is a Lunar-based DeciHz GW detector, which would be easier to maintain and have comparable sensitivity to the proposed space-based DeciHz detectors (Jani & Loeb, 2021).

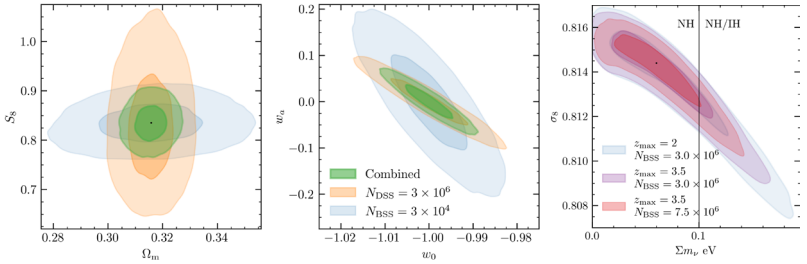

(a) (b)

Figure 1: Forecasts for combined gravitational wave weak lensing+standard siren constraints on cosmological parameters. a) shows expected constraints for 3G detectors in the wCDM cosmological model from Bright and Dark Standard Sirens (BSS/DSS) plus their combination, while b) shows constraints in the νΛCDM cosmological model from BSS observed by DeciHz detectors.

A limitation of this study is using single values for uncertainties for the whole population of GW sources. A natural extension to this work is to produce a realistic set of GW measurements through a Fisher forecast of their parameter uncertainties, then perform the d_L –z and power spectrum fitting on this realistic set of measurements.

References

Aghanim, N., et al., 2020. Planck 2018 results, Astronomy & Astrophysics, 641, A6.

Aiola, S., et al., 2022. Snowmass2021 CMB-HD White Paper (arXiv:2203.05728).

Balaudo, A., Garoffolo, A., Martinelli, M., Mukherjee, S., Silvestri, A., 2022. Prospects of testing late-time cosmology with weak lensing of gravitational waves and galaxy surveys (arXiv:2210.06398).

Bartelmann, M., Schneider, P., 2001.Weak gravitational lensing, Physics Reports, 340, 291.

Brout, D., et al., 2022. The Pantheon+ Analysis: Cosmological Constraints (arXiv:2202.04077).

Camera, S., Nishizawa, A., 2013. Beyond Concordance Cosmology with Magnification of Gravitational-Wave Standard Sirens, Physical Review Letters, 110, 151103.

Chen, H.-Y., Fishbach, M., Holz, D.E., 2018. A two per cent Hubble constant measurement from standard sirens within five years, Nature, 562, 545-547.

Chevallier, M., Polarski, D., 2001. Accelerating Universes with Scaling Dark Matter, International Journal of Mod- ern Physics D, 10, 213-223.

Congedo, G., Taylor, A., 2019. Joint cosmological inference of standard sirens and gravitational wave weak lensing, Physical Review D, 99, 083526.

Cutler, C., Holz, D.E., 2009. Ultrahigh precision cosmology from gravitational waves, Physical Review D, 80, 104009.

Euclid Collaboration et al., 2020. Euclid preparation, Astronomy & Astrophysics, 642, A191.

Ezquiaga, J.M., Holz ,D.E., 2022. Spectral sirens: cosmology from the full mass distribution of compact binaries (arXiv:2202.08240).

Farr. W.M., Fishbach, M., Ye, J., Holz, D.E., 2019. A Future Percent-level Measurement of the Hubble Expansion at Redshift 0.8 with Advanced LIGO, The Astrophysical Journal, 883, L42.

Ferraro, S., Sailer, N., Slosar, A., White, M., 2022. Snowmass2021 Cosmic Frontier White Paper: Cosmology and Fundamental Physics from the three-dimensional Large Scale Structure (arXiv:2203.07506).

Fragione, G., 2021. Black-hole–Neutron-star Mergers Are Unlikely Multimessenger Sources, The Astrophysical Journal Letters, 923, L2.

Harry, G.M., Fritschel, P., Shaddock, D.A., Folkner, W., Phinney, E.S., 2006. Laser interferometry for the big bang observer, Class. Quant. Grav., 23, 4887.

Jani, K., Loeb, A., 2021. Gravitational-wave Lunar Observatory for Cosmology, Journal of Cosmology and Astroparticle Physics, 2021, 044.

Karagiannis, D., Maartens, R., Randrianjanahary, L., 2022. Cosmological constraints from the power spectrum and bispectrum of 21cm intensity maps (arXiv:2206.07747).

Karkare, K.S., Dizgah, A.M., Keating, G.K., Breysse, P., Chung, D.T., 2022. Snowmass 2021 Cosmic Frontier White Paper: Cosmology with Millimeter-Wave Line Intensity Mapping (arXiv:2203.07258).

Kawamura, S., et al., 2020. Current status of space gravitational wave antenna DECIGO and B-DECIGO (arXiv:2006.13545).

Linder, E.V., 2003. Exploring the Expansion History of the Universe, Phys. Rev. Lett., 90, 091301.

MacLeod, C.L., Hogan, C.J., 2008. Precision of Hubble constant derived using black hole binary absolute distances and statistical redshift information, Phys. Rev. D, 77, 043512.

Maggiore, M., et al., 2020. Science case for the Einstein telescope, Journal of Cosmology and Astroparticle Physics, 2020, 050-050.

Messenger, C., Takami, K., Gossan, S., Rezzolla, L., Sathyaprakash, B.S., 2014. Source Redshifts from Gravitational-Wave Observations of Binary Neutron Star Mergers, Physical Review X, 4, 041004.

Mpetha, C.T., Congedo, G., Taylor, A., 2022. Future prospects on testing extensions to ΛCDM through the weak lensing of gravitational waves (arXiv:2208.05959).

Mukherjee, S., Wandelt, B.D., 2018. Beyond the classical distance-redshift test: cross-correlating redshift-free standard candles and sirens with redshift surveys (arXiv:1808.06615).

Mukherjee, S., Wandelt, B.D., Silk J., 2020. Probing the theory of gravity with gravitational lensing of gravitational waves and galaxy surveys, Monthly Notices of the Royal Astronomical Society, 494, 1956-1970.

Peebles, P.J.E., 1980. The large-scale structure of the universe. Princeton University Press.

Reitze, D., et al., 2019. Cosmic Explorer: The U.S. Contribution to Gravitational-Wave Astronomy beyond LIGO (arXiv:1907.04833).

Schneider, P., 2003. Gravitational lensing as a probe of structure (arXiv:astro-ph/0306465).

Schutz, B.F., 1986. Determining the Hubble constant from gravitational wave observations, Nature, 323, 310.

Takahashi, R., Suyama, T., Michikoshi, S., 2005. Scattering of gravitational waves by the weak gravitational fields of lens objects, Astronomy & Astrophysics, 438, L5-L8.

The LIGO Scientific Collaboration and The Virgo Collaboration et al., 2017. A gravitational-wave standard siren measurement of the Hubble constant, Nature, 551, 85-88.

The LIGO Scientific collaboration et al., 2016. Observation of Gravitational Waves from a Binary Black Hole Merger, Physical Review Letters, 116.

The eLISA Consortium et al., 2013. The Gravitational Universe (arXiv:1305.5720).

Wong, K.C. et al., 2019. H0LiCOW – XIII. A 2.4 per cent measurement of H0 from lensed quasars: 5.3σ tension between early- and late-Universe probes, Monthly Notices of the Royal Astronomical Society, 498, 1420-1439.

Ye, C., Fishbach, M., 2021. Cosmology with standard sirens at cosmic noon, Physical Review D, 104, 043507.

You, Z.-Q., Zhu, X.-J., Ashton, G., Thrane, E., Zhu, Z.-H., 2021. Standard-siren Cosmology Using Gravitational Waves from Binary Black Holes, The Astrophysical Journal, 908, 215.

Yu, J. et al., 2021. Multimessenger Detection Rates and Distributions of Binary Neutron Star Mergers and Their Cosmological Implications, The Astrophysical Journal, 916, 54.

Spectroscopic simulations for the Euclidmission

Francesca Passalacqua[1,2] on behalf of the Euclid Consortium

Abstract

Euclid is mission of the European Space Agency (ESA), designed to investigate the structure and the evolution of the Universe. To achieve the required accuracy on the redshift measure, calibrations must be performed both on the ground and in-flight. After launch, dust pitting, radiation damage, and material outgassing will degrade the transmission of light trough the instruments over time: an in-flight calibration procedure has been developed to determine and monitor the responses. Realistic simulations of different systematic effects are needed to validate and optimize the in-flight self-calibration procedure. We present the framework to study the in-flight self-calibration in the spectroscopic channel. The procedure includes the simulations of the entire calibration survey, the extraction of the spectra of the sources, and the reconstruction of the response function with a χ^2 minimization.

Key Words

in-flight calibration, pixel simulation, near-infrared spectrometer, systematic effects, relative response function.

[1] Dipartimento di Fisica e Astronomia "G. Galilei", Università degli Studi di Padova, Via Marzolo 8, I-35131, Padova, Italy. Correspondence: francesca.passalacqua@pd.infn.it

[2] INFN-Padova, Via Marzolo 8, I-35132, Padova, Italy.

Introduction

Euclid is a mission of the European Space Agency (ESA), scheduled to be launched in 2023, designed to investigate the nature and evolution of dark energy and dark matter. Euclid will observe the extragalactic sky from the Lagrangian point L2 for six years: the survey will cover an area of about 15 000 deg^2 up to redshift ~ 2.

In order to constrain the cosmological parameters, two main probes will be used: Weak Lensing (WL) and Galaxy Clustering (GC) (Laureijs et al., 2011). WL will be measured by using the shapes and the photometric redshift of ~ 1,5 billion galaxies; GC will be measured by using the spectroscopic redshift of ~ 35 million galaxies. To carry out these measurements, Euclid mounts two instruments onboard: a visible imager (VIS) and a Near-Infrared Spectrometer and Photometer (NISP). VIS performs imaging with high resolution and it will provide the shapes of the galaxies. NISP will measure the redshift of the sources observed by VIS with an accuracy of $0.02(1 + z)$ and $0.001(1 + z)$ in the photometric and spectroscopic channel respectively (Laureijs et al., 2011; Euclid Collaboration: Schirmer et al., 2022).

After launch, dust pitting, radiation damage, and material outgassing will degrade the response of the instruments, leading to an attenuation of the measured flux (Euclid Collaboration: Schirmer et al., 2022). Thus, to determine and monitor the evolution of the response of the instrument with great accuracy, an in-flight self-calibration program has been designed.

Realistic simulations allow the validation and optimization of the self-calibration procedure. We focus on the simulations of the self-calibration procedure for the spectroscopic channel of the NISP instrument: we simulate several systematic effects, extract the spectra of the sources, and finally reconstruct the response function of NISP spectroscopic channel.

The Self-Calibration

To monitor the response of the instruments over time, Euclid will observe each month the same sky area, called Self-Calibration Field. This area consists in a ~ 3.2 deg^2 circular field, located near the North Ecliptic Pole, which provides both a sufficient number of stars and a low background level from the Galactic disk.

The self-calibration strategy exploits the multiple observations of the same astrophysical sources in different positions on the focal plane. Because of the distortions of the signal introduced by the instrument, the same object observed at different positions on the focal plane provides different count rates. The relative response of the instrument, i.e. the response up to a multiplicative global scale factor, can be inferred by the requirement that each source is reconstructed with statistically consistent count rates, within the whole focal plane (Davini et al., 2021).

In the scientific survey, each observation will be made up of four frames acquired with a dithering strategy, in order to compensate for gaps between detectors, to discriminate cosmic ray hits, and to disentangle the spectra overlapping. The Euclid Self-Calibration survey will be made up of 60 pointings covering the entire self-calibration field, which are shown in Figure 1.a. In order to provide a complete and reliable reconstruction of the response of the instrument over the entire focal plane, it is crucial to use an optimized pointing sequence to ensure that every spatial scale of interest is sampled during the calibration. The 60 pointings were obtained with a Monte Carlo approach and properly sample all the spatial scales that will be observed in the survey: from a minimum dither scale (10") to the Field of View size (0.7 deg^2) (Risso et al., in prep.).

Simulations Configuration

It is necessary to consider the effect of different systematics to study and test the self-calibration procedure. For this purpose, we simulate

the images acquired by NISP detectors with the Euclid official spectroscopic simulator. The simulator takes as input the instrumental features (readout noise, bad pixels, non-linearity) and the environmental (background light level and cosmic ray hits) configuration.

Cross-contamination, i.e. the overlapping of the signal form different sources is shown in Figure 1.b and it strongly affects the spectra reconstruction. We consider this systematic effect in the simulations by using a catalog of sources containing the number of sources that are expected to be observed by Euclid Self-Calibration Field, based on both theoretical models and observations.

Since the instrumental response will not be known and will vary over time, it is necessary to simulate and reconstruct several functions to validate the method used. The response function is given by the combination of large-scale and small-scale effects. At large scales the optics introduce an attenuation of the signal at the edge of the focal plane, while dust and ice structures cause variation at small scales. So far, we have been simulating a uniform response and a Gaussian profile with the peak located at the center of the focal plane.

Reconstruction of the Response Function

The method we adopt for the reconstruction of the response (Davini et al., 2021) requires the measurement of the position and the signal of the sources on the focal plane. In photometry these two quantities are clearly identified, while in spectroscopy they must be re-defined: we set the reconstruction for a specific wavelength and repeat the process at different values.

We use Euclid official code to extract the counts of the 1D un-calibrated spectra from the simulated images. The code performs a pre-processing on the raw images to correct NISP detector artefacts: bad pixels and cosmic rays' hits are identified; non-linearity and dark current are corrected. The 1D un-calibrated spectra are extracted after flat-fielding, background subtraction, and decontamination of overlapping spectra.

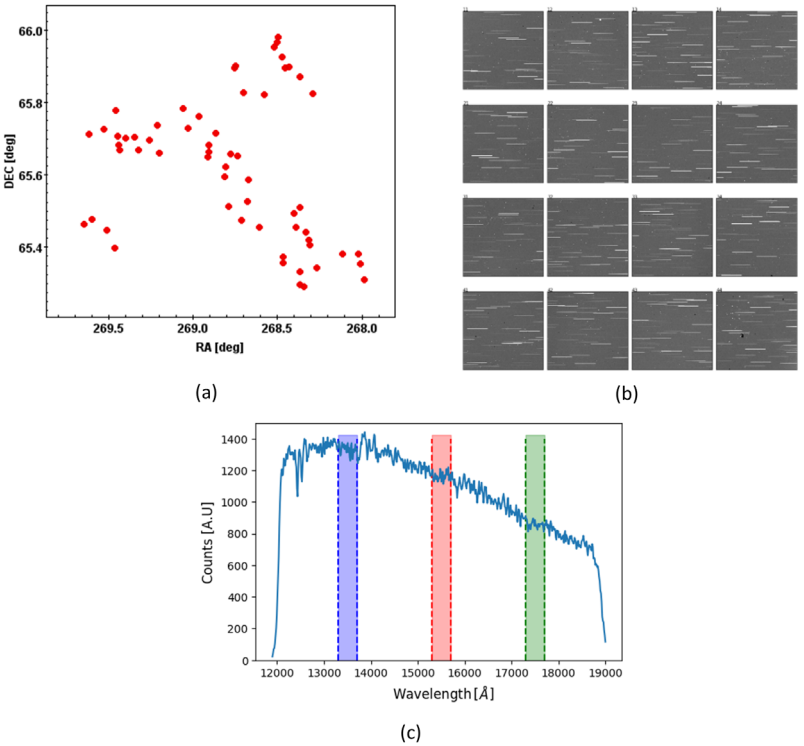

Figure 1. Simulation of the self-calibration procedure (Passalacqua, 2022).
a) shows the optimize sequence of pointings; b) shows the simulation of the images detected by NISP detectors; c) shows the extracted 1D counts from the raw images. The regions in different colors represent the integration range for each selected wavelength.

For each source we consider the position of a specific wavelength and we integrate the signal in a range of about ~ 400 Å in order to reduce the relative error on the measurement of the counts. Figure 1.c illustrates the extracted spectra (in A.U.) with three integration ranges represented in different colors.

We reconstruct the response function with a χ^2 minimization method (Davini et al., 2021) where the extracted counts from simulated data are compared to the expected ones, which are computed as the product of the theoretical rates, the exposure time, and the response

function. Since the theoretical rates are unknown, there is a global scale factor and the minimization returns the response of the instrument relative to a reference point of the focal plane.

Repeating the described procedure at different wavelength and interpolating the relative response functions will allow the correction of the spectra extracted during the scientific survey.

Conclusion

As a preliminary test, we simulated and reconstructed a uniform response function. So far, we are increasing the precision in the extraction of the counts in order to reconstruct non-uniform responses of the instrument.

After the validation is completed, we could study the optimization of the procedure by changing parameters such as the wavelength range of the signal integration.

Acknowledgements

The author acknowledge the Euclid Consortium, the European Space Agency, and a number of agencies and institutes that have supported the development of *Euclid*, in particular the Academy of Finland, the Agenzia Spaziale Italiana, the Belgian Science Policy, the Canadian Euclid Consortium, the Centre National d'Etudes Spatiales, the Deutsches Zentrum für Luft- und Raum- fahrt, the Danish Space Research Institute, the Fundação para a Ciência e a Tecnologia, the Ministerio de Economia y Com- petitividad, the National Aeronautics and Space Administration, the Netherlandse Onderzoekschool Voor Astronomie, the Nor- wegian Space Agency, the Romanian Space Agency, the State Secretariat for Education, Research and Innovation (SERI) at the Swiss Space Office (SSO), and the United Kingdom Space Agency. A complete and detailed list is available on the *Euclid* web site (http://www.euclid-ec.org). The autor would also thank the *Euclid* INFN group in Genoa for the contribution.

References

Davini, S. et al., 2021. A Proposal for Relative In-flight Flux Self-calibrations for Spectro-photometric Surveys. PASP, Volume 133, doi: 10.1088/1538-3873/ac102e.

Euclid Collaboration: Schirmer, M. et al., 2022. Euclid preparation. XVIII. The NISP photometric system. A&A, Volume 662 , doi: 10.1051/0004-6361/202142897.

Laureijs, R. et al., 2011. Euclid Definition Study Report. ArXiv, doi: 10.48550.

Passalacqua, F., 2022. Calibrations and Realistic Simulations for the NISP Instrument of the Euclid Mission. M.S. thesis, Università degli Studi di Genova, Genova.

Towards experimental study of compact binary ejecta opacity relevant for kilnovae

Angelo Pidatella[1] *on behalf of the PANDORA collaboration*

Abstract

Joint observations of gravitational-wave (GW) event to compact binary objects mergers, and of their electromagnetic counterpart, known as kilonova (KN) lead to a new avenue in the multi-messenger astronomy era to constrain the astrophysical origin of the r-process elements and the equation of state of dense nuclear matter. Coalescence of double neutron star releases n-rich ejecta which undergoes r-process nucleosynthesis, driving the quick evolution of the KN transient powered by freshly synthesized decaying radionuclides. KNe act as spectral probes to explore the merger environment, hence of fundamental relevance for future detection and for providing sounder nucleosynthetic yields. However, heterogeneous post-merging ejecta composition strongly impacts on the KN light-curve prediction through the ejecta opacity, which is yet hard to be fully captured via theoretical models. We present some peculiar features of the KN studies, focusing on the opacity issue, from the atomic and plasma physics perspectives. We report on the paradigm of blue-KN emission timescale peaked at optical wavelengths, presenting the work carried out in the framework of the PANDORA collaboration to support planned experimental measurements

[1] INFN-LNS, Via S. Sofia 62, 95123, Catania, Italy. Correspondence: pidatella@lns.infn.it

of opacity with in-laboratory plasmas close to the KN-stage conditions. In this view, we refer to results of experiments recently performed at the INFN-LNS on the Flexible Plasma Trap to reproduce suitable early-stage ejecta plasmas, presenting a possible conceptual design of a multi-diagnostic setup for the future opacity measurements.

Key Words

Plasma Physics, Nuclear Astrophysics, Multi-messenger Astronomy, Plasma Spectroscopy, Kilonovae.

Introduction

Recent detection of gravitational-wave (GW) events, such as GW170817 (Abbott, 2017), along with their radioactively powered thermal transients, known as *kilonovae* (KNe), represented first direct evidence of on-going rapid neutron capture nucleosynthesis process (*r*-process) hosted in the environment led by the coalescence of binary neutron stars (Li et al, 1998; Metzger et al., 2010; Korobkin et al., 2012). Studying the KNe light-curve timescale and dynamics could help in advancing knowledge on the post-merging ejecta dynamics, on the equation of state of nuclear dense matter, and on the *r*-process yield of elements heavier than iron. In particular, the observation (Arcavi, 2017) of the optical KNe spectrum (AT2017gfo) evinced a multi-component ejecta, made of both light- and heavy-*r* process elements (Kasen et al., 2017), which puts some constraints in modelling the photospheric phase of KNe synthetic light-curve from the dynamical ejecta: on the one hand on the nucleosynthesis calculations, fixing the heating rate, and on the other hand on radiation transport, which relies on the ejecta plasma opacity, the latter strongly dependent on the time-evolving composition. Spectral signatures of some *r*-process elements have been recently found (Watson et al., 2019), with other to be further investigated. One of the main uncertainties remains in fixing the opacity of such systems (Tanaka et al., 2020), where theoretical predictions could not be thorough due to the complexity of blended *d*- and *f*-shell atomic lines from

freshly synthesized nuclei. Experimental surveys have been carried out in the last decade on opacity models for stellar interior, inertial fusion, and high energy density plasmas (Bailey et al., 2009), looking at the opacity of metallic elements, measuring spectral transmission in the X-ray range, with plasma conditions however out of the range of interest for the KNe study. Within the PANDORA (Plasmas for Astrophysics Nuclear Decays Observation and Radiation for Archaeometry) project (Mascali et al., 2022), we intend to provide, in the forthcoming years, critical new nuclear and atomic physics inputs from advanced theoretical models and experiments. In particular, the in-plasma atomic physics knowledge on the opacity of several metallic nuclei from *r*-process will allow to extend the understanding on the microphysics of KNe. We have recently performed a feasibility study about typical electron cyclotron resonance (ECR) magneto-plasmas conceived in PANDORA, which confirms – in terms of thermodynamical properties of the plasma – the possibility to study early-stage timescale KNe emission expected at optical wavelengths from light *r*-process ejecta component (Pidatella et al., 2021). We present the work carried out in the framework of the PANDORA collaboration to support first-of-its-kind measurements of opacity with in-laboratory plasmas resembling these KNe-stage conditions. In this view, we have recently performed experiments at the INFN-LNS to reproduce stable early-stage ejecta thermodynamical conditions (Pidatella et al., 2022). Promising results of this campaign pushed us to present a conceptual design of a multi-diagnostic experimental setup for opacity measurements employing not only spectroscopic techniques. We also discuss about challenges and critical aspects of these envisaged experimental activities led by our experimental setup.

Methods and experimental setup

Retrieving information on the frequency-integrated plasma opacity of metallic species along a certain line-of-sight bases on the following relation between the transmission spectrum and the opacity:

$$T(\nu) = \frac{I_a(\nu)}{I_b(\nu)} = exp[-\tau(\nu)] = exp\left[-\int_0^l dx\, \rho(x)\, \kappa(\nu; n_e(x), T_e(x))\right],$$

where T(v) is the transmission spectrum (also known as transmittance), given as the ratio of the exiting, $I_a(v)$, and of the incident intensity spectrum, $I_b(v)$, which is related to the optical depth, $\tau(v) = \rho\kappa l$, of the plasma mean. The latter needs a particular treatment in the case the mean is not uniform in space along the line-of-sight of detection, since both the linear plasma density $\rho(x)$ [g cm^{-3}], and the opacity $\kappa(v;x)$[cm^2 g^{-1}], can strongly vary as a function of the depth. The opacity dependency on the depth is deeply influenced by the space-dependent electron density number, $n_e(x)$ [cm^{-3}], and electron temperature, $T_e(x)$, and the integral spectral information in Eq. (1) needs to be deconvolved. A numerical study on such impact for ECR plasmas has been performed in (Pidatella et al., 2022), stressing the necessity of devoted diagnostics to independently measure plasma temperature and density. Among main requirements for experimental measurements there are: (i) plasma sample uniform in time, (ii) accurate transmission measurements (taking care e.g., of spectral calibration, spectrometer resolution), and (iii) high-quality and stability of the light source, having broad and featureless spectrum, as well as high intensity overcoming self-emitted plasma light (Bailey et al., 2009). Many challenges are opened by combining the kinds of techniques with the ECR cavity effects. Transmission measurements occur through an active medium, i.e., self-emitting in the visible range of the electromagnetic spectrum, superimposing spectral feature arising from the radiation-matter interaction to the plasma de-excitation light emission, both from plasma gas buffer (e.g., H_2, Ar) and vaporized metal in plasma, which need to be disentangled. Moreover, spurious contributions come from light reflection at the trap chamber wall, and from the impact of the cavity on the wave propagation. Despite such difficulties, we designed a potential experimental setup to make some progress. Since the PANDORA facility is still on-construction, we propose a conceptual design for the opacity

measurements adapted on the already operative Flexible Plasma Trap (FPT) at the INFN-LNS (Gammino et al., 2017) as shown in Figure 1, to be then extended in the incoming PANDORA trap. The setup is based on the simultaneous use of an (a) optical spectrometer to carry optical emission spectroscopy (OES) analysis of the plasma emission, and (b) microwave interferometry to perform independent plasma density measurements. The OES will allow to measure transmission of a calibrated light source external to the chamber, facing on two independent lines: the first, crossing a collinear sight inside the plasma chamber, exiting into a fiber-connected light detector (i.e., a spectrometer coupled to a CCD detector working in the visible range). The second one, external to the chamber and used to guide the light directly to the detection system, unbiased by any effects due to the plasma or the chamber. Independent measurements on the two lines, with and without igniting the plasma, including or not in the plasma the metal of interest, will allow to disentangle the different contributions to T(v). OES can be also used to characterize plasma parameters (density, temperature) via the known line ratio method (Fantz, 2006; Pidatella et al., 2022), applied to the hydrogen (buffer gas) Balmer's lines ratios. The second diagnostics, based on the microwave interferometry, will allow to independently measure the plasma density along an OES-close line-of-sight, helpful in cross-checking OES data, and to better assess the deconvolution of the r.h.s. of the Eq. (1). The technique is based on the study of the phase-shift of the travelling microwave (f ~ tens of GHz) through two branches, an external one and another one crossing the plasma. The refractive index of the latter will induce such phase shift in a way proportional to the plasma density. For further references on the method, see (Mascali et al., 2016) and reference therein. To support this experimental activity, we have recently performed an OES plasma characterization for several plasma trap configurations as a function of the confining magnetic field, microwave frequency, gas pressure, and microwave power provided in the FPT. The outcome of this characterization highlighted a set of best experimental configurations suitable

for reproducing blue-KN conditions (n_e ~ 10^{11} cm^{-3}, T_e ~ eV), i.e., high-pressure, and low-power ones, as reported in the bottom-right plot of Figure 1. More details on the experimental setup and data can be found in (Pidatella et al., 2022).

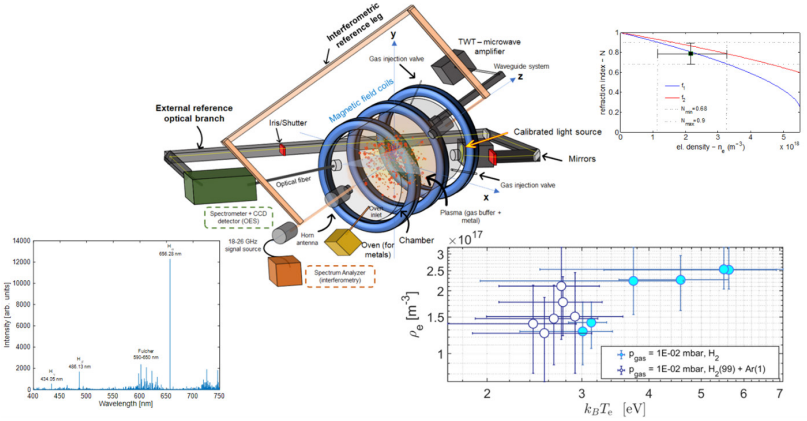

Figure 1. Conceptual design of the multi-diagnostic system on the Flexible Plasma Trap (FPT) devoted to opacity measurements. Two line-of-sights for the optical spectrometer are identified: the first, crossing a collinear sight inside the plasma chamber, between the light source and the exit optical fiber, collecting the transmitted spectrum; the second, guiding the reference light spectrum of the source through an optical guide system to the spectrometer. A typical buffer gas spectrum in the optical range (bottom left) and the range of measured density and temperature (bottom right) suitable with the KN scenario, as collected from experimental runs on FPT (p_{gas} = 1e-2 mbar, RF power 40 ÷140 W, with and w/o gas mixing of H_2 and Ar), are shown – see more in (Pidatella et al., 2022). An external reference branch for interferometric measurements of plasma density (as an independent diagnostic) is shown, along with a typical electron density measurement as a function of the refractive index and microwave phase shift – see more in (Mascali et al., 2016).

Conclusion

We reported on experimental activities on ECR laboratory plasmas in the framework of the PANDORA collaboration, aiming at performing first-of-its-kind opacity measurements relevant to assess plasma ejecta opacity

typical of binary neutron star post-merging event, and of fundamental importance in the study of the KNe signals. Based on a previous feasibility study, we presented some of the challenges and critical aspects introduced by transmittance measurements of light source through a trapped plasma, in the context of the ECR plasma trap, as possible technique for opacity measurements. A conceptual design of the experimental setup to step forward on these aspects, designed for the FPT trap at the INFN-LNS and thus for the incoming PANDORA trap, has been presented. The power of the setup is encoded in the multi-diagnostic approach which is one of the qualities featured and boasted by the PANDORA trap as well. This will allow to cross-check variable data and to perform independent and simultaneous measurements. Several independent acquisitions of spectral data must be performed to disentangle the many contributions to the transmission spectrum and thus to retrieve accurately the plasma opacity. This is made possible by the in-time stability and reproducibility of magneto-plasma conditions, which is one of the experimental requirements. The ECR plasmas produced in FPT have been tested on this side, checking for stability and for suitable plasma conditions to reproduce the astrophysical scenario. Promising results have been obtained, satisfying all the mentioned requirements. Especially the in-time reproducibility represents a big advantage with respect other explored plasma environments and laboratory facilities, where instead time-gated measurements must be performed due to strong time dependency of plasma structure. In perspective, PANDORA will host many further diagnostics lines which will help in extending the plasma parameters analysis, for instance providing local information on density and temperature, and possibly profilometric investigations, based both on microwave (Torrisi et al., 2022) and X-ray imaging techniques (Naselli et al., 2021).

Acknowledgements

The author would like to thank INFN for the support through the project PANDORA Gr3 funded by 3rd Nat. Sci. Comm., and to thank the whole PANDORA collaboration.

References

Abbott, B.P., et al. (LIGO Scientific Collaboration and Virgo Collaboration), 2017. GW170817: Observation of Gravitational Waves from a Binary Neutron Star Inspiral. Phys. Rev. Lett. 119, 161101.

Arcavi, I., et al., 2017. Optical emission from a kilonova following a gravitational-wave-detected neutron-star merger. Nature 551, 64.

Bailey, J.E., et al., 2009. Experimental investigation of opacity models for stellar interior, inertial fusion, and high energy density plasmas. Phys. Plasmas 16, 058101.

Fantz, U., 2006. Basics of plasma spectroscopy. Plasma Sources Science and Technology 15, S137.

Gammino, S., et al., 2017. The Flexible Plasma Trap (FPT) for the production of overdense plasmas. Journal of Instrumentation 12, P07027.

Kasen, D., et al., 2017. Origin of the heavy elements in binary neutron-star mergers from a gravitational-wave event. Nature 551, 80.

Korobkin, O., et al., 2012. On the astrophysical robustness of the neutron star merger r-process. Monthly Notices of the Royal Astronomical Society 426, 1940.

Li, L.X., et al., 1998. Transient Events from Neutron Star Mergers. The Astrophysical Journal 507, L59.

Mascali, D., et al., 2016. The first measurement of plasma density in an ECRIS-like device by means of a frequency-sweep microwave interferometer. Review of Scientific Instruments 87, 095109 (2016).

Mascali, D. et al., 2022. A Novel Approach to β-Decay: PANDORA, a New Experimental Setup for Future In-Plasma Measurements. Universe 2022, 8, 80.

Metzger, B.D., et al., 2010. Electromagnetic counterparts of compact object mergers powered by the radioactive decay of r-process nuclei. Monthly Notices of the Royal Astronomical Society 406, 2650.

Naselli, E., et al., 2021. Innovative analytical method for X-ray imaging and space-resolved spectroscopy of ECR plasmas. Condensed Matter 7 (1), 5.

Pidatella, A., et al., 2021. In-plasma study of opacity relevant for compact binary ejecta. Il Nuovo Cimento C 44, 4.

Pidatella, A., et al., 2022. Experimental and numerical investigation of magneto-plasma optical properties toward measurements of opacity relevant for compact binary objects. Frontiers in Astronomy and Space Sciences 9, 225.

Tanaka, M., et al., 2020. Systematic Opacity Calculations for Kilonovae. Mon. Not. Roy. Astron. Soc. 496, 1369.

Torrisi, G. et al., 2022. RF and microwave diagnostics for compact plasma traps and possible perspectives for fusion devices. JINST 17 C01050.

Watson, D., et al., 2019. Identification of strontium in the merger of two neutron stars. Nature 574, 497-500.

Extreme TeV BL Lacs: a self-consistent stochastic acceleration model

Alberto Sciaccaluga[1,2], *Fabrizio Tavecchio*[1]

Abstract

Lately, a specific kind of blazar drew the attention of the gamma-ray astronomy community: the extreme TeV BL Lacs, blazars that present an extremely energetic and hard emission at very high-energy. Explaining their features is still an open challenge, in fact the most used phenomenological models have difficulties to satisfactorily reproduce their Spectral Energy Distributions (SED). Based on a scenario we have recently proposed, we suppose that the non-thermal particles are firstly accelerated by a jet recollimation shock, which induces turbulence in the rest of the jet. Non-thermal particles are further accelerated by the turbulence, which hardens the particle spectra and accordingly the radiative emission. Given the physical properties of the plasma, as inferred by emission models, we expect a strong impact of the accelerating particles on the turbulence. Assuming isotropy and homogeneity, the interaction between non-thermal particles and turbulence and their spectra is modeled solving a system of two non-linear, coupled Fokker-Planck equations, while the radiative emission is calculated through the Synchrotron Self Compton model. The emission predicted by our model

[1] INAF – Osservatorio Astronomico di Brera, via E. Bianchi 46, I–23807, Merate, Italy Correspondence: alberto.sciaccaluga@inaf.it

[2] Università degli studi di Genova, via Balbi 5, I-16126 Genova, Italy.

is then compared with the prototype extreme TeV BL Lac object 1ES 0229+200 and the parameters obtained to reproduce its SED are in line with the expectations.

Key Words
AGN, Blazars, Shocks, Turbulence, Radiative models.

Introduction

Blazars are active galactic nuclei with a relativistic jet (produced in the supermassive black hole vicinity and propagating far outside the host galaxy) pointing toward the Earth (Blandford et al., 2019). Thanks to the relativistic beaming their emission is dominated by the jet non-thermal component, characterized by an emission ranging from radio to gamma-ray. The SED displays two broad peaks, attributed to synchrotron and inverse Compton mechanisms (but the high-energy peak is also interpreted in terms of hadronic processes). Generally, the variability of the blazar emission is extreme, both in amplitude and timescale (Sol & Zech 2022).

Among blazars, extreme highly peaked BL Lac objects (EHBLs) are a peculiar class which recently emerged because of their unique features (Biteau et al., 2020). In particular we focus on the extreme TeV BL Lacs, a subclass of the EHBLs which displays extreme properties: i) the second SED peak beyond; ii) a hard sub-TeV intrinsic spectrum; iii) in most cases, the TeV emission is stable over years. These characteristics are hardly reproducible by a phenomenological model based only on diffusive shock acceleration by a single shock. In fact the sub-TeV spectrum hardness requires the particle spectrum to have spectral index $p < 2$ (supposing $dN/d\gamma \propto \gamma^{-p}$), but with a single shock acceleration $p \geq 2$ (Biteau et al., 2020).

Leptonic models which leave the acceleration process unspecified show that the magnetization of extreme TeV BL Lacs is low, therefore the diffusive shock acceleration should work efficiently. Zech & Lemoine (2021) proposed a model based on diffusive shock acceleration by

multiple shocks. In this scenario non-thermal particles are accelerated multiple times and they can reproduce the hard spectra observed for the extreme TeV BL Lacs. However Matsumoto et al. (2021) show that if the magnetization is below a critical value, after the first shock the jet becomes unstable and turbulent due to the development of instabilities, preventing the formation of additional shocks. Based on this new evidence, we have proposed a different scenario.

Model

Here we describe an extension of the simple treatment in Tavecchio et al. 2022, introducing a self-consistent model capable of describing the interplay between the turbulence damping and the non-thermal particles acceleration (Sciaccaluga & Tavecchio, 2022).

We suppose that the non-thermal particles are first accelerated by a recollimation shock, formed in the jet when the external pressure is greater than the jet pressure. As already explained, the shock acceleration process is a deterministic process and the output spectra of the non-thermal particles is a power law, with spectral index $p \geq 2$.

The non-thermal particles injected by the recollimation shock can be further energized interacting with the turbulence, hardening the distribution and therefore the emitted spectrum. Non-thermal particles are supposed to be accelerated mostly through gyroresonant interaction with the weakly turbulent Alfvén waves. This acceleration process is stochastic and in order to study the equilibrium spectra of both the non-thermal particle spectra and the turbulence it is necessary to consider the time evolution of their phase-space densities through two momentum diffusion equations.

Assuming isotropy and homogeneity, the momentum diffusion equation can be highly simplified, obtaining the classical Fokker-Planck equation. Therefore our goal is to solve a system of two coupled non-linear Fokker-Planck equations, which describe both the interaction and the spectra of the non-thermal particles and of tur-

bulence (Kakuwa, 2016). The emission recorded by the observer is produced in the shock downstream region and comprises non-thermal particles at different stages of acceleration, from the shock to the top of the emitting region, which is modelled as a cylinder of radius R and length 10 R. We can be relatively confident that within such a distance, the magnetic field decay and the adiabatic losses effectively quench the emission. All quantities appearing in equations below are expressed in the downstream jet frame, we will move to the observer frame only for the quantities linked to the radiative emission.

The first equation describes the time evolution of $f(p)$, the momentum distribution of the non-thermal particles, from here on supposed to be relativistic electrons, since we are considering a leptonic model:

$$\frac{\partial f}{\partial t} = \frac{1}{p^2}\frac{\partial}{\partial p}\left[p^2 D_p \frac{\partial f}{\partial p} + p^2 \left(\frac{\partial p}{\partial t}\right)_{\text{rad}} f\right] + \frac{f}{t_{\text{esc}}} + I_f$$

where p is the particle momentum, D_p the momentum diffusion coefficient, $(\partial p/\partial t)_{\text{rad}}$ the cooling coefficient due to radiative emission and I_f is the particle injection rate. Starting from momentum distribution, it is possible to calculate the electron energy density, in fact $n(\gamma) = 4\pi p^2 f(p) m_e c$, where m_e is the electron mass.

The second equation we have to consider describes, in a phenomenological way, the time evolution of $W(k)$, the wavenumber energy distribution of the turbulence, i.e. the energy density of waves with wavenumber between k and $k + dk$. Defining $Z(\text{k}) = W(k)/k^2$, in order to obtain a Fokker-Planck equation in its canonical form, the equation can be written as:

$$\frac{\partial Z}{\partial t} = \frac{1}{k^2}\frac{\partial}{\partial k}\left(k^2 D_k \frac{\partial Z}{\partial k}\right) + \frac{Z}{t_{\text{dam}}} + \frac{I_W}{k^2}$$

where D_k is the wavenumber diffusion coefficient (which depends on $W(k)$ itself, making the equation non linear), t_{dam} the damping time and I_W the turbulence injection rate. Spatial effects (such as wave propagation outside the downstream region) are negligible with respect to

the damping of non-thermal electrons, while dissipation mechanisms (such as Landau or cyclotron damping) can be ignored because of the low density of jet thermal plasma.

The radiative emission is calculated through the Synchrotron Self Compton model, see Chiaberge & Ghisellini (1999) for the synchrotron emission and Blumenthal & Gould (1970) for the inverse Compton emission, while for the beaming we use the standard formula, see discussion in Zech & Lemoine (2021).

Results

Our model depends on five free parameters: the downstream region radius R, the Alfvén velocity v_a, the mean magnetic field B, the injected powers of the electrons and the turbulence in the jet frame, respectively P'_n and P'_W.

We apply our model to the prototypical extreme TeV BL Lac object, i.e. 1ES 0229+200 (z = 0.1396).

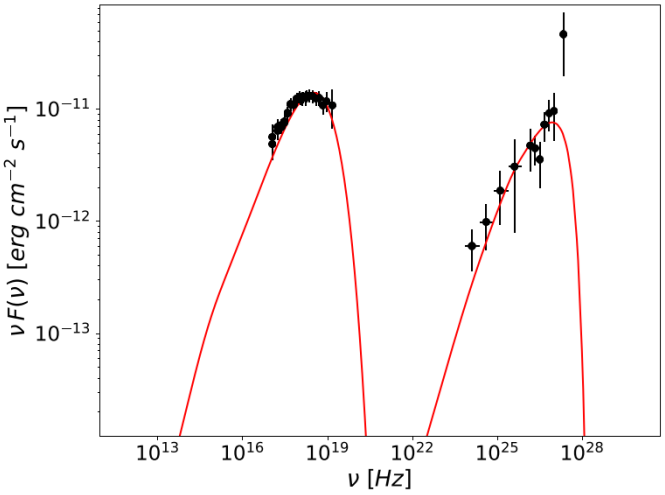

Figure 1: SED of 1ES 0229+200 (points with error bars, from Costamante et al. 2018) reproduced with the model presented in the paper (red solid line).

Figure 1 shows a model realization ($R = 1.2 \times 10^{16}$ cm, $v_a = 2 \times 10^9$ cm/s, $B = 15.9$ mG, $P'_n = 7 \times 10^{39}$ erg/s, $P'_W = 7 \times 10^{39}$ erg/s). In this first illustration of the model, the relativistic Doppler factor is fixed for simplicity to $\delta = 25$. In applying the model to a full sample of sources, the relativistic Doppler factor could be included in the set of the free parameters. The realization shown in Figure 1 is in good agreement with the data: in fact the X-ray peak is well reproduced and the model realization presents a hard sub TeV spectrum with a gamma peak beyond 1 TeV.

The free parameters are consistent with what we expect from the theory. Since the emission is due to the post-reconfinement flow, R is much smaller than the ordinary jet radius (Bodo & Tavecchio, 2018), whereas the Alfvén velocity is large with respect to the usual values in order to make the stochastic acceleration energy gain relevant for the non-thermal particles. Moreover the magnetic field is in the order of the values obtained by the phenomenological models that leave the acceleration process unspecified (Biteau et al., 2020). Finally the injected power of the non-thermal particle in the jet frame is in agreement with the theory predictions (Ghisellini & Tavecchio, 2010).

Conclusions

We have presented a self-consistent model for extreme TeV BL Lac objects, improving the simple version of Tavecchio et al. (2022). In particular, the inclusion of damping for the turbulence results in an electron distribution with an excess of particles below the peak, around $\gamma \simeq 10^4$ - 10^5, which produces a softer SSC component in the VHE band, in better agreement with the data with respect to the simple model without wave damping.

Our model is able to reproduce the SED of the prototypical extreme TeV BL Lac object 1ES 0229+200, but there are several caveats. First of all it will be necessary to compare our model with the data of other extreme TeV BL Lacs in order to check if this hybrid

emission scenario can be generalized to the entire population. Since the classification of this type of sources is still unclear, a different emission scenario could trigger a new way to categorize these objects. Moreover the parameters obtained by the comparison between SEDs and the model have to be checked with the results of MHD simulation. The papers already published shows that the low magnetization scenario favors the development of turbulence after the recollimation shock instead of the formation of multiple shocks. A better characterization of the emission region and turbulence based on dedicated MHD simulations will be presented in the near future (Costa et al., in prep).

Considering the model in this paper, there are some possible improvements. Firstly the Inverse Compton (i.e. SSC) cooling term could be added in the diffusion equation of non-thermal electrons, which would make the equation [eq:fp_part] non-linear too. Moreover the computational scheme used to solve the system in this paper could be replaced with more complex and accurate algorithms.

In the following years the number of extreme TeV BL Lacs will probably increase and their SED measurements will improve. In fact many data are going to be collected, since these sources are already studied by several telescopes and they will also be objects of interest for future gamma-ray facilities, such as CTA, because of their extreme high energy emission. Finally, another observational feature useful to test our model will be the polarization properties of the extreme TeV BL Lacs. Polarimetric measures in the optical band are extremely difficult for this type of sources because of the weak emission of the jet in this band, dominated by the emission of the host galaxy. Instead in the X-ray band the emission is mainly due to the synchrotron cooling of the jet particles emitting in a highly turbulent field, therefore we expect a low degree of polarization. This prediction could be proved by the IXPE mission, the first satellite able to measure the polarization in the X-ray band, launched at the end of 2021.

References

Biteau, J., Prandini, E., Costamante, L., Lemoine, M., Padovani, P., Pueschel, E., Resconi, E., Tavecchio, F., Taylor, A. and Zech, A., 2020. Progress in unveiling extreme particle acceleration in persistent astrophysical jets. Nature Astronomy 4: 124-131.

Blandford, R., Meier, D. and Readhead, A., 2019. Relativistic Jets from Active Galactic Nuclei. Annual Review of Astronomy and Astrophysics 57: 467-509.

Blumenthal, G.R. and Gould, R.J., 1970. Bremsstrahlung, Synchrotron Radiation, and Compton Scattering of High-Energy Electrons Traversing Dilute Gases. Reviews of Modern Physics 42: 237-271.

Bodo, G. and Tavecchio, F., 2018. Recollimation shocks and radiative losses in extragalactic relativistic jets. Astronomy and Astrophysics 609: A122.

Chiaberge, M. and Ghisellini, G., 1999. Rapid variability in the synchrotron self-Compton model for blazars. MNRAS 306: 551-560.

Ghisellini, G. and Tavecchio, F., 2010. Compton rockets and the minimum power of relativistic jets. MNRAS 409: L79-L83.

Kakuwa, J., 2016. Stochastic Gyroresonant Acceleration for Hard Electron Spectra of Blazars: Effect of Damping of Cascading Turbulence. Astrophysical Journal 816: 24.

Matsumoto, Jin, Komissarov, S.S. and Gourgouliatos, K.N., 2021. Magnetic inhibition of the recollimation instability in relativistic jets. MNRAS 503: 4918-4929.

Sciaccaluga, A. and Tavecchio, F., 2022. Extreme TeV BL Lacs: a self-consistent stochastic acceleration model. MNRAS 517: 2502-2507.

Sol, H. and Zech, A., 2022. Blazars at Very High Energies: Emission Modelling. Galaxies 10: 6.

Tavecchio, F., Costa, A. and Sciaccaluga, A., 2022. Extreme blazars: the result of unstable recollimated jets?. MNRAS 517: L16-L20.

Zech, A. and Lemoine, M., 2021. Electron-proton co-acceleration on relativistic shocks in extreme-TeV blazars. Astronomy and Astrophysics 654: A96.

Stability of hypermassive neutron stars against a prompt collapse

Paweł Szewczyk[1], Dorota Gondek-Rosińska[1], Pablo Cerdá-Durán[2]

Abstract

Differentially rotating neutron stars, which can be produced in core-collapse supernova explosions or binary neutron star mergers, may be significantly more massive than rigidly rotating neutron stars. Even for a modest degree of differential rotation, there exist equilibrium solutions with masses up to 4 times larger than the maximum mass of non-rotating neutron star (TOV limit). The immediate fate of the hypermassive remnant may have an impact on the gravitational wave and electromagnetic emission from a core-collapse supernova or binary neutron star merger. We investigate the dynamical stability against quasi-radial perturbations of differentially rotating neutron stars. We perform a series of hydrodynamical simulations of hypermassive neutron stars. We check whether the object undergoes a prompt collapse or stays stable on dynamical timescales. We present the preliminary results of our stability studies for masses up to 2 times larger than TOV limit. The threshold to collapse that we find is close to the limit estimated by the turning-point criterion.

---

[1] Astronomical Observatory, University of Warsaw, a. Ujazdowskie 4, 00-478 Warsaw, Poland.

[2] Departamento de Astronomía y Astrofísica, Universitat de València, E-46100 Burjassot, València, Spain.

Introduction

Simultaneous detection of the binary neutron stars (BNS) merger GW170817 (Abbott et al., 2017) in both gravitational waves (GW) and electromagnetic domain marked the beginning of a new era in astronomy. A broad range of astrophysical scenarios may lead to detectable GW emission in the predictable future. Some of them involve the formation of a compact object – either a black hole or a neutron star. One of those scenarios is a merger of two neutron stars, already detected in 2017. Another one is a core-collapse supernova, which is yet to be detected by GW observatories. A significantly differential rotation is expected in the compact remnant in both cases (Komatsu, Eriguchi, & Hachisu, 1989; Kastaun & Galeazzi, 2015).

For non-rotating neutron stars, a maximum gravitational mass can be easily found for a given equation of state (EOS) of dense matter. We call this value TOV limit (M_{TOV}). Rigid rotation allows for masses larger by 15-20% depending on EOS. A detailed study of the solution space of differentially rotating neutron stars has shown that significantly larger masses can be supported with differential rotation than with rigid rotation. Such objects that exist only because of their differential rotation are often called hypermassive neutron stars. It was first shown by Baumgarte, Stuart L. Shapiro, and Shibata (2000) that dynamically stable hypermassive neutron stars may exist. Four types of solutions of differentially rotating neutron stars were discovered by Ansorg, Gondek-Rosińska, and Villain (2008). With all solution types included, independently of the equation of state, a set of equilibrium configurations as massive as 3-4M_{TOV} was found (Gondek-Rosińska et al., 2017; Studzińska et al., 2016; Espino and Paschalidis, 2019; Szkudlarek et al., 2019). Similar features were discovered for a novel rotation profile, resembling the BNS merger remnant, by Iosif and N. Stergioulas (2021). Most importantly, the maximum mass occurs not for the extreme degrees of differential rotation, but for modest ones.

The mass of a BNS merger remnant is of course limited by the total mass of the system, which cannot be more than twice as massive as the most massive secularly stable neutron star. The core-collapse supernovae do not have such limitations and even more mass can be accumulated in the remnant.

The dynamical stability of hypermassive neutron stars was recently studied by Pedro L. Espino et al. (2019). Some of the most massive configurations in the solution space were found to be dynamically unstable and undergo a prompt collapse to a black hole. Meanwhile, some stable configurations of masses larger than $1.4M_{TOV}$ were found by Weih, Most, and Rezzolla (2018). A more thorough study of the stability properties of hypermassive neutron stars is needed to find the actual threshold to a prompt collapse and the mass limit for dynamically stable configurations.

In this paper, we study the dynamical stability of hypermassive neutron stars by means of numerical simulations of their evolution in time. We choose a rotation profile consistent with the properties of core- collapse remnants and a polytropic equation of state with $\Gamma = 2$.

Methods

Equilibrium configurations

To model equilibrium configurations of neutron stars, we consider a perfect barotropic self-gravitating fluid. We use the well-established J-const rotation law (Komatsu, Eriguchi, and Hachisu, 1989), which was shown to be consistent with the rotation profiles in compact core-collapse supernova remnants (Villain et al., 2004). The steepness of our rotation profiles is characterized by one dimensionless parameter $\tilde{A}$, which we call a degree of differential rotation. For the value $\tilde{A} = 0$ the rotation becomes uniform (rigid). Larger values mean a larger difference in angular velocity between the inner and the outer layers of the configuration.

To describe the properties of matter in the neutron stars we assume a polytropic equation of state with $\Gamma = 2$. If not stated otherwise, we use natural units where $c = 1$ and $G = 1$. For simplicity, we set the polytropic constant to $K = 1$, but the resulting parameters of a configuration can be easily scaled with different K (see e.g. Cook, S. L. Shapiro, and Teukolsky, 1994). To provide masses in units of the solar mass, we rescale our results with $K = 100$.

We construct a series of equilibrium configurations using the highly accurate and stable FlatStar code (Ansorg, Kleinwa ̈chter, & Meinel, 2003; Ansorg, Gondek-Rosińska, and Villain, 2008). It has proven to be a numerically challenging task and many well-established tools failed to construct highly flattened configurations in the past (e.g. Baumgarte, Stuart L. Shapiro, and Shibata (2000), Lyford, Baumgarte, and Stuart L. Shapiro, 2003). The FlatStar code was previously successfully used to construct equilibrium solutions in the whole parameter space for differentially rotating neutron stars (Gondek-Rosińska et al., 2017; Studzińska et al., 2016) and strange quark stars (Szkudlarek et al., 2019).

A classification into four distinct types of solutions was introduced by Ansorg, Gondek-Rosińska, and Villain (2008). In this paper, we considered solutions of types A and C only.

For the selected values of the degree of differential rotation $\hat{A}$, we construct sequences of constant rest mass M_0, which can be parametrized by the value of maximal density ρ_{max} or maximal relativistic enthalpy H_{max}. We inspect the values of gravitational mass M along those sequences and find the point of minimal value (a turning point). Turning points can be used in the rigid rotation case to estimate the dynamical stability (they mark the onset of quasi-radial instabilities). This criterion was already used for the differential rotation case by e.g. Bozzola and A. Stergioulas N. B. (2018) and Weih, Most, and Rezzolla, 2018. For differential rotation, we use it as a first estimation of the stability limit and select configurations close to it for further studies.

Hydrodynamical evolution

To test the stability of selected configurations we perform a series of hydrodynamical simulations. We use the well-established CoCoNuT code (Cerdá-Durán et al., 2008) which allows us to perform hydrodynamical simulations with dynamical timespace evolution.

For each considered value of $\hat{A}$ we select a sample of equilibrium configurations near the estimated threshold of stability. For each configuration we perform a simulation of its time evolution. In theory, a small perturbation resulting from numerical approximations is enough to initiate a prompt collapse in an unstable configuration. However, the configurations that are close to the stability limit tend to migrate to the stable branch, shifting the apparent stability limit. This issue was previously discussed by Weih, Most, and Rezzolla (2018).

To prevent this migration, to each configuration we introduce an additional radial velocity perturbation.

We gauge the amplitude of this perturbation to the value, for which the mean value of ρ_{max} matches its initial value. This method has proven to reproduce results known from Takami, Rezzolla, and Yoshida (2011) for rigid rotation and from Weih, Most, and Rezzolla (2018) for differential rotation.

By inspecting the behavior of ρ_{max}, the metric components, and other parameters we recognize the immediate start of a collapse in some configurations, which we mark as unstable. For configurations marked as stable, we observe an oscillation of those parameters.

Results

We have inspected the stability properties of more than a hundred differentially rotating configurations and found a threshold to immediate collapse for a wide range of parameters.

For $\hat{A} = 0.2$ and $\hat{A} = 0.77$ we have compared our results with Weih, Most, and Rezzolla (2018) and found them to be in agreement. We have also compared the stability threshold found by our methods for

$\tilde{A} = 0$ (rigid rotation) with the results of Takami, Rezzolla, and Yoshida (2011), which was consistent with each other.

M_0	H^{TP}_{max}	H^{*}_{max}	$1 - H^{TP}_{max}/H^{*}_{max}$	M^{*}/M_{TOV}	$M^{*}(K = 100)$
0.23	0.407	0.385	5.41%	1.277	$2.090 M_{\odot}$
0.26	0.375	0.345	8.00%	1.439	$2.356 M_{\odot}$
0.30	0.331	0.315	4.83%	1.652	$2.705 M_{\odot}$
0.33	0.304	0.305	-0.32%	1.806	$2.957 M_{\odot}$
0.36	0.285	0.295	-3.51%	1.968	$3.222 M_{\odot}$

Table 1: Parameters of the stability threshold on each studied sequence of constant M_0 for $\tilde{A} = 0.77$. M^{*} is the gravitational mass and H^{*}_{max} is the relativistic enthalpy for the marginally stable configuration on each sequence. H^{TP}_{max} marks the turning-point on given sequence. Values of mass are also presented in units of $M_{\odot}$ for the polytropic constant $K = 100$.

We have extended the parameter space studied by Weih, Most, and Rezzolla (2018) for $\tilde{A} = 0.77$ to the region of quasi-toroidal configurations – i.e. those configurations for which the maximal density occurs not in the center, but off the rotation axis.

In the case of $\tilde{A} = 0.77$ models, we found that going into the quasi-toroidal regime does not immediately impact the stability of differentially rotating neutron stars. We found a large region of dynamically stable solutions with large masses and a clear boundary between stable and unstable solutions. We stopped our analysis at the gravitational mass $M{=}2M_{TOV}$ due to numerical limitations.

For this study, we have chosen several sequences of configurations with $\tilde{A} = 0.77$, each characterized by a constant rest mass. We selected 32 configurations distributed along those sequences and close to the stability limit and performed a hydrodynamical simulation for each of them. On each sequence, we have estimated the boundary between the stable and unstable solutions. Table 1 shows the parameters of those marginally stable configurations for each sequence and the location of the turning point (point of minimal mass) along that sequence. The value of gravitational mass is presented in the relation to the maximum mass of non-rotating configuration M_{TOV}.

We found that the turning-point line is a close estimation of the dynamical stability even for large masses – the stability limit lies within 8% relative error in H_{max}. For the largest masses we studied, the turning point occurs before the threshold of stability that we found (for lower H_{max}).

Summary and discussion

For a wide range of parameters, we found a limit of dynamical stability against quasi-radial oscillations. A series of stable solutions was found in the previously poorly explored quasi-toroidal regime. We have shown that configurations as massive as $2M_{TOV}$ can be stabilized, giving interesting prospects for studying massive remnants of core-collapse supernovae.

Our results, however, do not take into account any non-axisymmetrical effects. A series of 3D simulations are needed to establish more realistic stability limit.

References

Abbott, B.P., et al. 2017. Phys. Rev. Lett. 119 (16 2017), p. 161101. DOI:10.1103/PhysRevLett.119. 161101. URL: https://link.aps.org/doi/10.1103/PhysRevLett.119.161101.

Ansorg, M., Gondek-Rosińska, D. and Villain, L. 2008. Monthly Notices of the Royal Astronomical Society 396 (2008). DOI: 10.1111/j.1365-2966.2009.14904.x.

Ansorg, M., Kleinwächter, A. and Meinel, R. 2003. A&A 405 (2003), pp. 711-721. DOI: 10.1051/ 0004-6361:20030618. arXiv: astroph/0301173 [astro-ph].

Baumgarte, T.W., Shapiro, S.L. and Shibata M. 2000. ApJ 528.1 (2000), pp. L29-L32. DOI: 10.1086/312425. arXiv: astroph/9910565 [astro-ph].

Bozzola G., Stergioulas A. and Bauswein, N. 2018. MNRAS 474.3 (2018), pp. 3557-3564. DOI: 10.1093/mnras/stx3002. arXiv: 1709.02787 [grqc].

Cerda-Duran P. et al. 2008. A&A 492.3 (2008), pp. 937-953. DOI:10.1051/0004-6361:200810086. arXiv: 0804.4572 [astro-ph].

Cook, G.B., Shapiro, S.L. and Teukolsky S.A. 1994. ApJ 424 (1994), pp. 823-845. DOI: 10.1086/ 173934.

Espino, P.L. and Paschalidis, V. 2019. Phys. Rev. D 99.8, 083017 (2019), p. 083017. DOI: 10.1103/ PhysRevD.99.083017. arXiv: 1901.05479 [astro-ph.HE].

Espino, P.L. et al. 2019. Phys. Rev. D 100.4, 043014 (2019), p. 043014. DOI: 10.1103/PhysRevD. 100.043014. arXiv: 1906.08786 [astro-ph.HE].

Gondek-Rosińska, D. et al. 2017. ApJ 837, 58 (2017), p. 58. DOI: 10.3847/1538-4357/aa56c1. arXiv: 1609.02336 [astro-ph.HE].

Iosif, P. and Stergioulas, N. 2021. MNRAS 503.1 (2021), pp. 850-866. DOI: 10.1093/ mnras/stab392. arXiv: 2011.10612 [gr-qc].

Kastaun, W. and Galeazzi, F. 2015. Phys. Rev. D 91 (6 2015), p. 064027. DOI: 10.1103/ PhysRevD.91.064027. URL: https://link.aps.org/doi/10.1103/PhysRevD.91.064027.

Komatsu, H., Eriguchi, Y. and Hachisu, I. 1989. MNRAS 237 (1989), pp. 355-379. DOI: 10.1093/ mnras/237.2.355.

Lyford, N.D., Baumgarte, T.W. and Shapiro S.L. 2003. ApJ 583.1 (2003), pp. 410-415. DOI: 10.1086/345350. arXiv: grqc/0210012 [gr-qc].

Studzińska, A.M. et al. 2016. MNRAS 463 (2016), pp. 2667–2679. DOI:10.1093/mnras/stw2152.

Szkudlarek, M. et al. 2019. ApJ 879, 44 (2019), p. 44. DOI: 10.3847/1538-4357/ab1752. arXiv: 1904.03759 [astro-ph.HE].

Takami, K. Rezzolla, L. and Yoshida, S. 2011. Monthly Notices of the Royal Astronomical Society: Letters 416.1 (2011), pp. L1–L5. ISSN: 1745-3925. DOI: 10.1111/j.1745-3933.2011.01085.x. eprint: http://oup.prod.sis.lan/mnrasl/article-pdf/416/1/L1/6140636/416-1- L1.pdf. URL:https://doi.org/10.1111/j.1745-3933.2011.01085.x.

Villain, L. et al. 2004. A&A 418 (2004), pp. 283-294. DOI: 10.1051/0004-6361:20035619. arXiv: astro-ph/0310875 [astro-ph].

Weih, L.R. Most, E.R. and Rezzolla, L. 2018. MNRAS 473.1 (2018), pp.128 L126–L130. DOI: 10.1093/ mnrasl/slx178. arXiv: 1709.06058 [gr-qc].

Collana ***Scienze Fisiche***

1. Probing the universe with multi-messenger astrophysics, Silvano Tosi, 2023 (ISBN: 978-88-3618-218-3)

Silvano Tosi is a professor at the University of Genoa, with scientific association to INFN and INAF. He carries out research in high-energy physics and astrophysics: he was a member of the BABAR experiment, until 2008 and of CMS, at the LHC accelerator of CERN, since 2008; since 2019 he is a member of Euclid, an ESA mission. He is also involved in optical astronomy. He is a professor of General Physics and Fundamentals of Astrophysics and Cosmology. He also carries out dissemination activities.

The conference, jointly organized by the Department of Physics of the University of Genova and by INFN-Sezione di Genova, aims at gathering an overview of the status and future prospects of astrophysics and cosmology with a multimessenger approach. The sessions deal with astrophysics with electromagnetic waves, astrophysics with gravitational waves, astroparticle physics and neutrino astrophysics, nuclear astrophysics, cosmology. The sessions and the talks are organised according to astrophysical sources and phenomena: compact objects, neutron star mergers, supernovae, active galactic nuclei, CMB, etc highlighting the current status of the knowledge and the benefit of a multimessenger approach.

ISBN: 978-88-3618-218-3

9 788836 182183

In copertina:
Galassia M64

Università di Genova

RICERCA